Important Notice

UNIVERSITY OF CALGARY

Integration of Seismic Methods with Reservoir Simulation, Pikes Peak

Heavy Oil Field, Saskatchewan

by

Ying Zou

A THESIS

SUBMITTED TO THE FACULTY OF GRADUATE STUDIES

IN PARTIAL FULFILMENT OF THE REQUIREMENTS FOR THE

DEGREE OF DOCTOR OF PHILOSOPHY

DEPARTMENT OF GEOLOGY AND GEOPHYSICS

CALGARY, ALBERTA

APRIL 2005

UNIVERSITY OF CALGARY

FACULTY OF GRADUATE STUDIES

The undersigned certify that they have read, and recommend to the Faculty of Graduate Studies for acceptance, a thesis entitled "Integration of Seismic Methods with Reservoir Simulation, Pikes Peak Heavy Oil Field, Saskatchewan" submitted by Ying Zou in partial fulfilment of the requirements of the degree of doctor of philosophy.

_____
Supervisor, Dr. L. R. Bentley,

Department of Geology and

Geophysics,

University of Calgary

_____
Co-supervisor, Dr. L. R. Lines

Department of Geology and

Geophysics,

University of Calgary

_____
Dr. D. Coombe,

Computational Modelling Group

_____
Dr. J. Bancroft,

Department of Geology and

Geophysics,

_____
Dr. I. Gates,

Department of Chemical &

Petroleum Engineering,

University of Calgary

University of Calgary

_____
Dr. D. R. Schmitt,

Department of Physics,

University of Alberta

_____
Date

Abstract

The Pikes Peak heavy oil field has been operated by Husky Energy Ltd since 1981.

Steam injection has been successfully employed to increase production. Efforts in

geophysics and reservoir engineering have been made to improve interpretations in the

mapping of reservoir conditions. This dissertation developed tools and a working flow for

integrating the analysis of time-lapse seismic surveys with reservoir simulation, and

applied them to the Pikes Peak field.

Two time-lapse 2D seismic lines acquired in February 1991 and March 2000 in the

eastern part of the field were carefully processed to produce wavelet and structure

matched final sections. Reservoir simulation based on the field reservoir production

history was carried out. It provided independent complementary information for the time-

lapse seismic analysis. A rock physics procedure based on Gassmann's equation and

Batzle and Wang's empirical relationship successfully linked the reservoir engineering to

the seismic method. Based on the resultant seismic models, synthetic seismic sections

were generated as the analogy of field seismic sections.

The integrated interpretation for the Pikes Peak reservoir drew the following conclusions:

The areas with a gas saturation difference, between two compared time steps, have

seismic differences. Thicker gas zones correspond with large reflectivity changes on the

top of the reservoir and larger traveltime delays in the seismic section. The thin gas zones

only induce large reflectivity changes on the top of the reservoir, and do not have large

time delays below the reservoir zone. High temperature regions also correlate with areas

having large seismic energy differences. High temperature with thick gas (steam and

methane) zones may be evidence for steam existence. The seismic differences at locations far from the production zone are due to the lower pressure that causes solution gas to evolve from the oil. Pressure changes propagate much faster (~20 m in one month) than temperature changes (~8 m in a year) based on the reservoir simulation results. The pressure dependence of the seismic data is due to its influences on gas saturation. The bypassed oil area and steam fronts (high temperature front) can be estimated from the temperature and oil saturation distributions from the reservoir simulation. AVO results show a steam and gas zone pattern similar to the one produced by reservoir simulation.

Acknowledgements

Dedication

To my curiosity about this world.

Table of Contents

List of Tables

List of Figures and Illustrations

Chapter One: Introduction

1.1   Motivation and objective

It is well known that newly discovered oil fields are becoming smaller and smaller, and

are being discovered less frequently. As the discovery of large reservoirs decreases,

optimal reservoir management becomes more and more important (Jack, 2003). An

important tool that reservoir engineers use to manage reservoirs is reservoir simulation.

Reservoir simulation is numerical modeling of the production of a reservoir. It is based

on a model made from well logs, core information, geological structure maps, and rock

property data such as permeability and porosity. The field data of well pressure,

production rates, and other information are used as guidelines to specify production or

injection constraints for modeling. Then the modeled dynamic production rates, fluid

saturation, reservoir pressure and temperature distributions can be obtained by reservoir

simulation. These results are then compared with the field records and the procedure is

repeated, after the model is modified, until the results are consistent with field

observations. This is called history matching in reservoir engineering and it is a

procedure to obtain a realistic reservoir model.

The changes in fluid saturations, reservoir pressure, and temperature will result in

changes in geophysical properties (such as rock and fluid compressibility, shear modulus,

and bulk density). The seismic response is a function of rock and fluid compressibility,

shear modulus, and bulk density. The seismic images are results of the change of acoustic

impedance which is seismic velocity multiplied by rock bulk density. It is sensitive to

spatial contrasts in two distinct types of reservoir properties. Although it is still difficult

to distinguish individual reservoir properties from the seismic image alone, the seismic

data can detect a wide range underground structures and the change of the reservoir with time. Time-lapse seismology involves repeating the seismic surveys to construct and compare seismic images to monitor time-varying dynamic fluid-flow properties in the subsurface during reservoir production. Usually a seismic 3D survey has a CMP (Common Middle Point) grid interval of 10 m to 40 m and covers thousands of square kilometres.

Compared to engineering data, seismic data have high lateral spatial resolution because the coverage is much finer than well spacing. However, seismic data has low vertical resolution compared to well logs. Therefore time-lapse seismic images can assist in constraining the dynamic reservoir model between wells.

There is a recognized need to combine the skills of geo-scientists and engineers to build quantitative reservoir models that incorporate all available reservoir data. These integrated models are critical for forecasting, monitoring, and optimizing reservoir performance because they will enable more accurate flow simulation studies, identification of flow paths and barriers, mapping of bypassed oil, and monitoring of pressure and saturation fronts (Biondi et al, 1998).

Although we face the decline of large conventional oil reservoir discoveries, it is known that Alberta has large amounts of heavy oil. According to an article in the "New York Times" August 14, 2003 issue (Talwani, 2003), "the country's (Canada) total potential reserves can be estimated at 174 billion to 271 billion barrels" which is almost half of the remaining oil in the Middle East reserves. The heavy oil reserves could be the energy resource of the future. However, the production problem that we have to deal with is the high viscosity of the heavy oil. A typical viscosity is around 25,000 mPa.s at 18°C for the

Pikes Peak Field (Sheppard et al, 1998) and 100,000 mPa.s at 30°C for the Cold Lake

Field (Isaac, 1996). Enhanced oil recovery operations such as Cyclic Steam Stimulation

(CSS) and Steam Drive that involve injection of high temperature steam into the reservoir

are employed in heavy oil production in most cases to reduce the viscosity (den Boer and

Matthews, 1988, Eastwood et al, 1994, Sheppard et al, 1998). Both CSS and Steam Drive

techniques are expensive and environmentally costly and therefore, it is important to

locate the injection wells and producing wells wisely.

Core tests on the samples from Pikes Peak heavy oil field indicate that the compressional

velocity decreases by 21% and the shear velocity decreases by 15% when temperature

increases from 22°C to 160°C (Core Laboratories, 2000). This significant velocity

decrease can produce a considerable acoustic impedance change. Therefore, seismic

methods can be useful in locating steam fronts for optimum development of heavy oil

fields. It is important to set up a procedure to convert reservoir simulation results to the

basic seismic parameters, velocities and densities, using rock physics equations and

thereby, to generate synthetic seismic sections that correspond to heavy oil thermal

recovery processes. After this, the synthetic seismiogram based on reservoir engineering

data can be compared with the seismic survey. In this way, geophysical methods can be

integrated with reservoir engineering methods. The research plan for this thesis was

initiated based on the above ideas.

The objective of this dissertation is to develop tools and a working flow for integrating

the analysis of time-lapse seismic surveys with engineering reservoir simulation. In order

to accomplish this, the following tasks will be carried out:

- To implement optimum seismic processing on a time-lapse data set.

- To conduct reservoir simulation.

- To develop a procedure to convert the 3D output of reservoir simulation to seismic velocity and density volumes.

- To construct a complex earth model that is the combination of well logs and the velocities and densities that are converted from the reservoir simulation in order to generate synthetic seismic sections that are analogous to the seismic survey sections.

- To generate synthetic time-lapse seismic sections based on the models from the above process.

- Finally, to do an integrated analysis based on the processed seismic data, the modeled synthetic seismic data, and the reservoir engineering information from both production activity and reservoir simulation.

1.2   Reservoir monitoring study review

1.2.1   Reservoir seismic monitoring study review

The earliest published works using seismic reflection data to monitor the progress of an enhanced oil recovery process (EOR) were published in 1987. Greaves and Fulp (1987) observed bright spots and dim spots on mid-burn and post-burn 3D seismic volumes for the in-situ combustion monitoring study on the Holt Field in north-central Texas. After some laboratory test results showed that seismic velocities in sands and sandstones with heavy hydrocarbon decrease markedly with increasing temperature (Tosoya et al, 1987, Wang and Nur, 1986), several time-lapse survey analysis studies combined with synthetic seismic modeling based on these laboratory results were published. Den Boer and Matthews (1988) implemented computer modeling and saw the two predicted effects of

amplitude brightening and pushdown time delay and they also observed the same phenomenon on a time-lapse seismic survey data set over a thermal recovery heavy oil field. Eastwood et al (1994) observed high frequency attenuation and time delays in the seismic window below the steamed reservoir. They calculated velocities from their reservoir simulation results but they did not do forward modeling on the model. Lumley (1995) paid attention to time-lapse survey acquisition and processing for a feasibility study. In his thesis work, he also tried synthetic seismic modeling. Najjar et al (2003) recently built a complex seismic model on the Gullfaks reservoir in the North Sea. They also tried to map oil saturation by co-kriging the measured saturation and seismic amplitude map. The work from Jenkins et al (1997) on the Duri field of Indonesia is the most complete integration work between geophysics and reservoir engineering so far. They converted reservoir simulation output to an acoustic velocity model and calculated CMP gathers for seismic modeling (detailed procedure is not published). Schmitt (1999) used a "Shift-Stack" procedure to produce large seismic amplitude anomalies over a steam assisted gravity drainage (SAGD) field, and concluded that bright spots were correlated with heated zones. Duri field was under steam drive (steam injected from injection well and oil produced from production wells) for 31 months and in their study there is only one injection well, the temperature effect is easy to observe with the time delay up to 12 ms. CSS is more complicated than steam drive since the well is in high pressure and temperature during the steaming process and in low pressure and temperature during the producing process. The pressure and temperature from adjacent wells may be in communication (Miller and Given, 1989, Miller et al, 1987). The distributions of pressure and temperature are the interaction of steam injecting and oil

producing from several wells. Eastwood's work is the only one that dealt with the CSS process but he did not carry his reservoir model to the synthetic seismic stage, at least in the published literature.

1.2.2   Reservoir simulation for thermal recovery monitoring

The steam injection process is a common method of enhanced oil recovery (EOR) in heavy oil reservoirs. Several heavy oil fields have applied steam injection successfully and have received significant improvement in oil production. For example, the Coalinga heavy oil field in the San Joaquin Valley of California had a dramatic increase in production from 9000 b/d (barrel per day) before 1961 to 34000 b/d in 1979 (Clark et al, 2001) when steam injection was introduced. Continuous steam flooding in the Duri field, Indonesia, has been estimated to improve the recovery from 8% to 60% (Jenkins et al, 1997). However, steam flow directions, rates and sweep efficiency can be unpredictable in the presence of reservoir heterogeneity. This uncertainty can lead to expensive changes in injection well placement, perforation intervals, and surface steam facility planning. Reservoir thermal simulation based on a heterogeneous earth model and combined with production history matching is necessary to depict the trend of the heat zone (or steam zone) spreading. Thermal simulation is more complex than that for an isothermal case. The theory of thermal simulation will be briefly introduced in Chapter 4. Since the reservoir model is not unique for a production history and there are no constraints between the wells, time-lapse seismic image can provide additional information to estimate reservoir parameters between the wells. The Duri field (Jenkins et al, 1997) and the Cold Lake field (Eastwood et al, 1994) are successful cases in which in a thermal

recovery heavy oil field reservoir simulation results have matched with time-lapse seismic images.

1.3   Pikes Peak heavy oil field

1.3.1   Geological setting and production activities

The Pikes Peak field was chosen because it has significant amount of information required for the proposed study. The data have been contributed to the University of Calgary by Husky Energy Ltd. The Pikes Peak heavy oil field is located 40 km east of Lloydminster (Figure 1.1), Saskatchewan. Husky Energy Ltd has operated this field since 1981. The Pikes Peak steam project produces heavy oil from the Waseca Formation of the Lower Cretaceous Mannville Group which is at an average depth of 500 m (Van Hulten, 1984, Wong et al, 2001). The reservoir is located on an east-west structural high within an incised valley fill channel complex that trends north-south (Figure 1.2). It consists of a generally fining upward sequence with clean homogeneous unconsolidated quartzose sand at the base and sand-shale interbeds on top. The quality of the upper interbed unit decreases upward as a result of decreasing grain size and increasing clay content. The higher-quality interbeds (lower interbeds zone) often are in communication with the homogeneous sand unit and contribute to oil production (Miller et al, 1987). Locally there are calcite-cemented tight streaks in the interval. Oil saturation is around 80%. Porosity is around 34% and permeability is around 5000 md. The structurally high central portion has the best and thicker homogenous sand and has no bottom water. Most of the rest area is underlain by bottom water; the thickness is in the range of 0.3-13.3 m (Wong et al, 2001). From Wong et al's analysis, the average steam oil ratios (SOR) for the bottom water wells are higher than their non-bottom water counterparts. The

structural relief of the Mannville Group in the study area is complicated by dissolution of Middle Devonian Prairie Evaporite salt beds (Van Hulten, 1984). Figure 1.3 is a stratigraphic chart from Watson and Lines (2003). The combination of the salt dissolution and differential compaction of the sand and shale in the Waseca interval are believed to have created the structural trap for the heavy-oil (Watson and Lines 2003). The Waseca interval has an average thickness of 15 m and a maximum thickness of 30 m. Oil gravity is 12 °API.
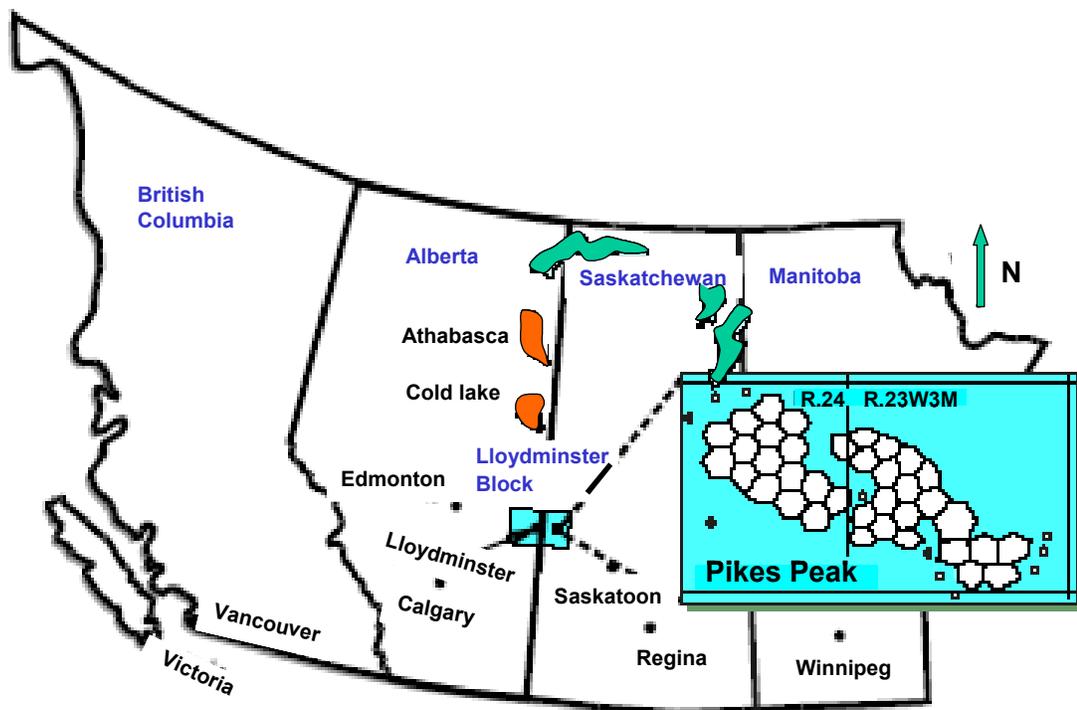
Figure 1.1 The location of Pikes Peak area (adopted from Wong et al, 2001)

After limited primary production, Husky started using Cyclic Steam Stimulation (CSS) technology in 1981 with subsequent conversion to Steam Drive (mostly in the western part of Pikes Peak area in 1984). The good thermal efficiency of this project is reflected

in the cumulative SOR (steam oil ratio) of 2.72 m^3/m^3 and current oil recoveries of up to

70% in the more mature steam-flooded areas. The total oil recovery is 6.56 X 10^6 m^3

(40% of the original oil-in-place) to the end of July 2001 (Wong et al, 2001). The project

was initiated with the intent of recovering 25 to 30% of the 16 X 10^6 m^3 original oil-in-

place.
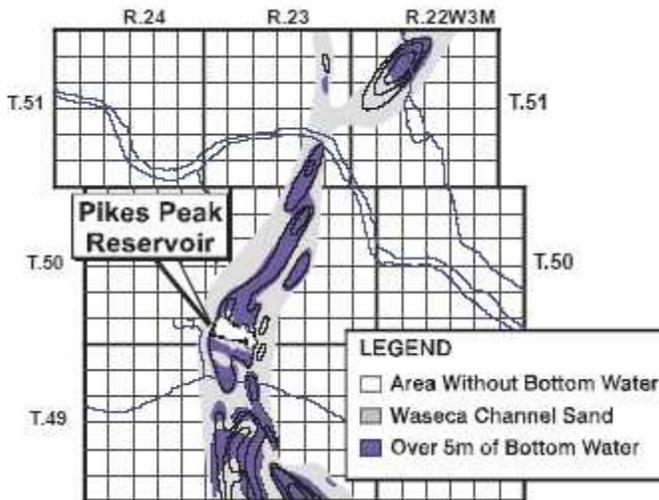
Figure 1.2 Pikes Peak Waseca channel sand complex (adapted from Wong et al, 2001)

AGE / GROUP		FORMATION	LITHOLOGY	APPROX. DEPTH
QUATERNARY		GLACIAL DRIFT		
CRETACEOUS UPPER	COLORADO GROUP	JUDITH RIVER		- 150 m -
		LEA PARK	SHALE	
		SECOND WHITE SPECS BASE OF FISH SCALES		- 300 m -
CRETACEOUS LOWER	MANNVILLE GROUP	VIKING		
		JOLI FOU		- 450 m -
		COLONY		
		MCLAREN		- 475 m -
		WASECA		- 510 m -
		SPARKY	SANDSTONE & SHALE	
		GENERAL PETROLEUM		
		REX		
		LLOYDMINISTER		- 550 m -
		CUMMINGS		
		DINA		- 650 m -
DEVONIAN	SASK. GROUP	DUPEROW	DOLOMITE	
	MANITOBA GROUP	SOURIS RIVER		- 825 m -
	ELK POINT GROUP	PRAIRIE EVAPORITE	EVAPORITE	- 950 m -
		WINNIPEGOSIS		
		ASHERN		- 1050 m -
CAMBRIAN		DEADWOOD		- 1600 m -
PRECAMBRIAN				

Figure 1.3 Pikes Peak stratigraphic chart (adapted from Watson and Lines, 2003)

1.3.2   Previous research work for the Pikes Peak field

The earlier works about Pikes Peak field has been presented by the personnel from Husky

Energy Ltd. Van Hulten (1984) provided a detailed geological background for the

Waseca Formation of Pikes Peak area. Sheppard et al. (1998) and Wong et al. (2001)

reviewed the reservoir engineering history and the field development information.

Several research results were published based on the acquisition and processing of the

March 2000 vertical array (conventional P wave survey), multi-component seismic data,

and September 2000 multi-component vertical seismic profile (VSP) data (Hoffe et al.,

2000, Stewart et al., 2000, Xu, 2001). Hedlin et al. (2001) investigated the seismic

attenuation through the steamed reservoir and suggested that the high frequency

attenuation by steamed reservoir may help delineate the extent of the steam flood.

Downton and Lines (2000) examined the feasibility of AVO time-lapse analysis and they

found a fluid factor anomaly on the 2000 line associated with the steam injection. The

work of Zhang (2003) showed that a joint inversion on the P-P and P-S (converted wave)

data has better resolution than conventional PP inversion. Zou et al. (2002) performed

synthetic modeling using the time-lapse model based on estimated steam zones and

shown similarities in the seismic difference and the time-delay to the real data analysis by

Watson et al. (2002). Watson (2004) highlighted the Vp/Vs variation after production

from multi-component data and also presented bottom water thickness estimation from

seismic interpretation.

1.3.3   Area of interest and available data for this study

The study area for this thesis is in the eastern part of the Pikes Peak area. A successful

CSS started in 1983 in this part of the reservoir. Husky acquired 2-D seismic surveys in

1991 that form grids of 29 north-south lines spaced every 100 meters over the Pikes Peak

area. In 2000, the University of Calgary and Husky acquired a repeat line on the eastern

side of the field (Figure 1.4). The honey-comb shapes in Figure 1.4 are entire seven point

steam drive pattern. Most wells around the time-lapse seismic lines are CSS wells. This

thesis will focus on the profile where this time-lapse seismic data sits.

The available well logs for this study are P-sonic and density logs from four wells, 1A15-

6, D15-6, 3C8-6, and 1D2-6 the locations of which are shown in Figure 1.4. Well 1A15-6

is the only well that has S sonic log. Figure 1.5 shows the logs from 1A15-6. The density

and gamma ray logs clearly show the homogenous sand zone. A 5-sample median filter

was applied to all the logs to filter spikes and then they were tied to the processed seismic

sections. The original field data and survey files of the two time-lapse seismic 2D lines were available for this study. The detailed information will be introduced in the processing section (Chapter 3). An initial reservoir model and the production history files of a partial Pikes Peak field were provided by Husky Energy Ltd for the reservoir simulation. Laboratory test results by Core Laboratories for the cores from well D2-6 are also available for this study (Core Laboratories, 2000).
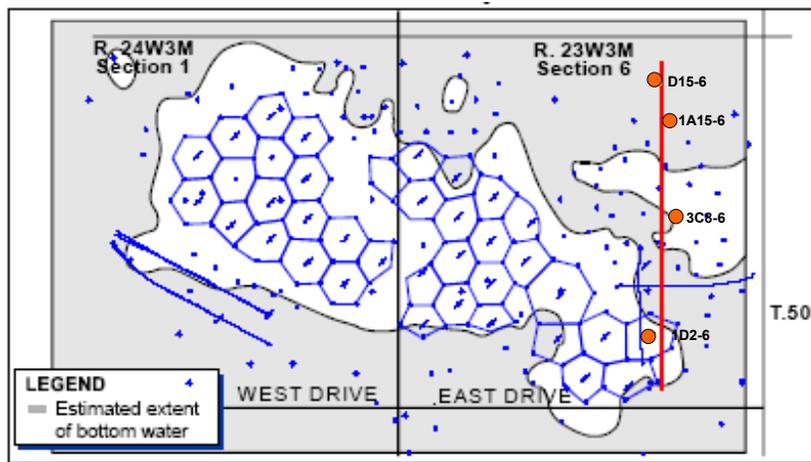
Figure 1.4 Map of the time-lapse seismic survey location (red line) (modified from Wong et al, 2001). The honey-comb shape is seven point steam drive pattern. Most wells around seismic line are CCS wells.

Figure 1.5 Logs from well 1A15-6 (median filtered). The partial logs from 465 to 500 m are shown here.

1.4 Dissertation Outline

In this thesis geophysics, rock physics, and reservoir simulation are combined to interpret time-lapse seismic surveys and to provide a way to integrate geophysics and reservoir engineering to optimize reservoir model. The study area is the east part of the Pikes Peak heavy oil field which is under CSS process for 20 years. However, the procedure can be applied to any thermal recovery field. This thesis includes the following four aspects.

   a. Rock physics

Rock physics links reservoir properties and seismic properties. Gassmann's equation (Wang and Nur, 1992) relates seismic property with rock and fluid properties. Several well-developed empirical relations will be used to calculate fluid density and modulus from reservoir parameters (Batzle and Wang, 1992). After applying above equations, the saturated rock bulk modulus, shear modulus, and saturated bulk density will be obtained,

and thereby compressional velocity and shear velocity can be derived. This dissertation will develop a procedure to implement the above task using a Matlab program. The detailed procedure is in Chapter 2.

    b.   Seismic survey processing

Identical seismic processing sequences will be applied to the two 2D time-lapse lines and presented in Chapter 3. The processing methods will be investigated to get optimized final stacks. Besides seismic amplitude difference section, AVO and inversion analysis will be conducted for both seismic surveys as discussed in Chapter 6. We will find the areas of the production footprints comparing the results before production and after production.

    c.   Reservoir simulation

In order to understand the whole picture of reservoir changes and to get reservoir pressure, temperature, and fluid saturation data at different stages of production, reservoir simulations will be carried out in Chapter 4. Chapter 4 will show the distributions of reservoir pressure, temperature and fluid saturations at different production stages.

    d.   Seismic modeling

Based on a. and c. we can calculate the distributions of bulk and shear moduli and densities, and then the distributions of velocity and density for the reservoir. In Chapter 5, the synthetic seismic sections, corresponding to the two time-lapse seismic survey times, are going to be generated. The mismatch between the difference stacks from synthetic modeling and real seismic surveys (which is the subtraction of the pre production section from the post production section) will be analysed in Chapter 6 in terms of processing error, reservoir model limitations, bypassed oil, and steam zones.

1.5   Software summary

The author developed the rock physics procedure using the Matlab programming code. The seismic processing was done by the author using Kelman Technologies's in-house processing software. The author implemented the reservoir simulation using Computer Modelling Group's commercial reservoir simulator STARS. The seismic modeling was done using Landmark's Promax processing tool. The time-lapse seismic analysis, well log editing, AVO modeling and analysis, and inversion were carried out using the Pro4D, Elog, AVO, and STRATA in Hampson-Russell's Geoview package. ACCUMAP archive system was used to retrieve log information and well distribution maps.

1.6   The significant contribution of this thesis

There is no published work that integrates seismic survey image, reservoir simulation, and seismic modeling together for a multiple well CSS heavy oil reservoir to the extent that this work does. The procedure to convert the outputs of reservoir simulation to seismic velocities and densities is significant for the integration of geophysics and reservoir engineering. It is the first time that all of the integrated works, seismic processing, reservoir simulation, rock physics procedure development, seismic modeling, and integrated interpretation, were done by one author. The working flow and the Matlab code can be used for other integrate projects between geophysics and reservoir engineering fields.

Chapter Two: Rock physics study

2.1   Introduction

In Chapter 1, we have discussed the need to convert the output of reservoir simulation to

seismic velocity and density models to generate synthetic seismic sections. To

accomplish this task we need rock physics equations to transfer the engineering

parameters to seismic parameters. Seismic velocities are expressed as following:

$$V_p = \sqrt{\frac{K_u + \frac{4}{3}\mu}{\rho_u}} \tag{1}$$

$$V_s = \sqrt{\frac{\mu}{\rho_u}} \tag{2}$$

Equation (1) is the compressional (or P) velocity, which is the velocity for the particle

motion parallel to the direction of propagation. Equation (2) is the shear (or S) velocity

which is the velocity for the particle motion perpendicular to the direction of propagation.

K_u is the saturated (undrained) rock's bulk modulus, μ is the saturated rock's shear

modulus, and ρ_u is the saturated rock's density. Wang and Nur (1992) developed a series

of empirical equations to calculate fluid seismic velocities and densities utilizing

reservoir engineering parameters. From the fluid seismic velocity and density we can

derive the fluid bulk modulus. Through Gassmann's equation (Wang and Nur, 2000) the

saturated rock bulk modulus (K_u) can be derived. The saturated rock density (ρ_u) can be

obtained by a simple equation (equation (5) in 2.2). This chapter will focus on the

procedure of applying rock physics theory. The regression of the relationship between

dry rock bulk modulus and shear modulus with temperature and pressure will also be presented here.

2.2 Theory and methodology

The well-known Gassmann's equation relates the bulk modulus of a saturated rock (K_u) to the dry rock bulk modulus (K_d), the solid grain bulk modulus (K_s), the fluid bulk modulus (K_f) and the porosity ϕ (Wang and Nur, 1992).

$$K_u = K_d + \frac{(1 - K_d / K_s)^2}{\dfrac{\phi}{K_f} + \dfrac{1-\phi}{K_s} - \dfrac{K_d}{K_s^{\,2}}} \tag{3}$$

The basic assumptions in the Gassmann's equation are: 1) the rock or porous medium is macroscopically homogeneous and isotropic; 2) all the pores are interconnected or communicating; 3) the pores are filled with a frictionless fluid (including gas); 4) the rock-fluid system under study is closed (undained); 5) the relative motion between the fluid and the solid rock is negligibly small compared to the motion of the saturated rock itself when the rock is excited by a wave; and 6) the pore fluid does not interact with the solid in a way that would soften or harden the frame (Wang and Nur, 2000). For heavy oil saturated unconsolidated sands, assumption 2) is very well satisfied but assumption 3) is violated. Wang and Nur compared laboratory data with Gassmann's predictions and their work shows that for the sands and sandstones under low effective pressure (10Mpa), the Gassmann-calculated Vp is lower than the measured Vp by as much as 8%. Since there is no other effective equation available so far, Gassmann's equation is the only choice for this study for the rock physics procedure. . Therefore, we have to keep in mind that there may be errors caused by this rock physics procedure.

We know that P and S wave velocities can be obtained from saturated rock density, saturated rock bulk modulus, and shear modulus. From reservoir engineering we know the following equations:

$$\rho_f = S_g \rho_g + S_o \rho_o + S_w \rho_w \tag{4}$$

$$\rho_u = \rho_s(1-\phi) + \rho_f \phi \tag{5}$$

Here ρ_o, ρ_g, ρ_w, ρ_s, ρ_u, and ρ_f are the densities of oil, gas, water, solid grains, saturated reservoir rock, and fluid mixture at reservoir condition, respectively. S_g, S_o, S_w, are the saturations of gas, oil, and water, and they are from the reservoir simulation for this study. We need to calculate ρ_o, ρ_g, and ρ_w at the reservoir condition to get ρ_f and to calculate the adiabatic gas, oil, and water bulk modulus K_g, K_o, and K_w using the equations developed by Batzle and Wang (1992) based on the known reservoir pressure(P), temperature(T), gas specific gravity(G), and water salinity(S).
For gas,

$$\rho_g = \frac{28.8 GP}{ZRT_a} \tag{6}$$

Where

$$Z = [0.03 + 0.00527(3.5 - T_{pr})^3 P_{pr} + (0.642 T_{pr} - 0.007 T_{pr}^4 - 0.52) + E$$

$$E = 0.109(3.85 - T_{pr})^2 \exp\{-[0.45 + 8(0.56 - 1/T_{pr})^2]P_{pr}^{1.2}/T_{pr}\}$$

$$P_{pr} = P/(4.892 - 0.4048G), \qquad T_{pr} = T_a/(94.72 + 170.75G)$$

T_a is the absolute temperature ($T_a = T(^oC) + 273.15$) and G is gas specific gravity. The units I used: MPa for pressure and bulk modulus; g/cm^3 for density; ^oC for temperature; m/s for velocity; and liters/liter for gas to oil ratio.

$$K_g = \frac{P}{(1 - \frac{P_{pr}}{Z} \frac{\partial Z}{\partial P_{pr}})_T} \gamma \tag{7}$$

Where small T means to do partial differentiation with respect to P, and

$$\gamma = 0.85 + \frac{5.6}{(P_{pr} + 2)} + \frac{27.1}{(P_{pr} + 3.5)^2} - 8.7 \exp[-0.65(P_{pr} + 1)]$$

For oil,

$$\rho_o = \frac{\rho_t^p}{B_o}(1 + 0.001 R_G)^{-1} \tag{8}$$

$$B_o = 0.972 + 0.00038[2.49 R_G (\frac{G}{\rho_o})^{1/2} + T + 17.8]^{1.175}$$

$$\rho_t^p = \rho_p /[0.972 + 3.81 X 10^{-4}(T + 17.78)]^{1.175}$$

$$\rho_p = \rho_o^{St} + (0.00277P - 1.71 X 10^{-7} P^3)(\rho_o^{St} - 1.15)^2 + 3.49 X 10^{-4} P$$

$$V_o = 2070(\frac{\rho_o}{2.6 - \rho_o})^{1/2} - 3.0T + 4.64P + 0.0115[4.12(1.08\rho_o^{-1} - 1)^{1/2} - 1]TP \tag{9}$$

ρ_o^{St} is oil density at standard condition (15.6°C and atmospheric pressure). V_o is oil P (compressional) velocity. R_G is gas oil ratio at standard condition. For Pikes Peak field, R_G was interpolated using the measured values provided by Husky Energy for different temperature and pressure.

For water,

$$\rho_w = \rho_{pw} + S\{0.668 + 0.44S + 10^{-6}[300P - 2400PS + T(80 + 3T - 3300S - 13P + 47PS)]\} \tag{10}$$

Where

$$\rho_{pw} = 1 + 10^{-6}(-80T - 3.3T^2 + 0.00175T^3 + 489P - 2TP +$$
$$0.016T^2P - 1.3X10^{-5}T^3P - 0.333P^2 - 0.002TP^2)$$

$$V_w = V_{pw} + S(1170 - 9.6T + 0.055T^2 - 8.5X10^{-5}T^3 + 2.6P$$
$$- 0.0029TP - 0.0476P^2) + S^{1.5}(780 - 10P + 0.16P^2) - 1820S^2$$

(11)

Here S is water salinity (the weight fraction of sodium chloride, ppm/1000000).

Here V_w is P (compressional) velocity for water, and

$$V_{pw} = \sum_{i=0}^{4}\sum_{j=0}^{3}W_{ij}T^iP^j \quad \text{is P velocity for pure water, and}$$

W_{00}=1402.85, $\quad W_{02}$=3.437X10^{-3}, $\quad W_{10}$=4.871, $\quad W_{12}$=1.739X10^{-4},

W_{20}= -0.04783, $\quad W_{22}$= -2.135X10^{-6}, $\quad W_{30}$=1.487X10^{-4}, $\quad W_{32}$= -1.455X10^{-8},

W_{40}= -2.197X10^{-7}, W_{42}= 5.23X10^{-11}, $\quad W_{01}$=1.524, $\quad W_{03}$= -1.197X10^{-5},

W_{11}= -0.0111, $\quad W_{13}$= -1.628X10^{-6}, $\quad W_{21}$=2.747X10^{-4}, $\quad W_{23}$= 1.237X10^{-8},

W_{31}= -6.503X10^{-7}, W_{33}= 1.327X10^{-10}, $\quad W_{41}$=7.987X10^{-10}, $\quad W_{43}$= -4.614X10^{-13}

After applying equation (6) to (11), from (4) ρ_f is calculated and from (5) undrained rock bulk density ρ_u can be derived.

To calculate the saturated rock bulk modulus using the Gassmann's equation, we need to know the moduli in the right side of Gassmann's equation (3). Average values of ϕ (0.32) from core tests and K_s (38 GPa) from published quartz bulk modulus (Wang and Nur, 2000) (were used in this study. The bulk modulus for oil and water is based on equation (9) and (11). It is assumed that fluids do not affect the estimated shear modulus (that is $\mu_o=\mu_g=\mu_w=0$). K_g, K_o, and K_w can be calculated by $K=Vp^2*\rho$, Vp is P velocity of fluids.

The average fluid bulk modulus for a multiphase system depends on the fluid distribution. The equations from Mavko and Mukerji (1998) were used to calculate combined fluid bulk modulus. The bounding values are:

$$\frac{1}{K_{f1}} = \frac{S_g}{K_g} + \frac{S_o}{K_o} + \frac{S_w}{K_w} \qquad (12)$$

$$K_{f2} = S_g K_g + S_o K_o + S_w K_w \qquad (13)$$

Equation (12) is for the homogeneous fluid distribution and equation (13) is for the patchy fluid distribution. The average of these two values was used for K_f in the following calculation. The remaining unknown in Gassmann's equation is K_d. It was assumed that K_d does not vary with different fluid saturation, but it is affected by effective pressure P_e (over burden pressure minus pore pressure) and temperature. The same assumption is applied to the shear modulus. Consequently the undrained shear modulus μ_u equals the dry shear modulus μ_d.

Given the P-wave, S-wave, and density logs before production, the undrained bulk modulus, K_u, and the shear modulus, μ_u, can be calculated (from equation (1) and (2)):

$$K_u = \rho_u^c (V_p^2 - \frac{4}{3} V_s^2) \qquad (14)$$

$$\mu_u = \rho_u^c V_s^2 = \mu_d = \mu \qquad (15)$$

ρ_u^c is the corrected log density. Since we know fluid saturation, pressure, and temperature before production, the corresponding K_f can be calculated from equations (6) to (13). Therefore from Gassmann's equation (3) and equation (15), K_d and μ can be obtained for the pre-production reservoir condition.

In the time-lapse calculation, we need to update K_d for effective pressure and temperature changes. The development of a relationship of K_d and μ_d with temperature and pressure will be discussed in 2.3.3. Here are the derived empirical relationships for the Pikes Peak field (P_e is in Pascal and T is in degrees centigrade):

$$dK_d = 141.18dP_e - 2.57dT \qquad\qquad (16)$$

$$d\mu = 7.08dP_e - 2.96dT \qquad\qquad (17)$$

After production, reservoir pressure, temperature, and saturation will change. From equation (16) and (17) K_d and μ_u are updated first, then K_f, and ρ_u for post-production conditions will be calculated from equation (6) to (13). Then the new K_u, V_p, and V_s corresponding to the post-production condition can be obtained from equations (3), (1) and (2), respectively.

2.3   Laboratory data analysis

2.3.1   Laboratory experiments for Pikes Peak area

In 2000, Core laboratory Canada Ltd did a series of tests for the University of Calgary. Acoustic velocity measurements were done on 38.1 mm diameter vertical unconsolidated heavy oil core samples from Husky Pikes Peak D2-6-50-23 W3M well, consisting of Waseca Sands Formation in the Pikes Peak field. The original goal of the tests was to study the effects of temperature, effective pressure and steam flooding on the acoustic response of the subject cores. These results were used to verify the fluid substitution procedure and also to derive relationships of K_d and μ_u with pressure and temperature. The magnitudes of the values of velocities from lab tests (around 2070 m/s with heavy oil saturation at room temperature) are much smaller than the values from the well logs

(around 2650 m/s in oil zone). However, if there are consistent gradients for all the lab tests, we will assume that an average trend exists, since we do not have an alternative. Therefore, the derived gradients of K_d and μ with pressure and temperature from lab tests were applied to in-situ reservoir rocks.

Five core samples were tested. The parameters of cores and the test procedure are listed as following:

a.   b.

Figure 2.1 One heavy oil core sample from well D2-6, a. saturated with heavy oil, b. after steam flooded (courtesy of Rob Stewart for the photo).

Sample 17A, OB27A, OB18, OB27B, and OB27C were punched as 38.1 mm diameter vertical cores from unconsolidated heavy oil cores from the Husky Pikes Peak D2-6-50-23 well (Figure 2.1 a.). The ultrasonic waves were generated by 1 MHz sound energy source. The sequence of events applied to the samples are:

1) 17A was mounted in a lead sleeve and all the oil was cleaned out in a hot toluene extractor. A further methanol cleaning was done to leach out any salt. After cleaning, sample 17A was frozen with liquid nitrogen and mounted in a high temperature sleeve with a fine screen at either end of plug to confine the sands. Flow heads, with compressional and shear transducers, were mounted in the sleeve on both ends of the sample, and the whole assembly was placed in a pressure vessel. An effective pressure of 0.7 MPa was established, and sufficient time allowed for the sample to equilibrate before acoustic velocity measurements were made at a temperature of 25^oC. Compressional and shear wave velocity measurements were done at ten additional overburden pressures. Sufficient time was allowed for achieving equilibrium at each pressure, which was confirmed by monitoring the compressional wave travel time.

2) OB27A was frozen with liquid nitrogen and mounted in a high temperature sleeve with a fine screen at either end of the plug to confine the sands. Flow heads, with compressional and shear transducers, were mounted in the sleeve on both ends of the sample, and the whole assembly was placed in a pressure vessel. A nominal confining pressure was applied to the sample and a vacuum was drawn on the sample. Spun dead crude from the D2-6-50-23 well was flowed through the sample to remove any trapped air and degraded in-situ oil in the sample. A reservoir effective pressure of 9.2 MPa and a pore pressure of 2.2 MPa was established and sufficient time was allowed for the sample to equilibrate at ambient temperature ($\sim22^o$C). Compressional and shear wave velocity measurements were done at six additional temperatures, while maintaining the reservoir effective pressure of 9.2

MPa and pore pressure of 2.2 MPa. Sufficient time was allowed for achieving equilibrium at each temperature, which was confirmed by monitoring the compressional wave travel time. After acoustic velocity measurements, fluid saturation in the sample was determined by Dean Stark extraction. Porosity and grain density of the sample were measured using helium porosimetry.

3) OB18 was tested as described in 2) for sample OB27A.

4) OB27B was frozen with liquid nitrogen and mounted in a high temperature sleeve with a fine screen at either end of the plug to confine the sands. Flow heads, with compressional and shear transducers, were mounted in the sleeve on both ends of the sample, and the whole assembly was placed in a pressure vessel. A nominal confining pressure was applied to the sample and a vacuum was drawn on the sample. Spun dead crude from the D2-6-50-23 well was flowed through the sample to remove any trapped air and degraded in-situ oil in the sample. A reservoir effective pressure of 14 MPa and a pore pressure of 2.2 MPa were established and sufficient time was allowed for the sample to equilibrate at ambient temperature ($\sim25^o$C). Compressional and shear wave velocity measurements were done at five additional overburden pressures, while maintaining the test temperature of 25^oC and pore pressure of 2.2 MPa. Sufficient time was allowed for achieving equilibrium at each pressure, which was confirmed by monitoring the compressional wave travel time. After acoustic velocity measurements, fluid saturation in the sample was determined by Dean Stark extraction. Porosity and grain density of the sample were measured using helium porosimetry.

5) OB27C was tested the same as in 4) for sample OB27B.

2.3.2 Lab test results and comparison with published results

The measured V_p and V_s for the five samples are plotted in Figure 2.2. Sample 17A, in a

clean and dry state, was tested to study the effect of effective pressure on V_p and V_s. The

measurements were done at the temperature of 25^oC (Figure 2.2. a.). Sample OB27A

(Figure 2.2. c.), with 0.79 heavy oil saturation and connate water 0.21, and sample OB18

(Figure 2.2. b.), with 0.76 heavy oil saturation and connate water 0.24, were tested to

study the effect of temperature on V_p and V_s. The measurements were done at effective

pressures of 9.2 MPa. Sample OB27B, with 0.73 heavy oil saturation and connate water

0.27, was tested to study the effect of pressure on V_p and V_s. The measurements were

done at the temperature of 25^oC (Figure 2.2. d.). Sample OB27C, with 0.78 heavy oil

saturation and connate water 0.22, was tested to study the effect of pressure on V_p and V_s.

The measurements were done at the temperature of 100^oC (Figure 2.2. e.). The pore

pressures were maintained at 2.2 MPa for all the tests with heavy oil saturation. The

experimental results show that the V_p and Vs of the heavy oil saturated unconsolidated

Waseca sand increase with effective pressure and decrease with temperature. To

investigate this trend further we also plotted other researchers' results (Wang and Nur,

1986, Wang et al, 1988) in Figure 2.3 a. and b. for the Ottawa sand. The properties of the

Waseca sand and the Ottawa sand are very similar and they are listed in Table 2.1 for

comparison.
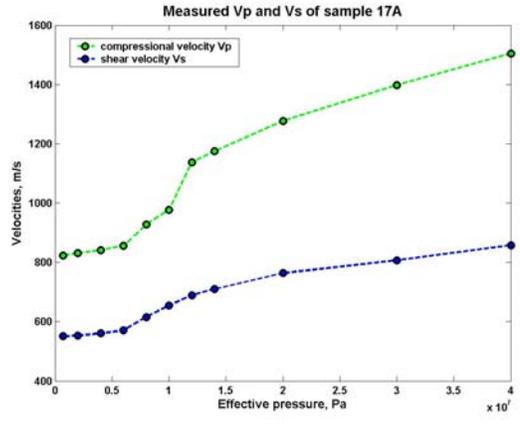
a.
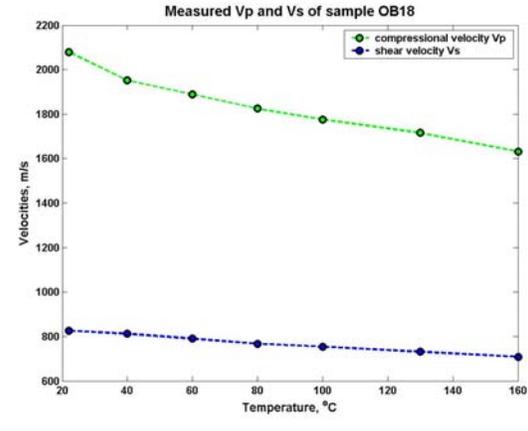
b.
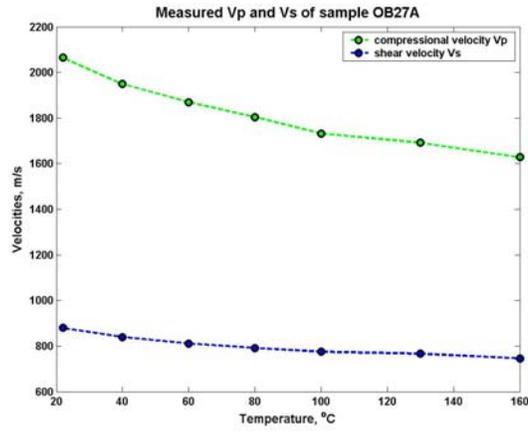
c.
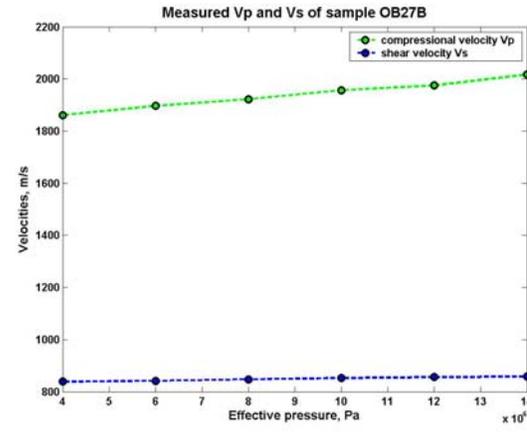
d.
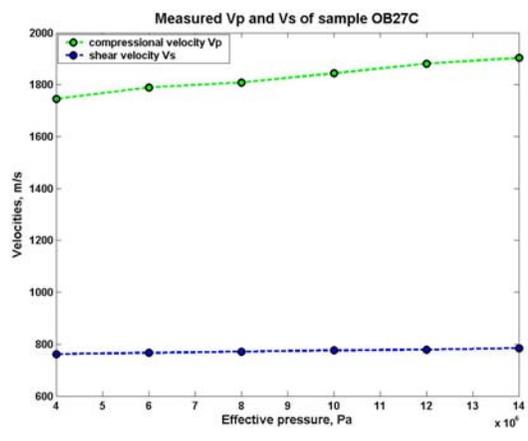
e.

Figure 2.2 Lab measured compressional and shear velocities for sample 17A(a), OB18(b), OB27A(c), OB27B(d), and OB27C(e).

Table 2.1. Comparison between Waseca Sand and Ottawa Sand.

	Porosity	Permeability(md)	Grain density(km/m3)
Waseca Sand	0.32 – 0.36	5000	2650
Ottawa Sand	0.37	3000	2650

a.   b.
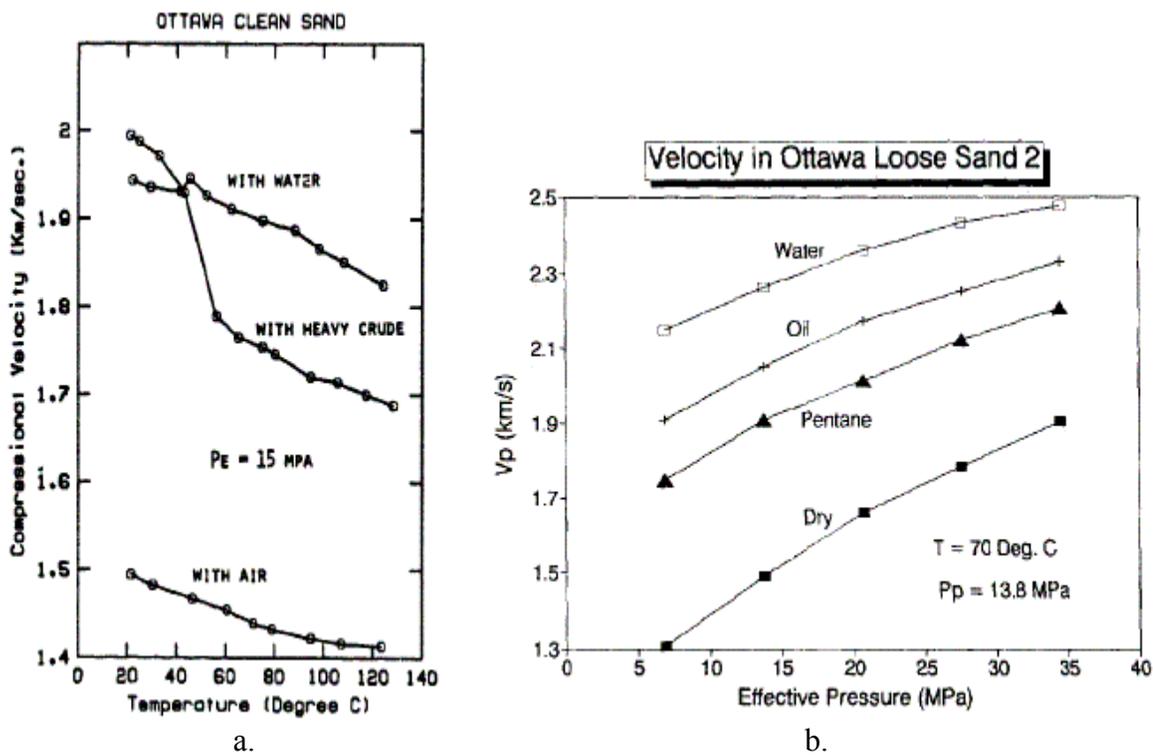
Figure. 2.3 Lab measured compressional and shear velocities for Ottawa unconsolidated sand. a. V_p vs. T, effective pressure P_e=15 MPa, after Wang and Nur, 1986, b. V_p vs. P_e, T=70°C, after Wang et al, 1991.

From Figure 2.2 b (with constant effective pressure 9.2 MPa) and c (with constant temperature 100°C) for the Waseca sand, we can work out that the V_p decreases about 9.5% when temperature changes from 20°C to 60°C, and another 9% decrease when temperature changes from 60°C to 130°C. From Figure 2.3 a. for the Ottawa sand with heavy crude, the decrease is 11% when temperature change from 20°C to 60°C, and a

4.5% decrease when temperature changes from 60°C to 130°C. The Ottawa sand is very

similar to the Waseca sand from Table 2.1 and the amount of change from 20°C to 60°C

is very close. The difference of the V_p decrease when temperature changes from 60°C to

130°C may in part be due to the difference in the effective pressure of the two tests. For

Vp changing with pressures, Figure 2.2 a for the Waseca sand in dry condition gives a

50% Vp increase when effective pressure changes from 8 Mpa to 30 Mpa. For the Ottawa

sand in dry condition, Figure 2.3 b gives only a 33% increase for the same effective

pressure change. Part of the mismatch could be caused by the temperature difference

between the tests. For Figure 2.2 a. the temperature is 25°C and for Figure 2.3 the

temperature is 70°C.

Through the comparison between the tests on the Waseca sand and the tests on the

Ottawa sand, we have shown that the tests on Waseca Sand are in a reasonable range.

2.3.3 Dry bulk modulus and shear modulus change with effective pressure

To study the change of dry bulk modulus, K_d, and shear bulk modulus, μ ($\mu=\mu_d=\mu_u$), with

temperature and effective pressure, P_e, the lab measured V_p, V_s, and other known

parameters were used to find the relationship. Since the fluid properties for the lab tests

are known, the measured K_d can be derived from measured V_p and V_s. Using equations

(14) and (15) in 2.3.2, from measured Vp and Vs, measured K_u and μ can be derived. The

bulk density is calculated by equation (5). From the known temperature, pressure,

porosity, grain density, and fluid saturations of the core samples and using equations (6)

to (13), K_f can be derived for the core samples. Through Gassmann's equation (3) in

2.3.2, K_d can be obtained for the corresponding temperature and pressure. The derived

results are listed as follows for all the samples:

For sample 17A, ρ_s is 2650 kg/m^3 and ϕ is 0.385. The calculated K_d and μ values are

listed in Table 2.2. The values were plotted in Figure 2.4 for K_d and μ with the fitted

lines. The correlation coefficient is 0.9752 for K_d and is 0.9779 for μ.

Table 2.2. Dry bulk modulus calculated from lab measured V_p and V_s for sample 17A.

$P_e(10^6Pa)$	0.7	2	4	6	8	10	12	14	20	30	40
$K_d(10^9Pa)$	0.449	0.462	0.472	0.488	0.581	0.622	1.08	1.16	1.39	1.77	2.09
$\mu(10^9Pa)$	0.494	0.498	0.512	0.531	0.618	0.699	0.774	0.821	0.95	1.06	1.2
Vp(m/s)	824	831	842	856	928	977	1138	1175	1277	1398	1505
Vs(m/s)	551	553	561	571	616	655	689	710	764	807	858
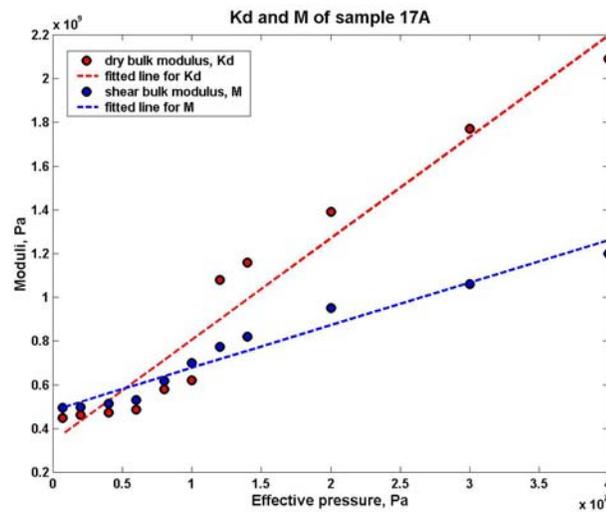
Figure 2.4 Dry bulk modulus and shear modulus and the fitted lines for sample 17A.

For sample OB27A, ρ_s is 2650 kg/m^3 and ϕ is 0.379. The calculated K_d and μ values are

listed in Table 2.3. The values were plotted in Figure 2.5 for K_d and μ with the fitted

lines. The correlation coefficient is -0.2983 for K_d and is -0.9505 for μ.

Table 2.3. Dry bulk modulus calculated from lab measured V_p and V_s for sample OB27A.

T(^{o}C)	22	40	60	80	100	130	160
Kd(10^9Pa)	1.1398	0.4365	0.2302	0.1683	0.0782	0.4415	0.5910
μ(10^9Pa)	1.5638	1.4208	1.3200	1.2546	1.1973	1.1639	1.0985
Vp(m/s)	2065	1949	1870	1804	1732	1692	1629
Vs(m/s)	880	840	811	792	775	766	746
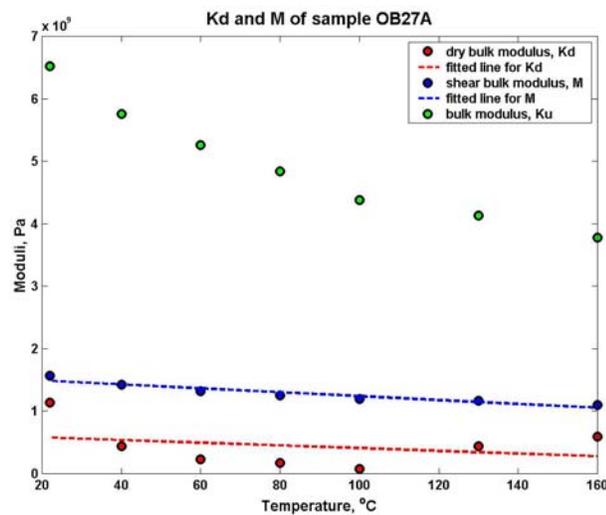
Figure 2.5 Dry bulk modulus and shear modulus and the fitted lines for sample OB27A.

For sample OB18, ρ_s is 2650 kg/m^3 and ϕ is 0.383. The calculated K_d and μ values are

listed in Table 2.4. The values were plotted in Figure 2.6 for K_d and μ respectively with

the fitted lines. The correlation coefficient is -0.3697 for K_d and is -0.9947 for μ.

Table 2.4. Dry bulk modulus calculated from lab measured V_p and V_s for sample OB18.

T($^{\circ}$C)	22	40	60	80	100	130	160
Kd(10^9Pa)	1.6728	0.6741	0.5652	0.5282	0.6060	0.8335	0.8022
μ(10^9Pa)	1.3732	1.3232	1.2483	1.1757	1.1294	1.0562	0.9886
Vp(m/s)	2079	1952	1888	1825	1776	1716	1632
Vs(m/s)	826	812	790	768	754	734	709
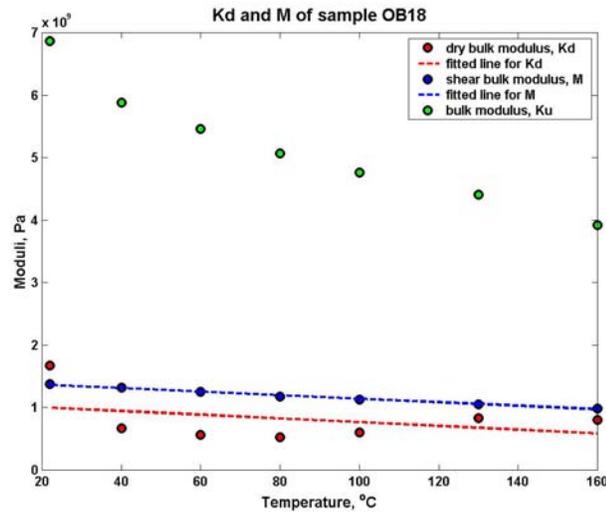
Figure 2.6 Dry bulk modulus and shear modulus and the fitted lines for sample OB18.

For sample OB27B, ρ_s is 2650 kg/m^3 and ϕ is 0.385. The calculated K_d and μ values are

listed in Table 2.5. The values were plotted in Figure 2.7 for K_d and μ respectively with

the fitted lines. The correlation coefficient is 0.9949 for K_d and is 0.9934 for μ. It can be

noted that the derived K_d numbers are negative for the lower three effective pressure.

This may be caused by either measurement errors or the limitations of the empirical

equations (6) to (13) in 2.3.2.

Table 2.5. Dry bulk modulus calculated from lab measured V_p and V_s for sample OB27B.

Pe(10^6Pa)	4	6	8	10	12	14
Kd(10^9Pa)	-0.7211	-0.3646	-0.1209	0.2120	0.3819	0.8302
μ(10^9Pa)	1.3732	1.3232	1.2483	1.1757	1.1294	1.0562
Vp(m/s)	1861	1897	1923	1957	1975	2017
Vs(m/s)	839	842	847	852	856	858
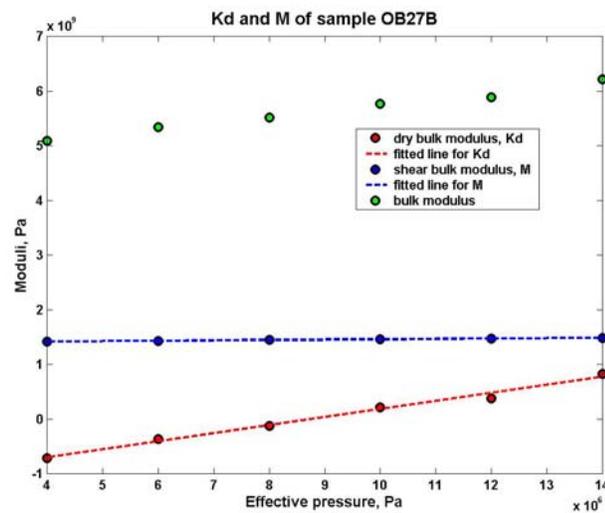
Figure 2.7 Dry bulk modulus and shear modulus and the fitted lines for sample OB27B.

Sample OB27C, ρ_s is 2650 kg/m^3 and ϕ is 0.371. The calculated K_d and μ values are

listed in Table 2.6. The values were plotted in Figure 2.8 for K_d and μ respectively with

the fitted lines. The correlation coefficient is 0.9954 for K_d and is 0.9975 for μ.

Table 2.6. Dry bulk modulus calculated from lab measured V_p and V_s for sample OB27C.

Pe(10^6Pa)	4	6	8	10	12	14
Kd(10^9Pa)	0.2288	0.6005	0.7633	1.0630	1.3980	1.5778
μ(10^9Pa)	1.1656	1.1809	1.1933	1.2088	1.2181	1.2370
Vp(m/s)	1745	1789	1809	1844	1881	1903
Vs(m/s)	762	767	771	776	779	785
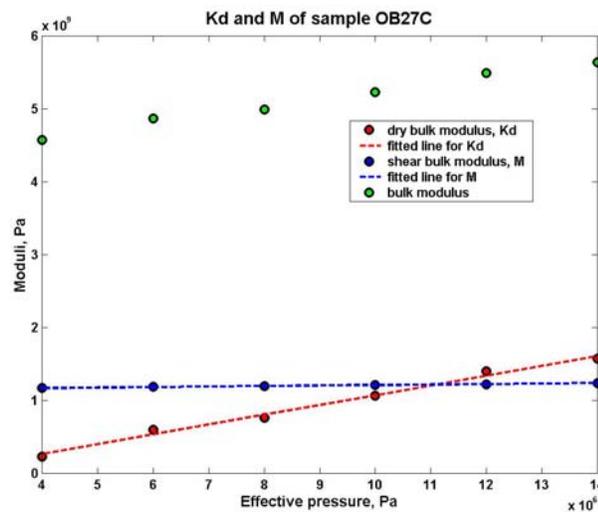
Figure. 2.8 Dry bulk modulus, shear modulus and the fitted lines for sample OB27C.

From above analysis on deduced K_d and μ values from measured Vp and Vs, it manifests

that the change of K_d and μ depending both on effective pressure P_e and temperature T.

To correctly work out the relationship, we should consider two variable problems. Figure

2.9 is the plots of all the lab data for K_d and μ in T and P_e domain.

From Figure 2.9, it is almost impossible to fit a 2D surface in P_e and T space. The

velocity values from sample 17A in dry condition are extremely low compared with the

saturated samples and this phenomenon is also shown in Figure 2.3 for the Ottawa sand in dry condition. It may be that the samples had been washed too much during the heavy oil extraction (Figure 2.1, b). Therefore, sample 17A was excluded for the curve fitting.
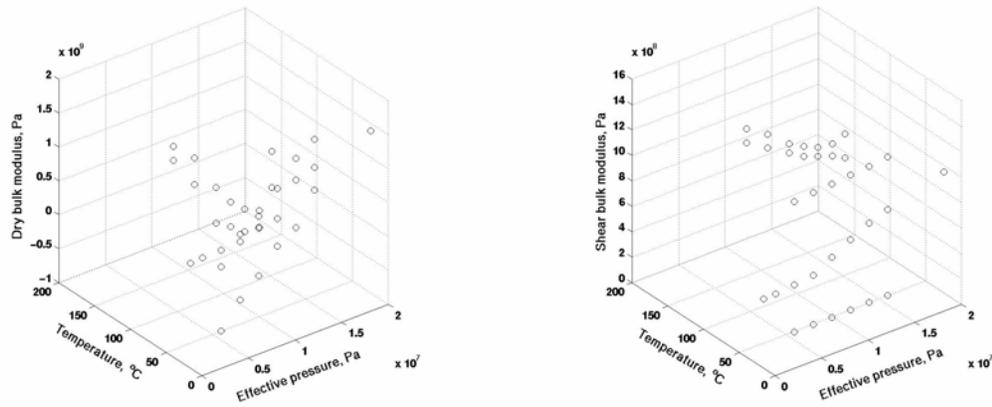
Figure. 2.9 Lab obtained K_d (left) and μ (right) in effective pressure and temperature space.

Figure 2.9 shows that although the intercept values for the different tests vary a lot for different samples, the gradients are similar for the tests. For tests at P_e=9.2 MPa with different temperatures:

From sample OB27A: dK_d=-2.16dT, $d\mu$=-3.1000*dT

From sample OB18: dK_d=-2.98dT, $d\mu$=-2.81dT

For tests at T=25 $^\circ$C and T=100 $^\circ$C with different effective pressures:

From sample OB27A: dK_d=147.54dP_e, $d\mu$=7.09dP_e

From sample OB18: dK_d=134.81dP_e, $d\mu$=7.06dP_e

Assuming K_d and μ change with T independent of P_e, then

$$dK_d = \frac{\partial K_d}{\partial P_e} dP_e + \frac{\partial K_d}{\partial T} dT$$

$$d\mu = \frac{\partial \mu}{\partial P_e} dP_e + \frac{\partial \mu}{\partial T} dT$$

After averaging the coefficients from different samples, the following relationships are obtained (equation (10) and (11) in 2.1):

$$dK_d = 141.18 dP_e - 2.57 dT$$

$$d\mu = 7.08 dP_e - 2.96 dT$$

The unit for P_e is MPa and for T is $^{\circ}$C.

These relationships are based on the test results and they were applied to the rock physics procedure (please refer to Chapter 2, 2.1 equation (16) and (17)) to modify K_d and μ with changing T and P_e.

2.3.4   Verification of rock physics procedure

To verify the validity of the rock physics procedure described in section 2.2.1, this procedure was applied on sample OB27A to calculate saturated bulk modulus at the seven temperatures using lab test pressure, temperature, fluid saturations, and other measured parameters in test 2). Through equation (6) to (11) fluid bulk moduli can be calculated. After this calculation K_d and μ for pressure and temperature change can be updated by equation (16) and (17). Finally, from equation (3), calculated K_u is obtained. The measured saturated bulk moduli were deduced using equation (4), (5), (14) and (15)

in section 2.3.2 from the measured grain density, porosity, fluid saturations, and

compressional and shear velocities in test 2). The calculated and the measured saturated

bulk moduli at different temperatures are plotted in Figure 2.10.

The standard deviation of the calculated values from the lab derived saturated bulk

moduli are -10%, 6%, 7%, 9%, 6%, 0.8%, and -1% respectively for temperature at 22^oC,

40^oC, 60^oC, 80^oC, 100^oC, 130^oC, and 160^oC. The results indicate that the procedure

developed for fluid substitution works very well on the laboratory data set.
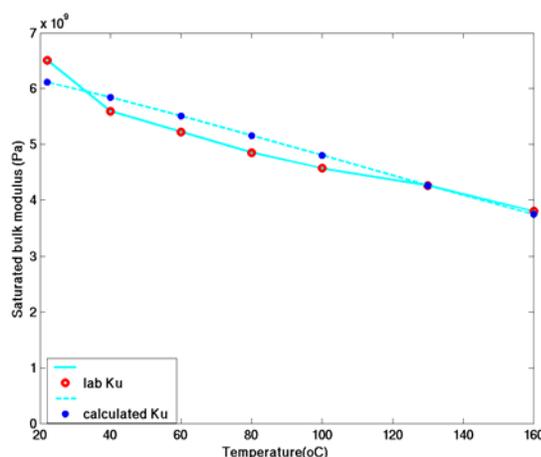
Figure 2.10 Calculated saturated bulk moduli vs. lab derived saturated bulk moduli.

2.4   Discussion

In the rock physics procedure of section 2.1, the common assumption that the saturated

shear modulus equals dry shear modulus was applied. This assumption may be

reasonable for light oil since light oil has very small viscosity. For heavy oil, the

assumption might bring some error because heavy oil has very high viscosity at lower

temperatures; although, viscosity decreases with temperature. The following paragraph gives some discussion on this issue.

If P_{ij} and E_{ij} are distortional stress and distortional strain tensors, respectively, for perfect elastic material the equation is:

$$P_{ij} = 2\mu E_{ij} \qquad (18)$$

and if we assume that rock saturated with heavy oil is the same as a combination of the perfect elasticity with the viscous fluid (Kelvin material in material mechanics, Bullen, 1963), equation (18) should be:

$$P_{ij} = 2\mu E_{ij} + 2v\frac{dE_{ij}}{dt} \qquad (19)$$

where v is the viscosity of heavy oil and μ is the shear bulk modulus of the rock matrix. If we assume $E_{ij}=A_{ij}\cos(2\pi t/T)$, here T is equivalent to the seismic period, then

$$P_{ij} = 2\mu A_{ij}\cos(\frac{2\pi t}{T}) + \frac{4v\pi A_{ij}}{T}\sin(\frac{2\pi t}{T}) \qquad (20)$$

If $\mu \gg v/T$ i.e. $v \ll T\mu$, the viscous effect would be unimportant. On the other hand, if $\mu \sim v/T$, the second term of equation (20) would become an effective rigidity on the order of μ. For the Pikes Peak case, average μ from dipole well logs is 4.5×10^9 Pa, and the cold heavy oil (18°C) viscosity is 25000 cp or 25 PaS. At 150°C, the heavy oil viscosity is around 0.01 PaS. For 50 HZ centre frequency seismic, the period T is 0.02 S. At 18°C, $v/T \sim 1.2 \times 10^3$ Pa and at 150°C $v/T \sim 0.5$ Pa; they are both much smaller than μ (4.5×10^9) Therefore, the effect of viscous on the application of elastic equation should not be significant.

2.5   Conclusions

The above sections have described the rock physics procedure that I used to convert the

reservoir engineering parameters to seismic velocities and densities. We need reservoir

pressure, temperature, porosity, fluid saturations, oil and gas gravity, gas oil ratio, water

salinity, and rock grain density to calculate saturated rock bulk modulus and density.

Some of the parameters are from reservoir simulation output and some of them are from

lab measurements. The laboratory results not only show the bulk modulus and shear

modulus increase with pressure and decrease with temperature, but also gave me a good

example to test the validity of the rock physics procedure. This procedure has been

written into a Matlab code and can be applied to other cases that need to transfer

engineering parameters to seismic parameters.

In the next Chapter, I will discuss seismic processing. Processed seismic profiles can give

us a general picture of underground structure.

Chapter Three: Time-lapse seismic processing

3.1   Introduction

Time-lapse seismic reservoir monitoring is a procedure to acquire, process, and interpret repeated seismic surveys at the same location but at different production stages. Seismic processing is a very important step as it is the foundation for the interpretation. The processing flow should be optimized to obtain high-quality seismic sections, to minimize non-reservoir related energy on the difference sections and maintain the true image differences caused by reservoir property change. To ensure that the image obtained at beginning time is comparable to subsequent images, identical field parameters and processing flows are necessary whenever possible. However, in many cases the legacy data existed before production or in the beginning stage of production. They were not designed for time-lapse analysis in some cases. Some time-lapse processing case studies have been published to pursue a better repeatability of time-lapse seismic surveys by optimum processing and cross-equalization steps (Rickett and Lumley, 2001, Johnston et al., 2000). Ross and Altan discussed the effect of offset and dead traces on the final difference section (Ross and Altan, 1997). Ross et al. (Ross et al., 1996) studied the impact of time delay, phase difference, and unequal amplitude on the final seismic difference sections.

The two time-lapse lines in this study were acquired 9 years apart and have different field parameters. A series of processing steps were implemented in order to get validly comparable images. Important issues for the processing of time-lapse seismic data are survey position accuracy, wavelet shape and spectral content, amplitude preservation, and time and phase match.

This chapter shows the processing procedure for obtaining a properly processed

difference section (which is the processed 2000 section minus the processed 1991

section). The important processing issues will be discussed at relative stages. The

different scaling methods will be compared for the two time-lapse seismic surveys.

Finally, the difference sections will be compared with production activities. The

difference section that best fits the production activities was selected as the final

difference section.

Table 3.1   Field parameters for 1991 and 2000 surveys.

	1991 Field Parameters	2000 Field Parameters
Date	February 1991	March 2000
Sweep length	6 Second	16 Second
Sweep bandwidth	8-110 Hz	8-150 Hz
Anti-alias filter	8-110 HZ nonlinear	3-164 HZ nonlinear
Source array	3 Vibs over 20 M	2 Vibs over 20 M
Vibroseis drag length	10 m	No drag
Geophone Freq.	14 HZ	10 HZ
Geophone Int.	20 M	20 M
Source Int.	40 M	20 M
Geophone array	9 over 20 M	6 over 20 M
Fold	30	66

3.2   The time-lapse seismic survey

Husky Oil acquired a set of 2D swath lines in north-south directions in 1991. To

investigate the time-lapse effects, the University of Calgary and Husky acquired a repeat

line on the eastern side of the field (Section 1.3.3, Figure 1.4). Figure 3.1 schematically

shows the relative locations between line H00-131 (2000 survey) and H91-76S (1991

survey); the two lines are about 5 meters apart. Please note that the scale in Figure 3.1 is not the same in X and Y direction. The distance between the two lines is much smaller than the seismic resolution and therefore the survey position accuracy is considered acceptable. A further discussion on the seismic resolution will be given in the discussion section. The field parameters for the two seismic surveys are listed in Table 3.1. The main difference for the field parameters between these two surveys are, sweep bandwidth, vibs drag length, and geophone array. The latter two factors are probably the main reasons for the larger ground roll noise in the 2000 survey.
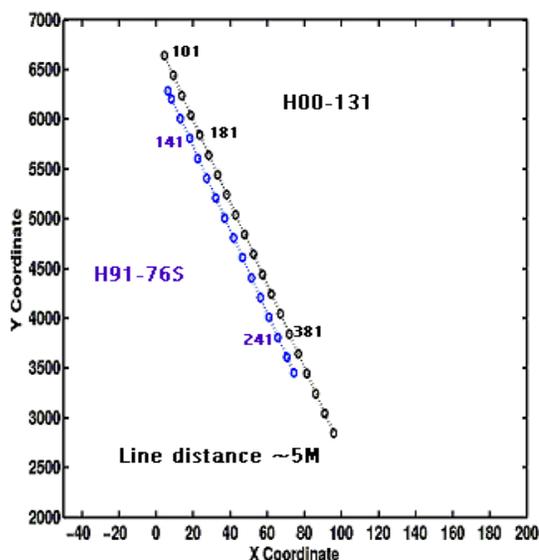
Figure 3.1 Relative locations between line H00-131 and H91-76S (The scale is not the same in X and Y directions).

Figure 3.2 shows one shot from each survey. The ground roll noise is on both the surveys and it is larger on the 2000 survey. During the survey for the 2000 line, the production activities were still going on, and noise created by the pumps from nearby wells is seen in Figure 3.2. The 1991 survey is not really a base survey because production started in

1983 in the southern part of the lines. The 1991 survey was used as the reference survey.

The detailed well activity will be shown in Chapter 4.
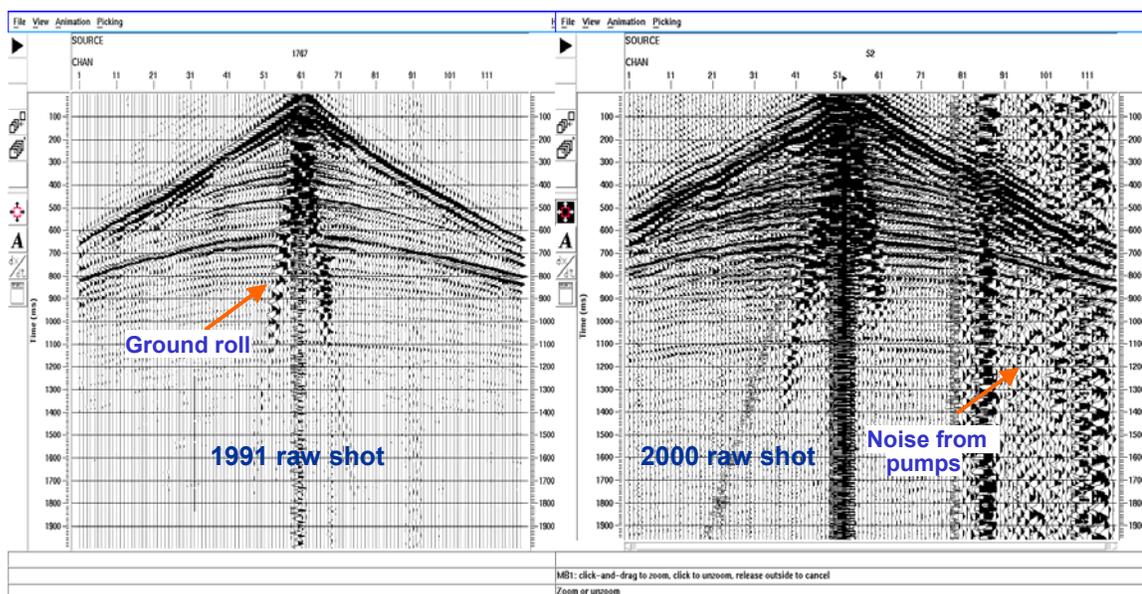
Figure 3.2 The raw shot from 1991 survey (left) and 2000 survey (right).

3.3   Processing flow

The two surveys were processed with the same processing flow using the processing

package of Kelman Technology Inc. Some graphs shown here are using Promax and

Hampson-Russell's Pro4D software. The basic processing flow is as follows:

Reformat,

Spherical gain recovery,

Geometry assignment and trace editing,

Surface consistent deconvolution,

Partial spectrum balance,

Weathering statics and surface consistent statics,

NMO and mute application,

TRIM statics,

Amplitude equalization,

Stacking,

Spectral balancing,

FX predictive decon,

Finite-difference migration,

Final bandpass filter,

Final amplitude equalization (scaling)

Phase match and time match (TRIM statics using 1991 as a model),

Difference plot.

Here some important steps are addressed:

A gain recovery for the spherical divergence correction was tested before its application on the data.

A surface consistent deconvolution was applied in order to obtain frequency enhanced and amplitude preserved results. It computes the operators for common shot, common receiver, common offset, and common CDP and this, in theory, will give consistent deconvolution results for the gathers with different local features. The following partial spectrum balance suppresses the anomalously high amplitudes for certain frequencies and then balances the amplitude spectrum.

Although the two surveys were both acquired in the winter, the weathering layer still could be different due to the different temperatures and environments each year. The weathering statics were calculated separately. The marker depth is around 200 ms in time

and is not exactly the same for the two surveys. Therefore, the replaced weathering layer will not have the same shape in the two surveys.

To make the two surveys as comparable as possible, I limited the shot and receiver offset to 1200 m, which is the far offset for the 1991 survey. The 2000 survey has offsets as large as 1320 m. The same mute was applied for both the surveys.

Because the weathering layer change could influence the deeper events, velocities were picked for each survey individually. Surface-consistent statics and residual statics (TRIM statics) were also calculated individually.

After stacking, another spectral balance was applied to further enhance the amplitude spectra. The amplitude spectra with pre-stack partial balance and the spectra with both pre-stack partial balance and post-stack balance for both surveys are plotted in Figure 3.3. The wavelet shapes for the two surveys matched very well on both pre-stack data and post-stack data. The post-stack spectrum balance has done a good job to balance the frequency content.

Before post-stack migration, FX predictive deconvolution was applied to reduce random noise. Post-stack finite difference migration was performed using stacking velocities. After post-stack migration, cross-correlation was done to check phase and time shift with a window from 250 ms to 450 ms which is just above the reservoir and below the weathering layer. After applying a global phase correction and time shift, TRIM statics was run for the 2000 stack using the 1991 stack as the model to adjust short-wave time-shift. At this stage final stacks were obtained. Then a difference section was generated which is the 1991 final stack subtracted from the 2000 final stack using Hampson-Russell's Pro4D software.
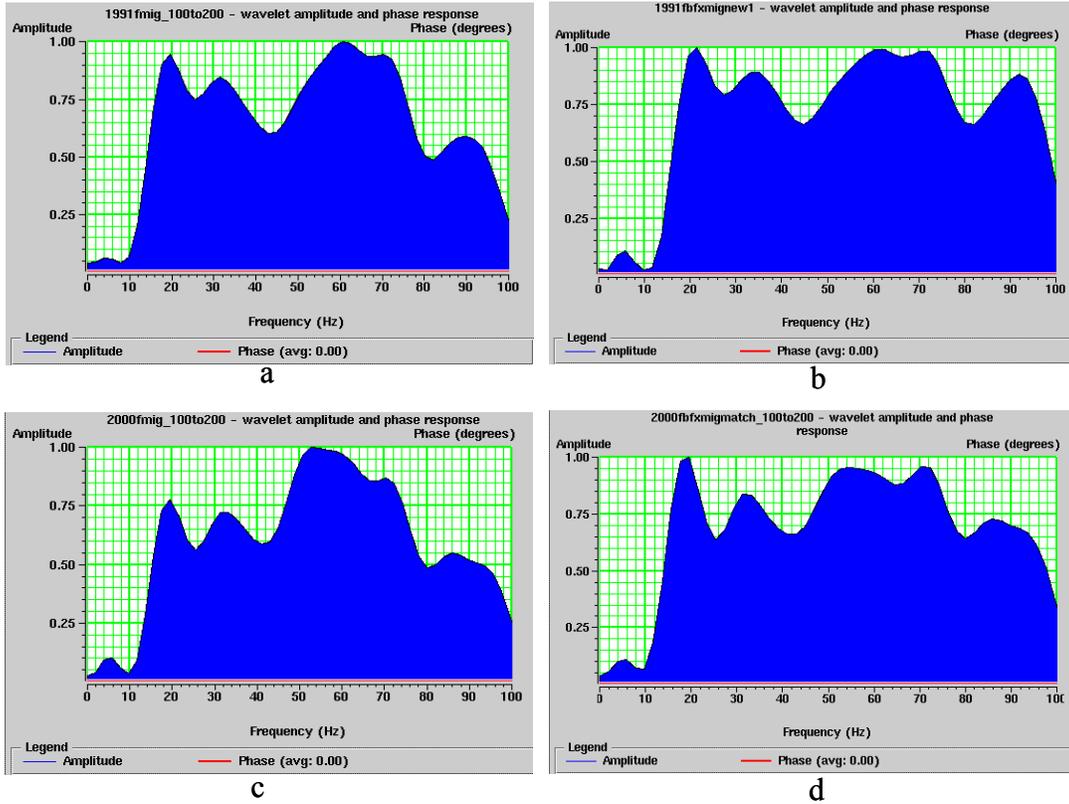
Figure 3.3 Amplitude spectra before and after post-stack balance. a & c: amplitude spectrum with pre-stack partial spectrum balance for the 1991 and 2000 survey respectively; b & d: amplitude spectrum with pre-stack partial spectrum balance and post-stack spectrum balance for the 1991 and 2000 survey respectivily.
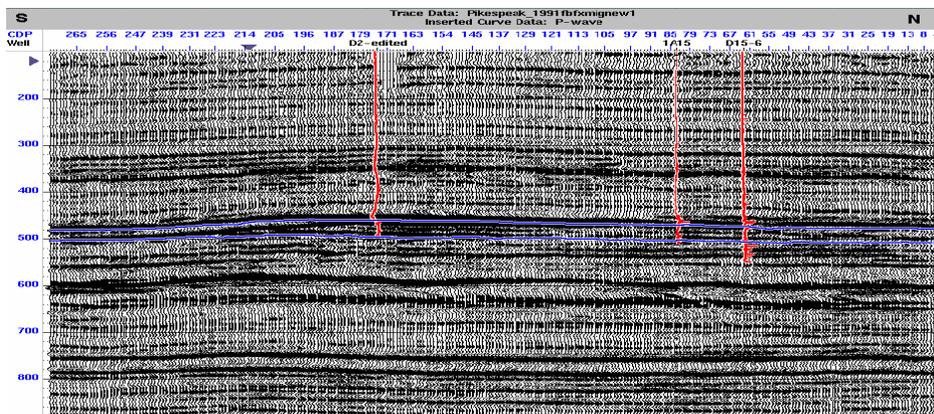
a.
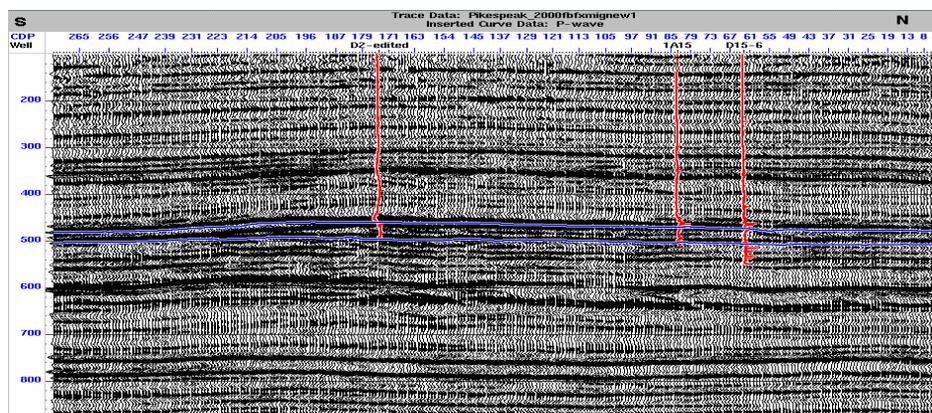
b.
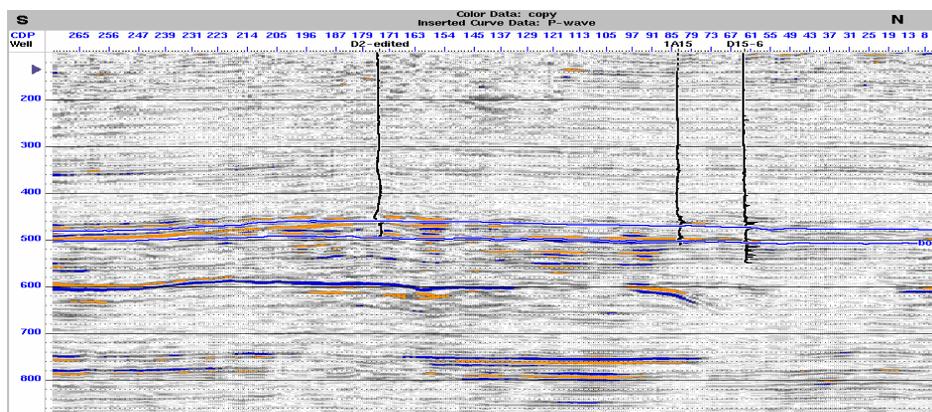
c.

Figure 3.4 Final migration stacks with conventional scaling for the 1991 survey (a.) and the 2000 survey (b.) and their difference (c), relative scale: orange is +1 and blue is –1.
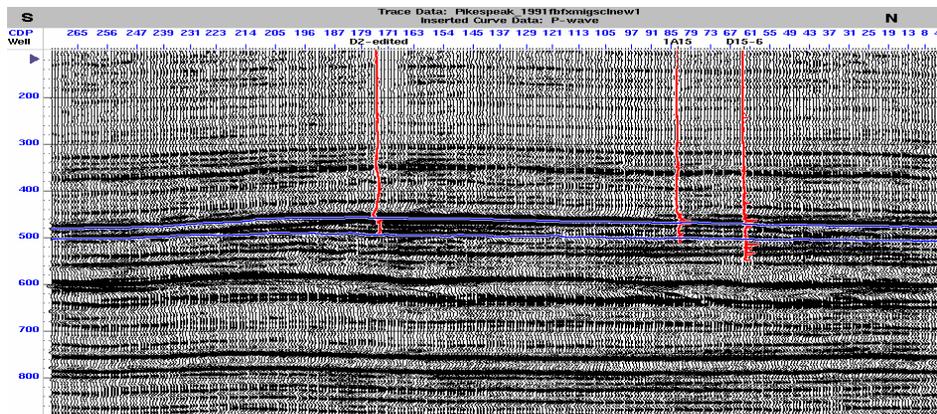
a.
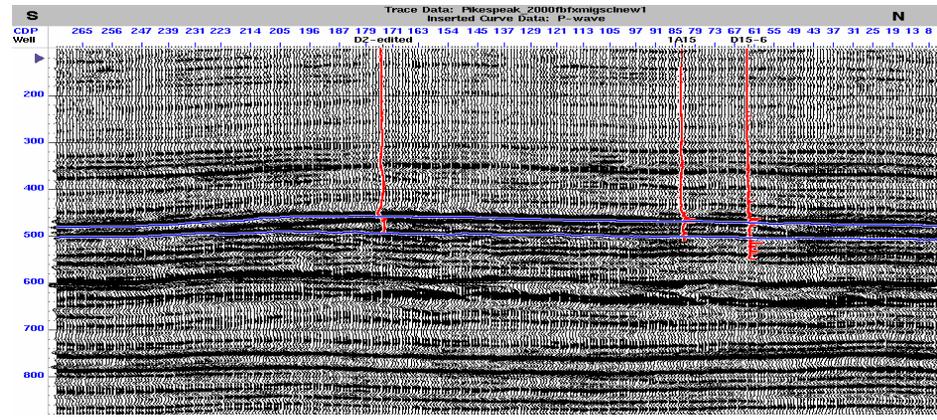
b.
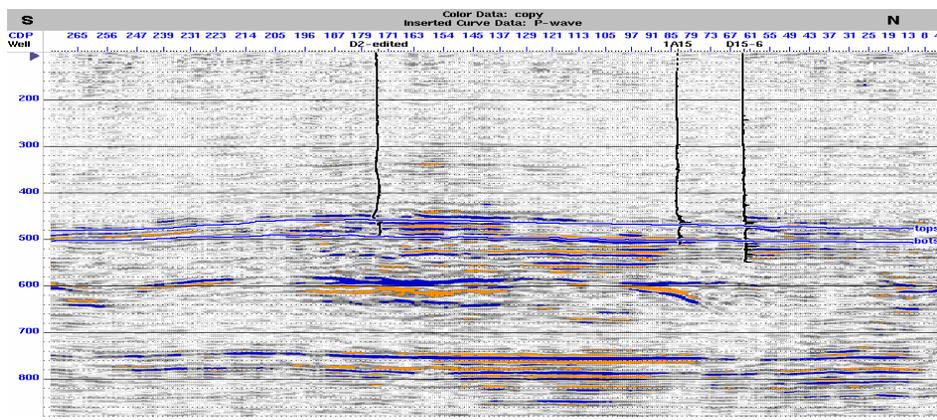
c.

Figure 3.5 Final migration stacks with surface consistent scaling for the 1991 survey (a.) and the 2000 survey (b.) and their difference (c), relative scale: orange is +1 and blue is –1.
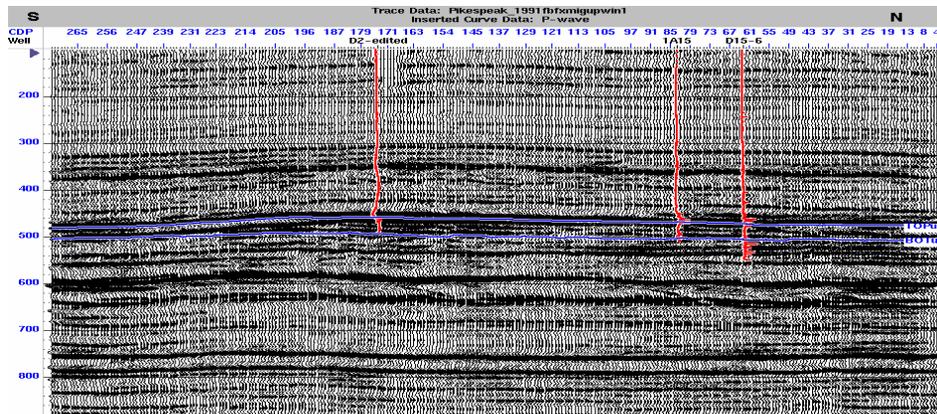
a.
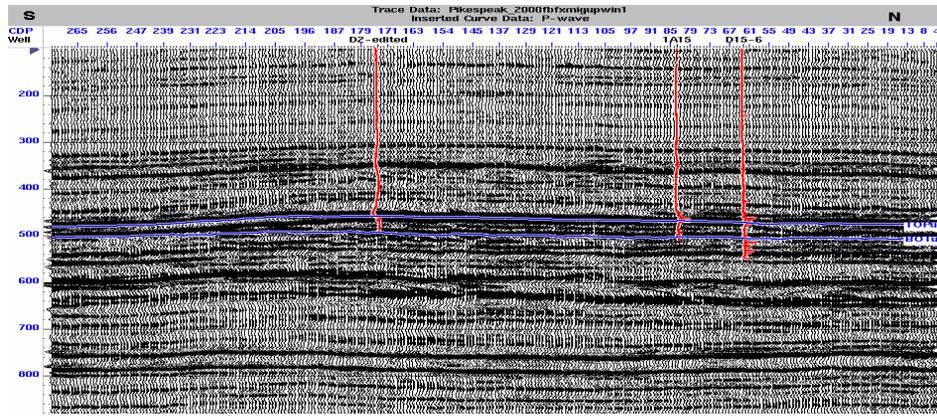
b.
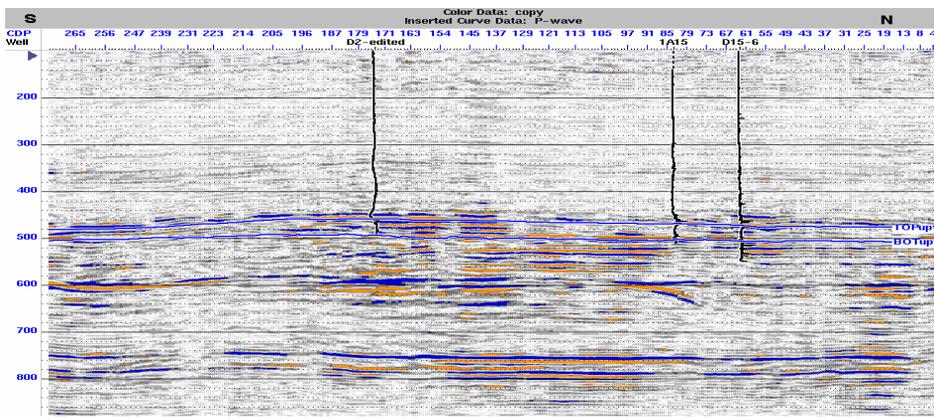
c.

Figure 3.6 Final migration stacks with two mean window scaling for the 1991 survey (a.) and the 2000 survey (b.) and their difference (c), relative scale: orange is +1 and blue is –1.

The following is a detailed discussion on the trace equalization used in this processing.
Trace equalization is always a tough issue in time-lapse seismic processing if the surveys
have different vintages. We have to apply scaling to enhance the amplitude in the zone of
interest, although scaling can damage relative amplitude if used without care. In the
above paragraphs, it was mentioned that three scaling methods had been tested in order to
obtain an optimized result. The scaling methods tested are:

1) Conventional scaling

One mean window from 450 ms to 1400 ms with multiple mean windows above is
applied. The reservoir is around 470 ms to 510 ms. The multiple windows at shallow
depths suppress high-amplitude ground roll and the mean window keeps the relative
amplitude around the reservoir.

2) Surface-consistent scaling

An one-window (250 ms to 450 ms) scalar is calculated on filtered data and then solved
into the receiver, shot, offset, and CDP component. Then the receiver, shot, and CDP
components were applied to unfiltered data. The relative amplitude between offsets is
preserved.

3) Scaling with two mean windows

One mean window across the reservoir from 450 ms to 1400 ms with another mean
window above the reservoir from 250 ms to 450 ms and multiple mean windows
approximately above the weathering marker were applied.

It was assumed the relative amplitude in the 250 ms to 450 ms time range does not
change systematically within the two surveys.

The final stacks of the above three scaling methods for both the 1991 and 2000 surveys and their difference are shown in Figures 3.4, 3.5, and 3.6.

3.4   Comparison with production activity

Comparing these three difference plots, we can see that most areas are similar but there is some difference between them. For conventional scaling, the northern end of the line (right hand side) has a relatively small difference compared to the southern end of the line. But for the other two scaling methods, both the northern end and southern end have considerable difference in energy. The steam injection caused velocity decrease in the 2000 survey within the reservoir, and therefore, the travel time through the steam zone is longer in the 2000 section. When subtraction is done, the difference energy inside the reservoir is due to both acoustic impedance change and time delay on the 2000 stack. The difference energy below the reservoir is mainly due to the time delay on the 2000 stack. On all the difference plots, the difference in the middle of the line is larger than either end. Obviously, there is a large difference below 750 ms between CDP 96 to 160.

To further discuss which of the difference plots is acceptable, we have to investigate the production activity and do some isochron analysis. From the Accumap system well activities in the study area were obtained. Three well logs were tied to the three final stacks to identify the reservoir top and bottom. Then the reservoir top and bottom for the six stacks were picked and the isochron ratios were calculated, that are the isochron of the 2000 survey divided by the one from the 1991 survey. Figures 3.7, 3.8, and 3.9 have the difference sections from the three scaling methods plotted with well activities and isochron ratios. The high frequency difference among the isochron ratios may be caused by the time delay induced by random noise and error.

Well activities are marked by year in groups. Production started from the southern part of

the line (left) in 1983. At the time when the 1991 survey was acquired, the production in

this part had been carried out for 8 years. The reservoir had already been heated up. The

average temperature in this region should be similar in 1991 and 2000. The rest of the

reservoir had not been heated in 1991. In 1995 and 1997, two groups of wells (circled on

Figures 3.7, 3.8, and 3.9) had been drilled and started for thermal recovery. A detailed

production activity will be present in Chapter 4. This corresponds to the large difference

energy on the difference stacks from all the three scaling methods very well between

CDP 96 to 160. In 2000, the production around well 1A15 had just begun for two months

prior to the seismic survey and the temperature should not have been high in this region

yet. Therefore, there should not be a large difference in this part of the line. Given all of

the above considerations, conventional scaling gives a reasonable result. Actually, the

difference sections from the conventional scaling and surface consistent scaling are very

close. Conventional scaling is better in the northern end but is less continuous on the

event at 600 ms in the middle of the section. The difference section with conventional

scaling was used in the following chapters, but please keep in mind that there are pros

and cons for different scaling methods.

Theoretically, surface-consistent scaling should be better than the other two scaling

methods but this is not true in some real cases. This problem has been noticed by Lumley

(2001). For the land seismic survey, uniform source and receiver coupling with the
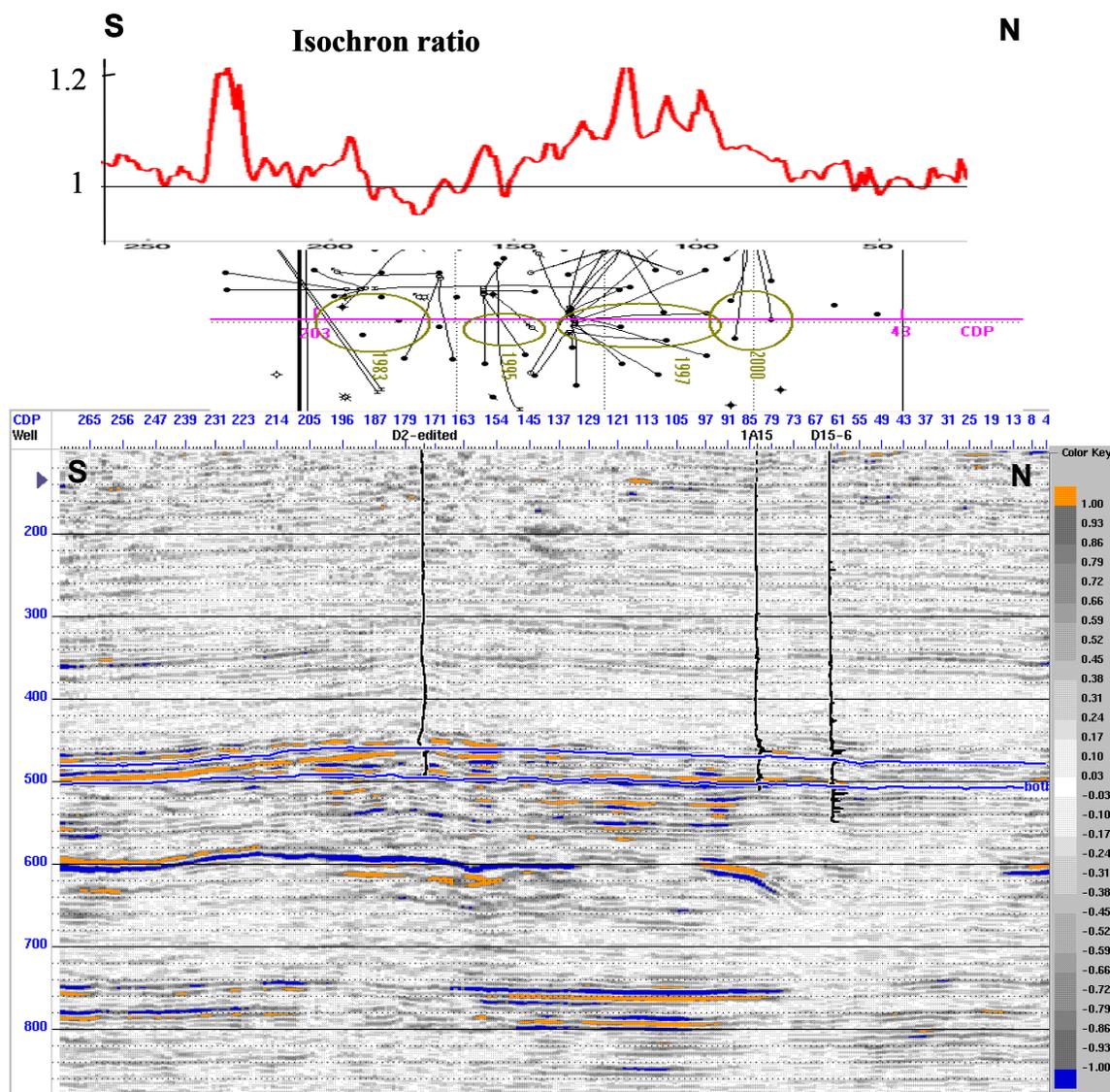
Figure 3.7 Difference section from conventional scaling (bottom, in relative scale from –1 to 1) with well activities (middle, circles mark the drilling time) and isochron ratio (top, which is the isochron of the 2000 survey divided by the one from the 1991 survey).

ground is difficult to obtain during the entire survey. Variable coupling can be detrimental for achieving true amplitude in a seismic survey. Another aspect is that the strong ground roll should be cleaned up before surface consistent decon and scaling. Since a good program was not found that can efficiently attenuate ground roll noise

without damaging the signal, there was no noise attenuation applied before surface

consistent decon and scaling.
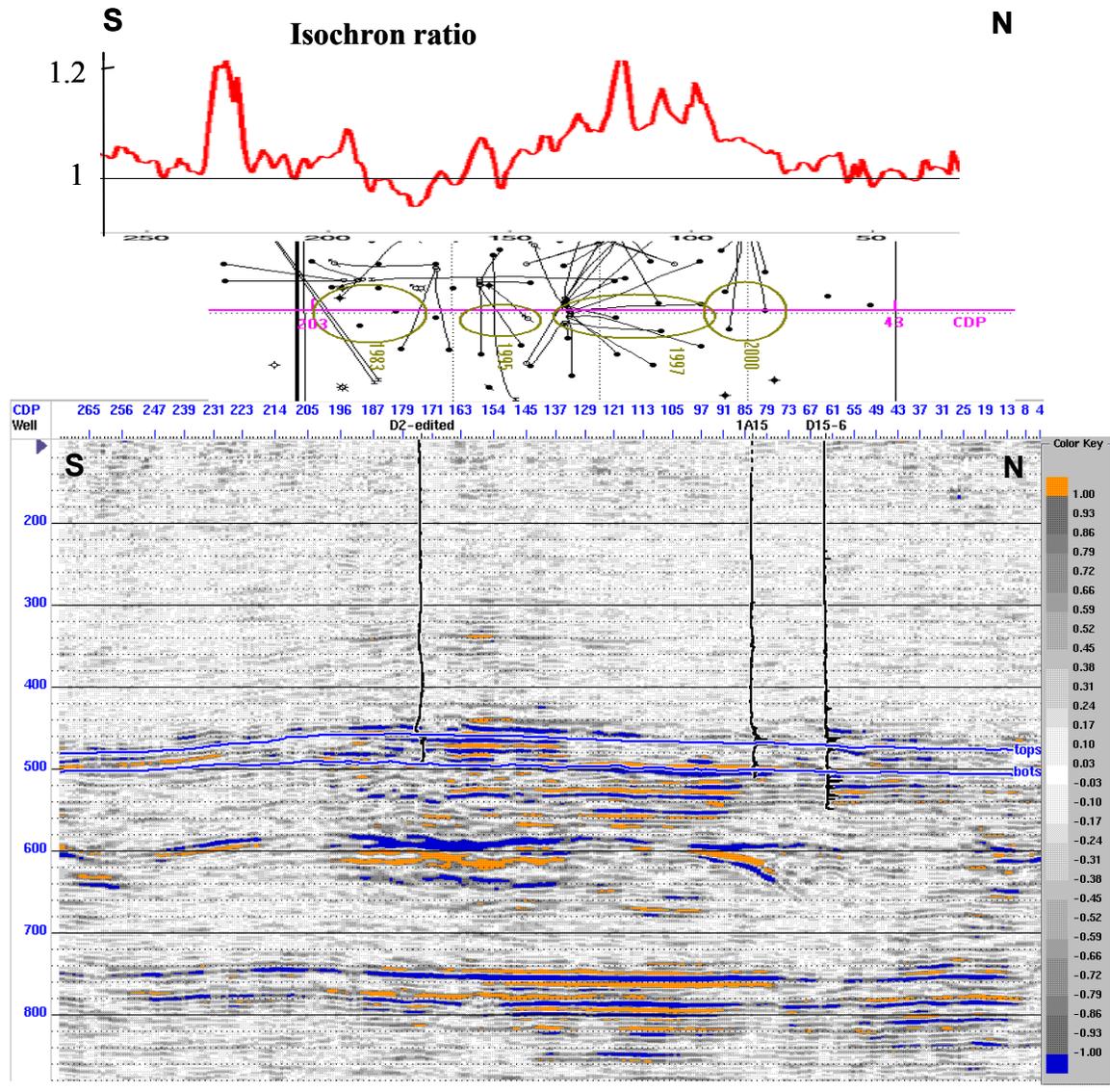
Figure 3.8. Difference from surface consistent scaling (bottom, in relative scale from –1 to 1) with well activities (middle, circles mark the drilling time) and isochron ratio (top, which is the isochron of the 2000 survey divided by the one from the 1991 survey).
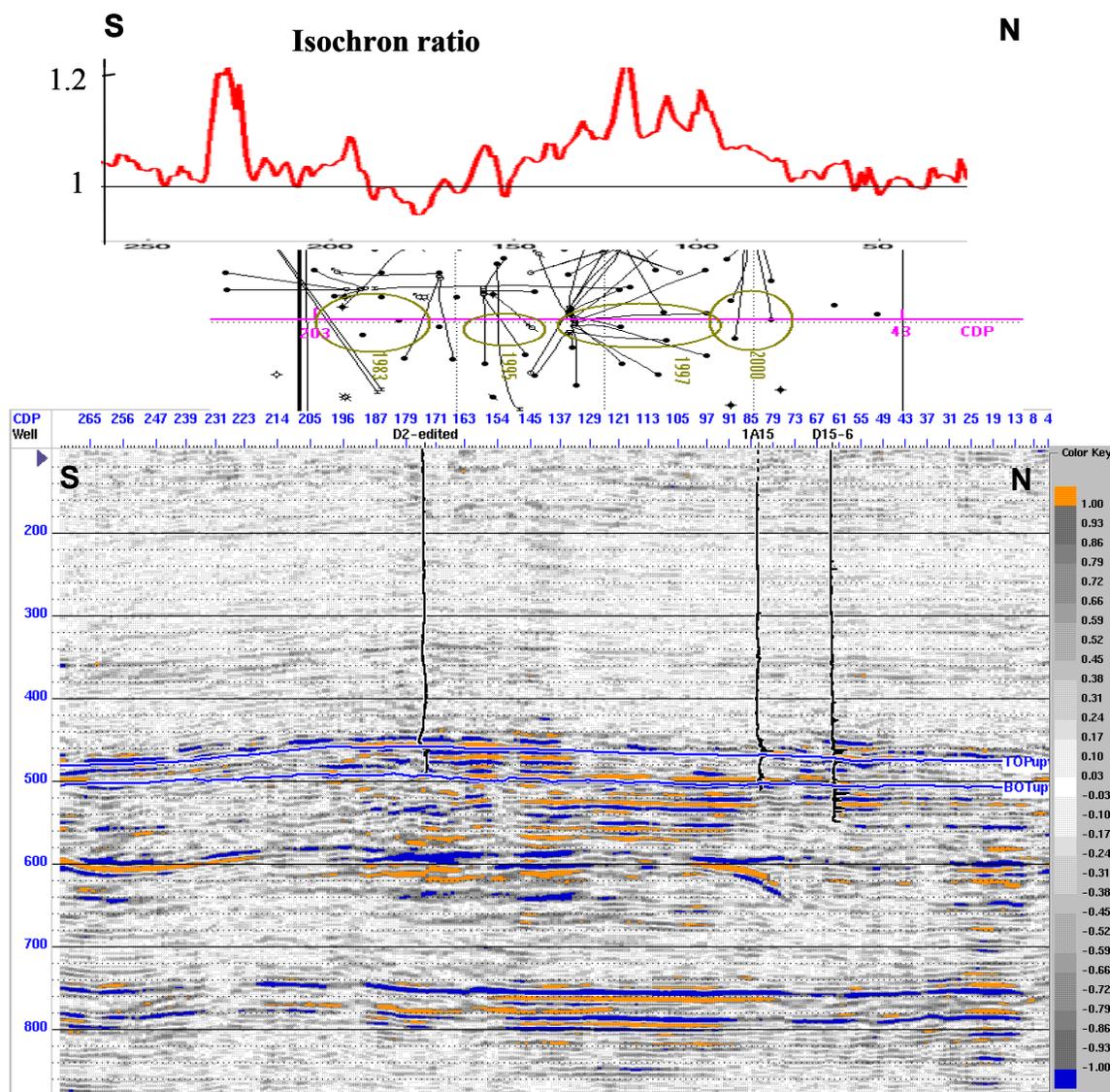
Figure. 3.9. Difference from two mean window scaling (bottom, in relative scale from –1 to 1) with well activities (middle, circles mark the drilling time) and isochron ratio (top, which is the isochron of the 2000 survey divided by the one from the 1991 survey).

With the large coherency noise the issue might be how to suppress the noise to gain a better image but not maintain it, especially within the matching window for cross-equalization. For these two time-lapse lines, ground-roll noise is quite large, and it is very strong on the 2000 survey. The conventional multiple-window scaling greatly enhanced

the signal-to-noise ratio above the reservoir. This probably helped in cross correlation between the two surveys.

3.5   Discussion

There are many published examples dealing with cross equalization among time-lapse seismic surveys (Johnston et al., 2000, Lumley, 2001, Rickett and Lumley, 2001). Not many examples can be found on amplitude scaling discussion for time-lapse seismic processing. In fact, scaling is an important step for getting a proper cross equalization. We might need to preserve the signal amplitude and suppress noise amplitude rather than preserve all acquired amplitudes.

To further discuss the location error on the final sections, the resolution of the seismic surveys should be considered. Since the velocity in reservoir depth is about 3000 m/s (from the well log) and the dominant frequency is 60 hz, the wavelength of the seismic signal is around 50 m. The lateral resolution of the migrated stack is a quarter of the wavelength, 12.5 m, at the reservoir depth. The 5 m CDP dislocation is far from the seismic resolution and therefore it is not necessary to do any correction.

Finally, in future investigations, it may prove useful to apply pre-stack time migration. Theoretically, pre-stack time migration should add clarity to the images compared to post-stack time migration. In real practice, the structure cannot be perfectly flat. The energy can be smeared by stacking before migration.

3.6 Conclusions

The presented processing flow has successfully gained wavelet and structure matched time-lapse seismic final sections. Three scaling methods were investigated for the two time-lapse seismic lines at the Pikes Peak heavy oil field. The processed difference sections were compared with isochron analysis and production activities. The large difference energy on the difference stacks from all the three scaling methods corresponds to well activities very well between CDP 96 to 160. However, conventional scaling methods with multiple mean windows above the reservoir and one mean window including the reservoir gave the result most consistent with production information. The cause for no ideal surface-consistent scaling could be due to strong ground roll and non-surface consistent amplitude. Time-lapse seismic processing should be set to preserve the signal amplitude and suppress noise amplitude rather than preserve all acquired amplitudes.

So far, we have discussed the rock physics procedure, the processing flow, and the processed final stacks. In order to compare the synthetic seismic sections with the processed seismic survey sections, we have to do reservoir simulation and then do seismic modeling using the seismic parameters converted from the output of reservoir simulation. The next chapter will take us to the reservoir engineering world to show how the reservoir simulation was done for this partial Pikes Peak Field.

Chapter Four: Reservoir simulation

4.1   Introduction

In Chapter 3, the seismic difference section was derived. The amplitude caused by time

delay in the centre of the reservoir and the amplitude in the southern end was observed on

the difference section. It cannot be seen by seismic analysis alone how these features are

associated with fluid-flow processes in the reservoir. By implementing a reservoir

simulation based on a reasonably simplified reservoir model, and then applying the rock

physics procedure in Chapter 2 to the output of the reservoir simulation, the engineering

parameters will be transformed to seismic velocities and densities. After performing

seismic modeling based on the derived velocity and density model, the seismic response

of reservoir process can be explained.

Reservoir simulation is a tool for engineers to predict future production rates from a

given reservoir engineering model with production history data. The theory is based on

conservation of mass and energy equations and the mass transport mechanism equations

(Darcy's law) in a porous media (Settari, 2001). For a general N component and L phase

model, the conservation of mass is (adopted from Settari and CMG's STARS User

Guide):

$$-\nabla \cdot (\sum_l \rho_l \omega_{li} V_l^c + \sum_l \rho_l \omega_{li} V_{li}^d) + A_{wi} + \sum_l \rho_l q_{kl} \omega_{li} + C_i$$
$$= \frac{\partial}{\partial t}(\phi \sum_l S_l \rho_l \omega_{li}), \qquad i = 1,...,N \qquad l = 1,...,L \tag{21}$$

ρ_l is the phase density; ω_{li} is the mass fraction of component i in phase l; S_l is the phase

saturation; A_{wi} is from thermal aquifer source/sink; q_{kl} is the well phase rate; C_i is the

chemical reaction contribution; V_l^c is the convection velocity; and finally V_l^d is the

dispersion velocity of phase l. The conservation of the energy equations is:

$$-\nabla \cdot (\sum_l \rho_l H_l V_l^c) + K\Delta T + \sum_l A_l + \sum_l \rho_l q_{kl} H_l + C + \sum_l L_l$$
$$= \frac{\partial}{\partial t}(\phi \sum_l S_l \rho_l U_l) \quad l=1,...,L$$
(22)

H_l is the specific enthalpy of phase l; K is the heat capacity of rock; A_l is the aquifer

contribution to the energy of phase l; C is the chemical reaction contribution to the

energy; the L_l is the heat loss term from adjacent formation; and U_l is internal energy per

unit mass of phase l. The mass transport mechanism equations are (Darcy's law and

Fick's law):

$$V_l^c = \frac{kk_{rl}}{\mu_l}(\nabla P_l - \gamma_l \nabla h), \quad \rho_l \omega_{li} V_{li}^d = -K_{li}\nabla(\rho_l \omega_{li}) \quad i=1,...,N \quad l=1,...,L \quad (23)$$

k_{rl} is the relative permeability; k is absolute permeability of the media; P_l is phase

pressure; h is depth; and K_{li} is the dispersibility of component i in phase l. Equations (21),

(22), and (23) are coupled with the auxiliary equations for saturations and capillary

pressures:

$$\sum_l S_l = 1, \quad P_{c,l+1,l} = P_{l+1} - P_l = f(S_1,...,S_l) \quad l=1,...,L \quad (24)$$

and the equations for phase equilibria:

$$\omega_{li}/\omega_{ki} = K_{lki} = f(P_l,T,\omega_1,...,\omega_N) \quad i=1,...,N \quad l=1,...,L \quad (25)$$

$\omega_1, ...,\omega_N$ are the total mass fractions of the multiphase mixture, and the auxiliary

equations for composition variables:

$$\sum \omega_{li} = 1, \quad l=1,...,L \quad (26)$$

The unknown variables are P_l, T, S_l, and ω_{li} (a total of 2L+NL+1 unknowns) and other

parameters are either obtained by field measurements or by laboratory test. The number

of conservation equations of mass (21) is N. There is only one conservation equation of

energy (22). The number of auxiliary equations for saturations and capillary pressures

(24) is L. N(L-1) is the number of equations for phase equilibrium (25). Finally, the

number of auxiliary equations for composition variables (26) is L. The total equation

numbers are 2L+NL+1. They are solved iteratively on a variable 3D reservoir mesh by a

finite difference algorithm (CMG's STARS User Guide).

A reservoir engineering model consists of the geometry of the reservoir, porosity

distribution, permeability curves, initial pressure, initial temperature, initial fluid

saturations, GOR (gas/oil ratio) curve, fluid viscosities, rock and fluid thermal properties,

etc. Maximum production rate and minimum reservoir pressure in an input file are

usually given to constrain the calculation iteration. The output of a reservoir simulation

usually consists of pressure, temperature, fluid saturation for every element, and fluid

production etc at specified time steps.

With an initial model and production history data from Husky, reservoir simulation was

undertaken for the partial reservoir that encompasses 230 meters on either side of the two

time-lapse seismic lines in the Pikes Peak heavy oil field. The simulator STARS (CMG's

STARS User Guide) was used courtesy of the Computer Modelling Group. The model

has four components: water, oil (dead), steam, and gas (methane) and three phases, water,

oil, and gas (vapour). At high temperatures, gas component can be in the vapour phase

and at high pressures gas component can be in the oil phase. Therefore, the gas phase

saturation could be composed of both steam and methane. The physical properties of the

steam were considered the same as the methane in the modeling. At the injection time, the high temperature may cause some solution gas to come out of solution and the low pressure in a production period may also cause gas to vaporize. The hydrocarbon gas and steam in vapour cannot be distinguished in the reservoir simulation results.

4.2 Reservoir model and production activities

Table 4.1 contains the basic reservoir properties. The relative permeability tables and other parameters for reservoir simulation were provided by Husky Oil. The initial reservoir model is 280 m wide in the east-west direction and 3000 m long in the north-south direction. After the preliminary reservoir simulation, it was found that the boundary effect could not be ignored because the large temperature change had reached to the east-west boundary. To avoid the boundary effect, 4 and 5 elements were padded in the east and west sides of the reservoir respectively. The padded reservoir grid geometry, well locations, and time-lapse seismic line location are shown in Figure 4.1. The final reservoir has a dimension of 460 m in the east-west direction and 3000 m in the north-south direction. The grid cells are 20 m by 20 m horizontally and are varying in thickness. The three layers correspond to the two interbeded top layers and the lower homogenous sand layer. Cyclic Steam stimulation (CSS) started in the southern part of the reservoir in 1983 at well 1D2-6. The average steam injection duration was 10 to 30 days followed by a few days of soak, and 5 to 10 months of production. The reservoir simulation is based on the injection and production history from Jan. 1981 to Aug 2003. Wells within 60 m of the seismic lines are summarized in Table 4.2. It takes about 36 hours to finish the running of the current model which has 10350 blocks.

Table 4.1 Pikes Peak Waseca Channel homogeneous unit reservoir properties

Depth	~500 m
Initial temperature	18 ^{o}C
Initial pressure	3350 KPa
Net pay (including lower interbeded zone)	5.7 – 27.5 m
Air permeability	4500-10,000 md
Porosity	0.34
Water saturation	0.08 – 0.22
Oil density	985kg/m^3
Dead oil viscosity	25,000 mPa.s
Oil formation volume factor	1.025 m^3/m^3
Initial GOR	14.5 m^3/m^3
Oil Saturation	0.86
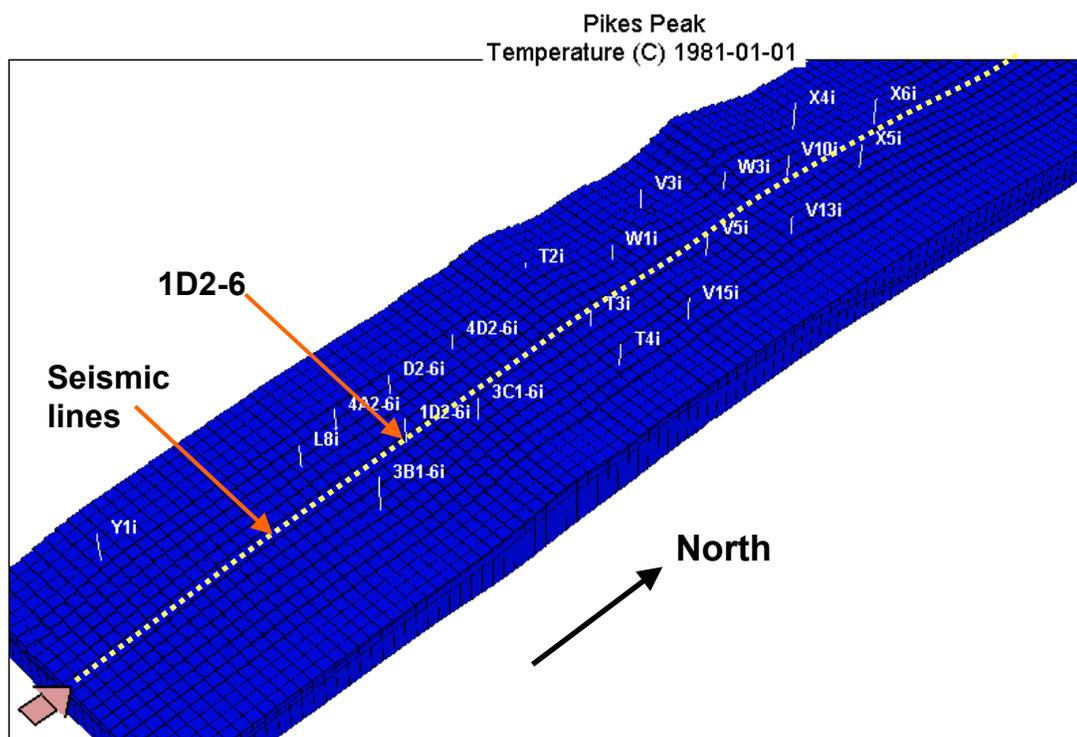
 Figure 4.1 Reservoir geometry, production wells, and time-lapse seismic line location.

4.3   Reservoir simulation results

The reservoir simulation is subject to the reservoir model introduced in section 4.2, the specified production rate, the bottom hole pressure constraint, and the numerical method. The resultant production and bottom hole pressure may not be close to the reality at the beginning. If we believe the theory and calculation methods are reasonable, we have to change the model to let the calculated simulation results match the field production and measured results. To compare the calculated results with field results and then to modify the model is called history match. For the current reservoir, the reservoir model was practically built by Husky Oil through their simulation runs. Only the absolute permeability values in lateral direction and convergence criteria were modified in the history matching process. It is impractical to analyse the history matching in this thesis for every well and therefore only one well will be discussed here. The history matching results for well 1D2-6 are shown in Figure 4.2 and 4.3. The history matching results for the other 6 wells that are within 60m of the seismic line are in appendix 1. These wells have more or less the similar results to well 1D2-6. For well 1D2-6, the cumulative liquid production from simulation is somewhat lower than the history data (Figure 4.2). However the cumulative oil production is about the same as the one from the history file. This means the cumulative water production is low. The simulated bottom hole pressure (BHP) dropped rapidly in early 1985 (Figure 4.3). Since the BHP reached the producer minimum pressure constraint of 202Kpa which is enforced within the model, the simulated water production stopped and caused the average liquid production rate to be low. BHP history file is unavailable and therefore it cannot be checked if the calculated BHP is close to the reality or not.

Table 4.2 Production history for the wells within 60 m of seismic lines

Well name [meters from seismic lines]	Brief history	Status in Feb. 1991	Status in March 2000
L8 (1A2-6) [~60 m]	CSS: 8/1985-10/1988, Prod.: 9/1992-1/193, Inj.: 2/1993-4/1993, Prod.: 4/1993-2/1997	Shut-in (since 10/1988)	Shut in (since 8/1997)
3B1-6 [~60 m]	CSS: 6/1984-9/1984, Inj.: 11/1990-1/1991, Prod.:1/1991-12/1991, Inj.:9/1992-11/1992, Prod.:11/1992-9/1993, Inj.: 9/1993-12/1993, Prod.:12/1993-10/1999, Inj.:10/1999-11/1999, Prod.: 12/1999-7/2003	Producing (since 1/1991)	Producing (since 12/1999)
1D2-6 [within 10 m]	CSS: 11/1983-12/1986, Inj.: 8/1992-9/1992, Prod.: 9/1992-7/1993, Prod.: 4/1994-9/1994, Prod.: 3/1995-12/1995, Prod.: 5/1996-10/1997, Inj.: 10/1997-1/1998, Prod.: 2/1998-7/2003	Shut-in (since 1/1987)	Producing (since 2/1998)
3C1-6 [~40 m]	CSS: 12/1983-5/1986, Inj.: 8/1992-9/1992, Prod.: 10/1992-7/2003	Shut-in (since 8/1986)	Producing (since 10/1992)
T3 (3B8-6) [~20 m]	Inj.: 8/1995-10/1995, Prod.: 10/1995-7/1997, Inj.: 7/1992-9/1997, Prod.: 9/1997-2/1998, Inj.: 2/1998-7/2000	Not drilled	Injection (since 2/1998)
W1 (4D7-6) [~60 m]	Inj.: 9/1999-10/1999, Prod.: 10/1999-2/2000, Inj.: 2/2000-1/2001, CSS: 1/2001-7/2003	Not drilled	Injecting (since 2/2000)
V5 (2B9-6) [~20 m]	Inj.: 11/1996-12/1996, CSS: 1/1997-8/1998, Prod.: 8/1998-3/2000, Inj.: 3/2000-4/2000, CSS: 3/2000-7/2003	Not drilled	Producing (since 8/1998)
W3 (4A10-6) [~60 m]	Inj.: 10/1999-10/1999, Prod..: 10/1999-1/2000, Inj.: 1/2000-2/2000, CSS: 2/2000-7/2003	Not drilled	Producing (since 2/2000)
V10 (1D10-6) [~20 m]	Inj.: 5/1997-6/1997, Prod.: 7/1997-3/1998, Inj.: 4/1998-5/1998, Prod.: 5/1998-2/1999, Inj.: 2/1999-3/1999, Prod.: 3/1999-4/2000, CSS: 4/2000-7/2003	Not drilled	Producing (since 3/1999)
X5 (3C9-6) [~40 m]	CSS: 8/2000-7/2003	Not drilled	Not drilled
X6 (1A15-6) [~20 m]	CSS: 8/2000-7/2003	Not drilled	Not drilled
	Inj.: Injection Prod.: Production		
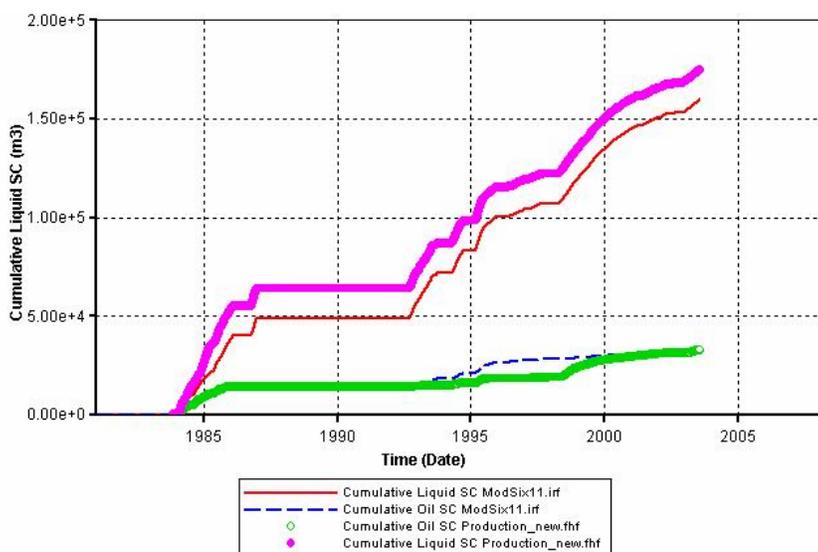
Figure. 4.2 History matching results of the cumulative liquid and cumulative oil production for well 1D2-6 in standard condition. The pink dots are the cumulative liquid productions from the history file. The red line is the cumulative liquid production from the simulation output. The green dots are the cumulative oil production from the history file. The blue dash line is the cumulative oil production from the simulation output.
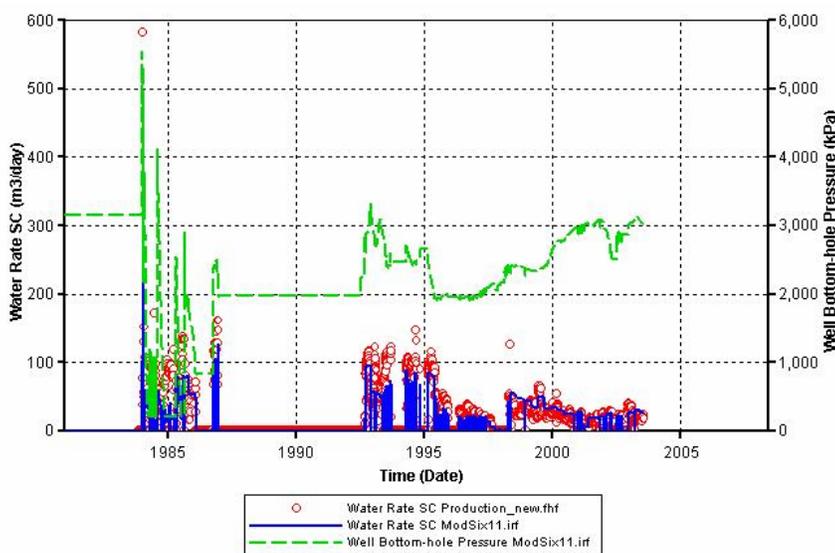
Figure 4.3 History matching results of the water rate and the bottom hole pressure for well 1D2-6. The red dots are the water rate in standard condition from the history file. The blue line is the water rate in standard condition from the simulation output. The green dash line is the well bottom-hole pressure from the simulation output (there is no pressure history).

The reservoir simulation outputs include the element values of reservoir pressure, temperature, water, oil, and gas saturations during the simulation history. Figure 4.4 shows the temperature distributions on the 3D volume at the starting time in 1981, the first seismic survey time in Feb. 1991, and the second survey time in March 2000. In 1991, the temperature changed around well 1D2-6. In year 2000, more production activities had started and the reservoir was heated around several wells. The temperature progress is about 5 to 8 m per year (average effect of production and injection). Pressure distributions on the three time steps are shown on Figure 4.5. Pressure changes had reached the boundary elements already by the 1991 time step. The pressure, temperature, oil, and gas saturation profiles will be plotted later with synthetic seismic sections in Chapter 6.

Gas saturation distributions on the three time steps are shown on Figure 4.6. The original reservoir had no gas cap. The heavy oil is live oil and has solution gas in it. During steam injection the reservoir temperature increased and pressure increased around the injection well. During production the temperature decreased and the pressured decreased too. Since pressure spreads rapidly, some locations not in the vicinity of the production well experience low pressure too. This can cause the solution gas to exsolve from liquid oil. Figure 4.7 schematically shows how the gas saturation and oil saturation vary with temperature and pressure. If an initial reservoir is injected with steam, it may move to point 1 state. Then it will be below the bubble point line and will have some gas vaporized out of solution even though the pressure is higher than before. During production, the new reservoir state may be at point 2, although temperature is not high it is still below the bubble point line due to the lower pressure. Please remember, in the

STARS simulator, steam and gas are treated the same as gas phase. All the gas saturation in the discussion after should be considered as the combination of steam and natural gas (methane).

4.4   Conclusions

The production history matching was reasonably good. The cumulative oil production for most wells matches the reported oil cumulative production in the history file. The cumulative water production is lower than the one reported in the history file and therefore the cumulative liquid production is a little lower than that from the history file. Pressure spreads much quicker (~20 m in one month) than temperature (~8 m in a year). Artificial boundary effects can degrade the simulation results. The boundary problem was minimized by adding boundary blocks on the east and west sides of the reservoir. Now, we have obtained reservoir engineering data during the production period from reservoir simulation. After applying the rock physics procedure to the output of the reservoir simulation, geophysical properties required for seismic modeling such as velocities and densities were derived. The next chapter will show how I used the derived velocities and densities to build models corresponding to the two seismic survey times, the procedure of the seismic modeling, and the comparison of the synthetic seismic sections to processed seismic survey sections.
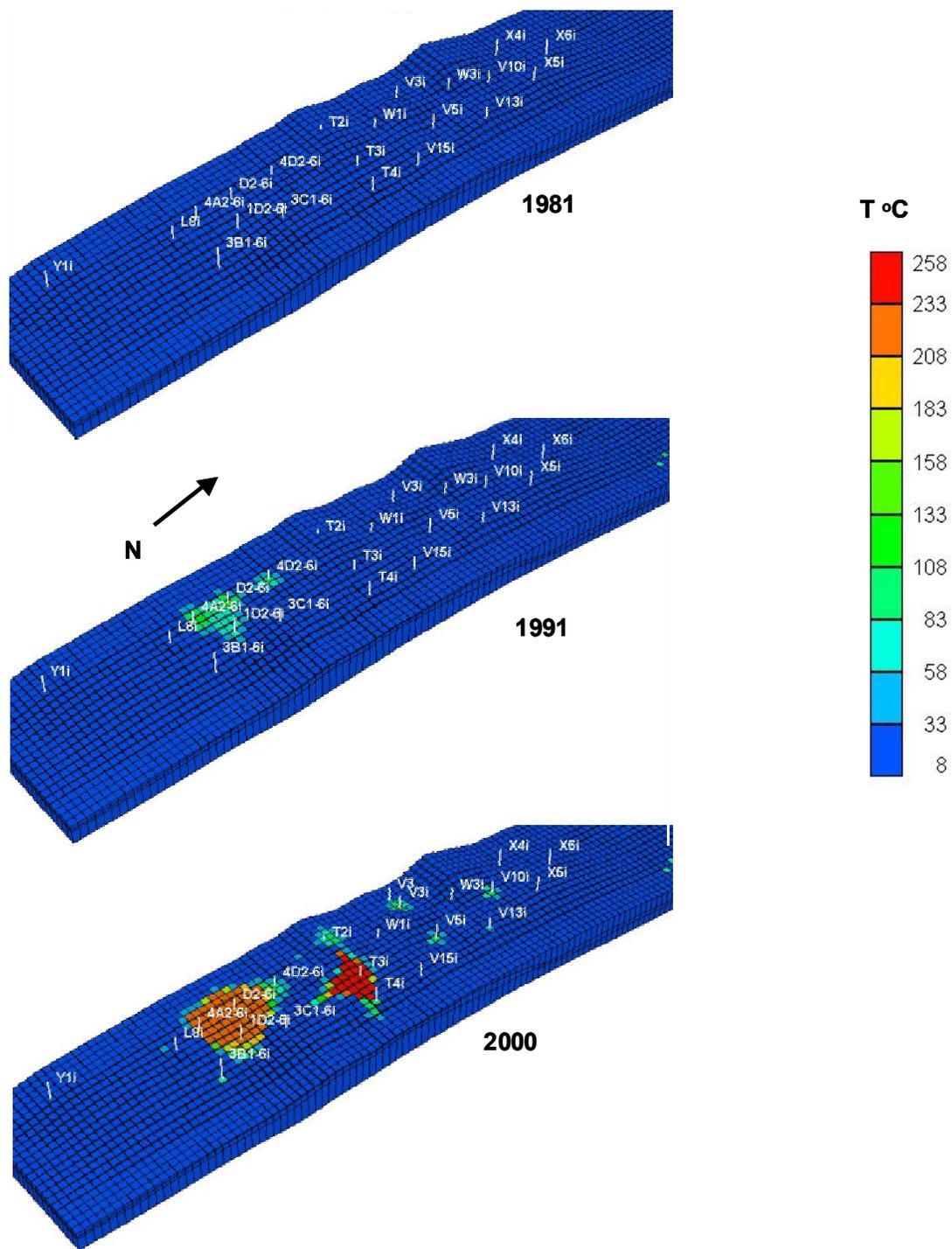
Figure 4.4 Temperature distributions from reservoir simulation at three dates.
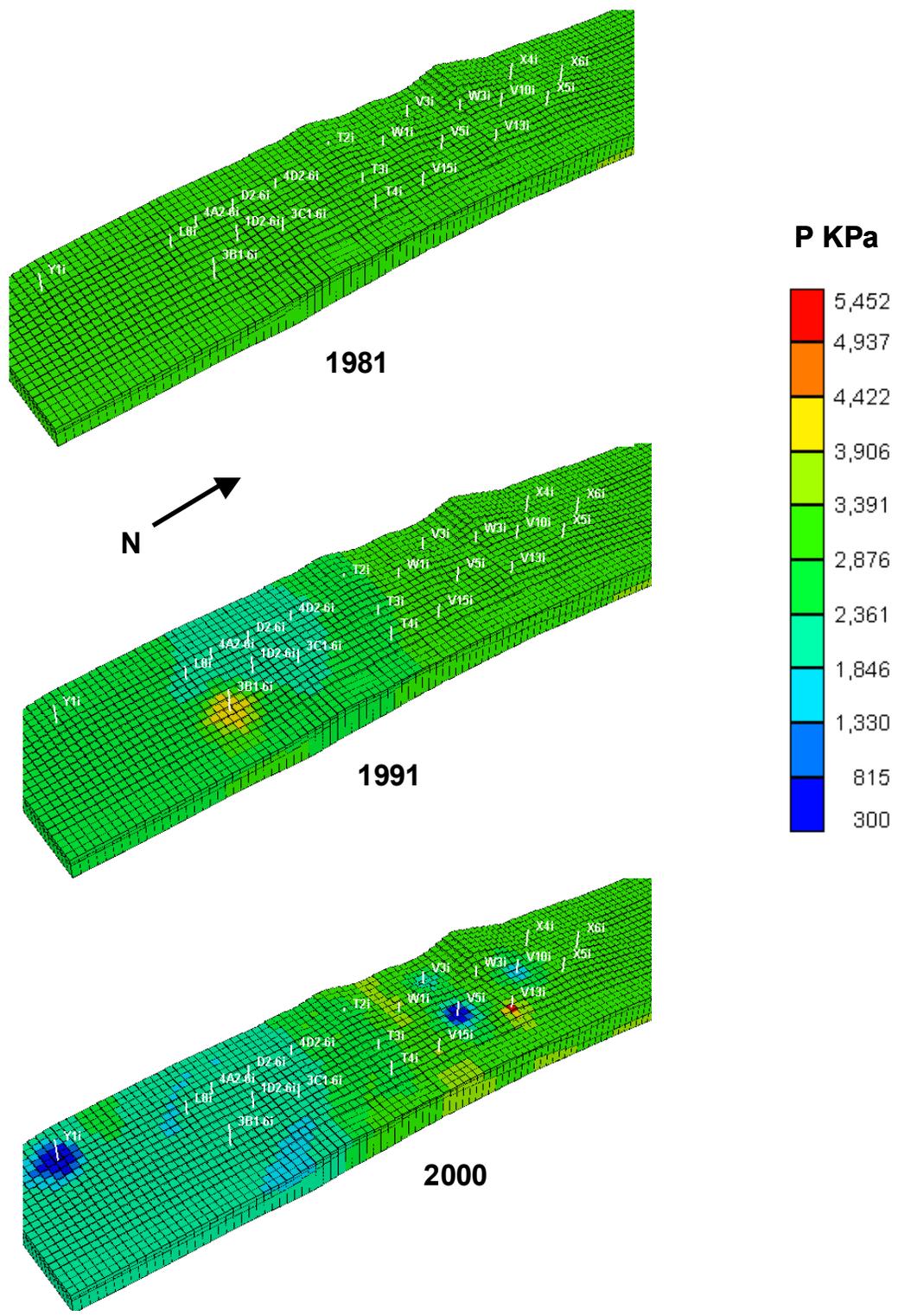
Figure 4.5 Pressure distributions from reservoir simulation at three dates.
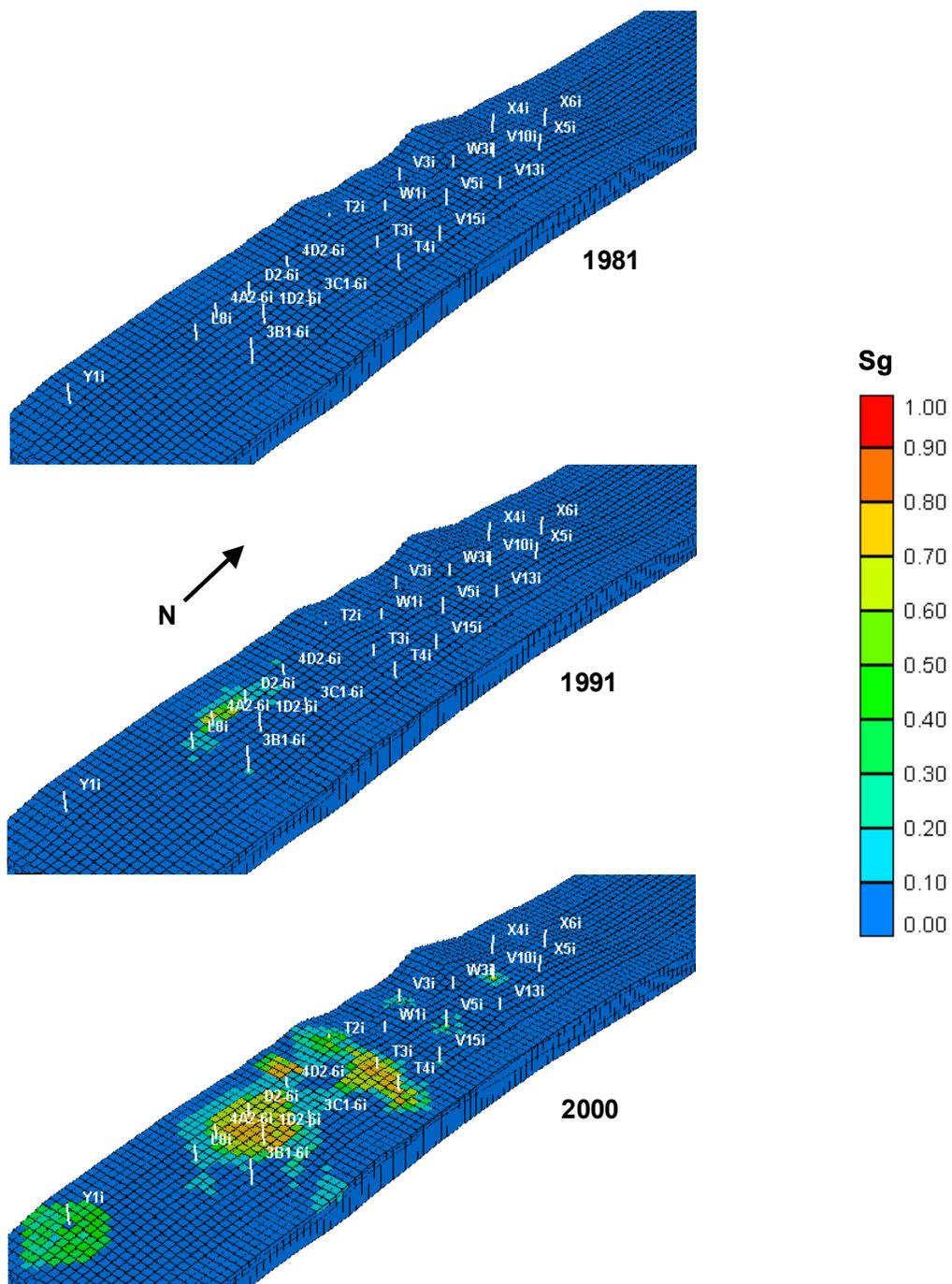
Figure 4.6 Gas saturation distributions from reservoir simulation at three dates.
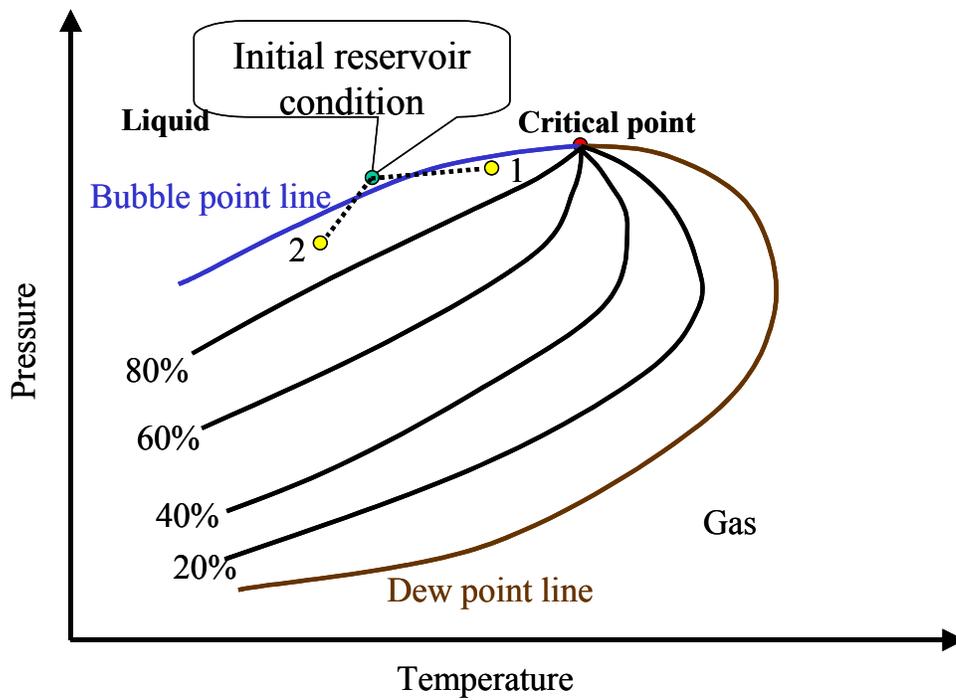
Figure 4.7 Hydrocarbon phase diagram in the pressure-temperature plane with contours of liquid oil saturation relative to gas.

Chapter Five: Time-lapse seismic modeling

5.1   Introduction

The reservoir simulation in Chapter 4 has given us a dynamic picture of the reservoir

change. To see the corresponding seismic response of the reservoir states at the two

seismic survey times, we need to do seismic forward modeling. The technique of forward

modeling in seismology is the numerical computation of theoretical or synthetic

seismograms for a given geophysical model of the subsurface. There are modeling

techniques based on the Kirchhoff integral, finite difference, and f-k domain solutions to

the wave equation (Yilmaz, 1991). For the current study, the calculated velocity and

density models are 2D matrices from the output grid values of reservoir simulation.

Promax processing software was used because it has the capability to import velocity and

density ASCII files. Promax offers the Finite Difference modeling of the P

(compressional wave) wave.

There are several published cases in time-lapse study that have combined reservoir

simulation with seismic modeling (Najjar et al, 2003, Johnston et al, 2000, Lumley, 1995,

Eastwood et al, 1994, and Jenkins et al, 1997). Only Jenkins et al (1997) conducted point

source modeling. Point source modeling, which simulates the real field survey, includes

the offset effect in the stacked section. Zero offset modeling (or 1D modeling) is quicker

than point source modeling but it is not suitable for detailed comparison with seismic

survey results. Both zero offset seismic modeling and point source seismic modeling

were tried. The match between synthetic seismic and real seismic was greatly improved

by using point sources and shot gathers for the last modeling version.

Time-lapse seismic modeling is the same as normal seismic modeling in principle.
However we should use the same parameters for the modeling corresponding to the two
seismic survey times that are Feb. 1991 and March 2000 in this case. The two models
have the same values outside the reservoir zone and the values inside the reservoir zone
can be different. The next section gives detail for the model building procedure.
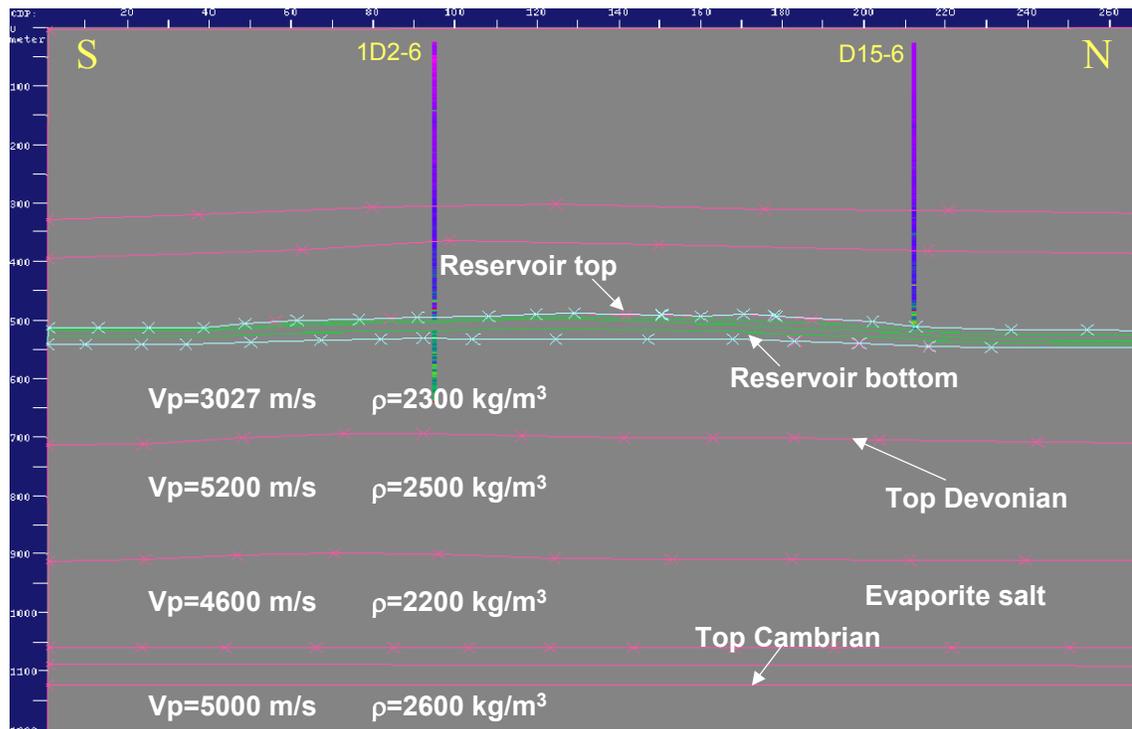
Figure 5.1 Synthetic seismic model. Above the reservoir velocity and density was interpolated along the structure using well logs at well 1D2-6 and well D15-6, inside reservoir the values were calculated using the output of reservoir simulation and the rock physics procedure, and below the reservoir are average values of well logs from adjacent wells.

5.2   Model building

5.2.1   Grid size match between seismic model and reservoir model

The reservoir model grid is 20 m X 20 m horizontally (section 4.2). That means after

applying the rock physics equation, velocity and density values were distributed every 20

meters along the profile corresponding to the seismic location. The processed seismic

survey sections have CDP intervals of 10 meters. Since the seismic model (velocity and

density model) is in CDP horizontally and in meters vertically, one point was interpolated

between two grid points of the reservoir output in order to match the synthetic seismic

CDP interval to seismic survey CDP interval. The interpolated grid points are CDP

numbers for the seismic model. The three vertical layers in the reservoir model give us

three values vertically at variable intervals (~1 meter to ~15 meters) (section 4.2). Since

the seismic vertical sample rate is 2 ms (millisecond), which is about 5 to 6 meters at

reservoir depth, the built-in interpolation function in Promax was used to output the

seismic models in the vertical interval of 2 meters. Therefore, the seismic models have 10

meter horizontal grids and 2 meter vertical grids.

5.2.2   Velocity and density model building

In the seismic model, the part above the reservoir was created using pre-production logs

from two wells, D15-6 and 1D2-6 (Figure 5.1) that were logged in 1978 and 1981. First,

major horizons that are the reflections of major formations were drawn based on a post-

stack depth migration section of the 1991 seismic survey. Then, the velocity and density

values were interpolated along the horizons. Inside the reservoir are the calculated

velocities and densities derived from the reservoir simulation output corresponding to the

Feb 1991 and March 2000 time steps, respectively. The pressure, temperature, fluid

saturation from reservoir simulation outputs plus oil and gas gravities, water salinity, K_s (rock grain bulk modulus), K_d (dry rock bulk modulus), μ (shear modulus), and porosity were inputs for the calculation of the velocity and density distributions using the rock physics procedure described in Chapter 2. The initial K_d and μ for the reservoir layers are 2.9 GPa and 4.9 GPa respectively. The calculation was only applied along the profile where the seismic lines are located. Since we do not have well logs deeper than the Devonian depth in the Pikes Peak area, we borrowed average velocity and density values from well 10-09 which is about 8 km west of the Pikes Peak area. The reservoir depth is around 500 m. To ensure the synthetic seismic sections have minimum boundary effect, the models were set to 1200 m deep and they include all the major stratigraphic markers (Figure 5.1).

5.3   Synthetic seismograms

To simulate the seismic surveys, we should have seismic sources and receivers and the similar geometry to the real seismic surveys. The source for the modeling is a 60 Hz zero phase Ricker wavelet. Figure 5.2 shows a modelled shot gather. The average velocity at 1991 time step in the reservoir interval is 2900 m/s. The seismic resolution is around $\lambda/4=V/4f=2900/(4 \times 60)=12$ m. The grid size of the seismic models is 2 m in depth and 10 m horizontally (CDP interval) and they are small enough to ensure the seismic resolution. There are 96 traces in a shot gather and the shot interval equals two receiver's distance. This gives 28 fold for a CDP gather which is very close to the 30 fold of 1991 seismic survey. The modelled time length is 1800 ms which is large enough to ensure that far offset energy was imaged. NMO (Normal Move Out) stack and post stack Finite Difference Migration were performed after the shot gather generation, which was also

designed to match the processing for the seismic surveys. The velocities for NMO and migration are converted from the model velocities. The migrated synthetic seismic sections for the 1991 time step and 2000 time step are displayed in Figures 5.3 and 5.4. From Figures 5.3 and 5.4, we can see that the geological boundaries were imaged very well. The multiples can be seen on the bottom of the sections, but they are not strong enough to damage the primaries. The high amplitude zones inside the reservoir have different features on the two sections. This amplitude change should be the effect of steam injection and production. Figures 5.5 and 5.6 are enlarged processed seismic survey stacks from Chapter 3 for the 1991 survey and 2000 survey. To compare the characteristic of the modeled synthetic seismic sections with the processed seismic sections, Figures 5.7 and 5.8 have the well locations marked and the reservoir zoomed in. The production induced amplitude change pattern can be seen in the lower part of the reservoir very similar to the processed seismic survey section in Figures 5.3 and 5.4. Please note that the shape and the phase of the events are not exactly the same between modeled and real seismic sections, because it is very difficult to get an earth model that are the same as the real earth. The reservoir simulation is mainly to observe the change of the reservoir, therefore, it is more practical to look at the difference sections of the modeled seismic and the field seismic. The synthetic difference section was generated by subtracting the 1991 final synthetic section from the 2000 final synthetic section (Figure 5.9); and the seismic survey difference section was generated by subtracting the 1991 final processed section from the 2000 final processed section (Figure 5.10). The CDP number 96 on the synthetic seismic section corresponds to CDP number 178 on the real seismic section and the direction of numbering is different on the two sections. The

difference sections from the synthetic modelling and seismic survey are going to be interpreted in the next Chapter.

5.4 Discussion

The current modeling algorithm is based on the scalar (acoustic) wave equation. The AVO effect cannot be modeled. Future work should extend the modelling to an algorithm based on the elastic wave equation that would be suitable for amplitude analysis.
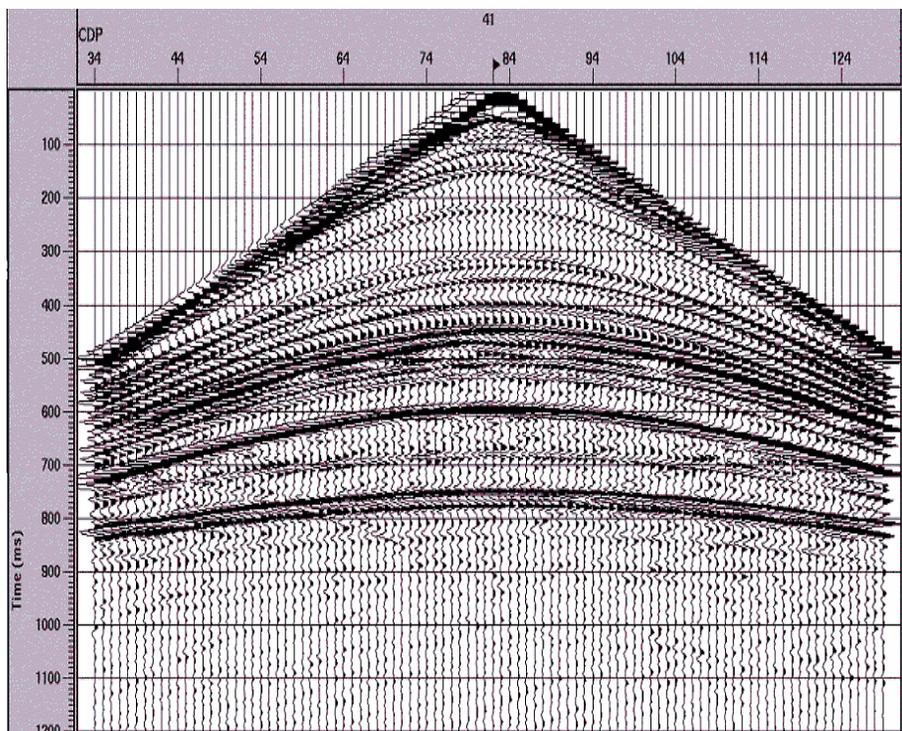
Figure 5.2 A synthetic shot gather.

5.5   Conclusions

This chapter demonstrated the seismic model grid building, the interpolation of the velocity and density values, the synthetic survey simulation, and the resulted synthetic seismic section. The seismic model grid is based on the interpolated reservoir grid to accommodate seismic survey geometry. The model values above the reservoir were interpolated from well logs. The model values inside the reservoir were calculated from the output of the reservoir simulation using the rock physics procedure introduced in Chapter 2. Finally, the model values below the reservoir were average values of the rock column from adjacent well logs. The modelled synthetic sections have very similar features when compared with the processed seismic survey sections. The synthetic seismic section at one time cannot be exactly the same as the seismic survey at that time due to the limitation of the initial earth model. It is more important to analyse the change in the seismic amplitude and traveltime that was caused by production activity than the absolute values of each seismic section. In the next chapter, the integrated interpretation will be given by comparing the real seismic difference section to the synthetic seismic difference section with the reservoir simulation results and other geophysical methods.
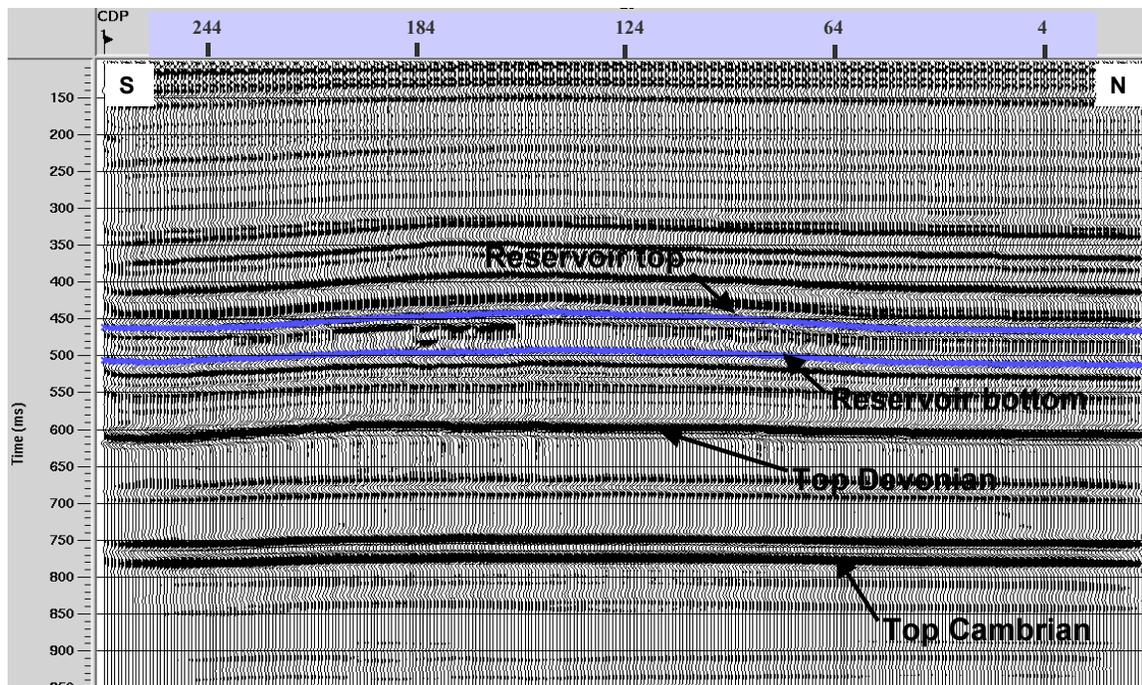
Figure 5.3 Migrated synthetic section for 1991 time step.
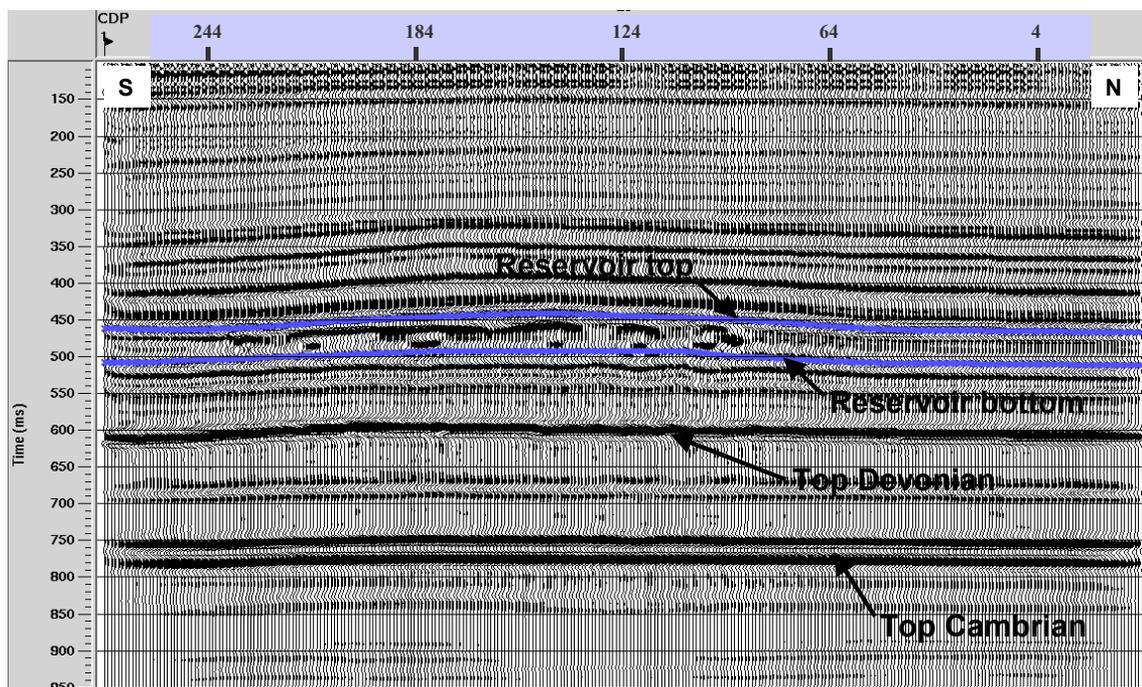
Figure 5.4 Migrated synthetic section for 2000 time step.
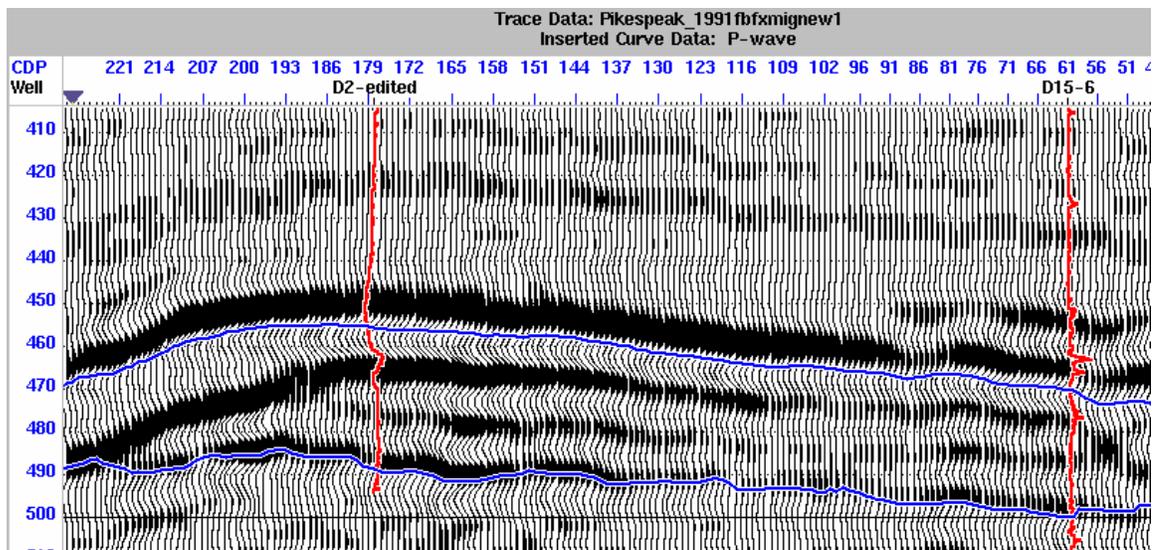
Figure 5.5 Enlarged final migrated stack of the 1991 survey
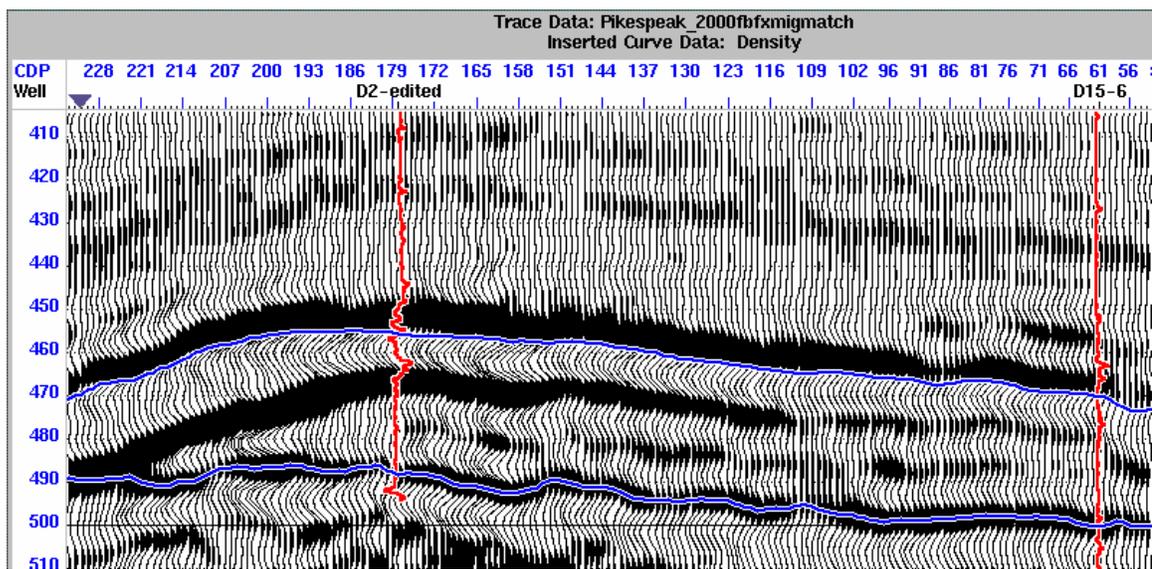
Figure 5.6 Enlarged final migrated stack of the 2000 survey
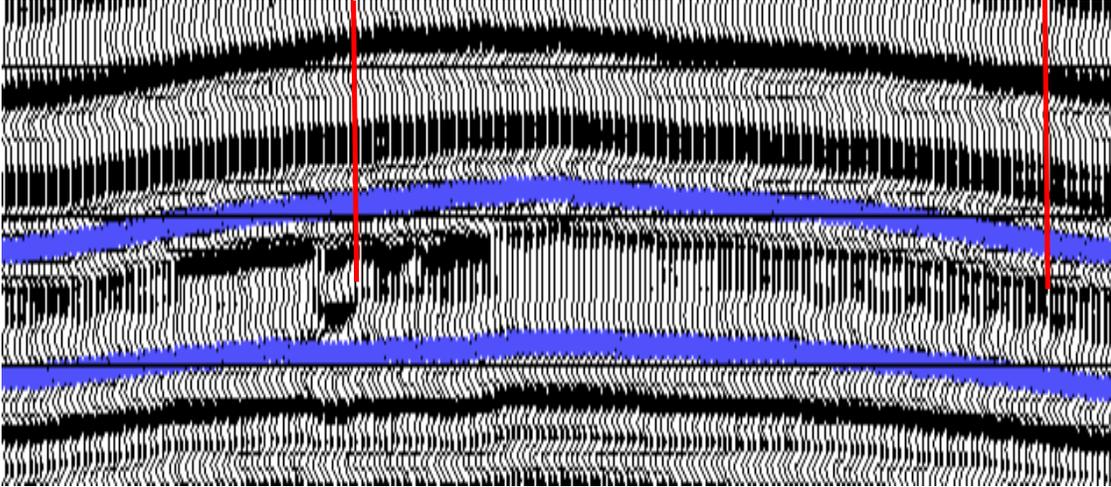
Figure 5.7 Enlarged final migrated stack of the 1991 synthetic seismic section
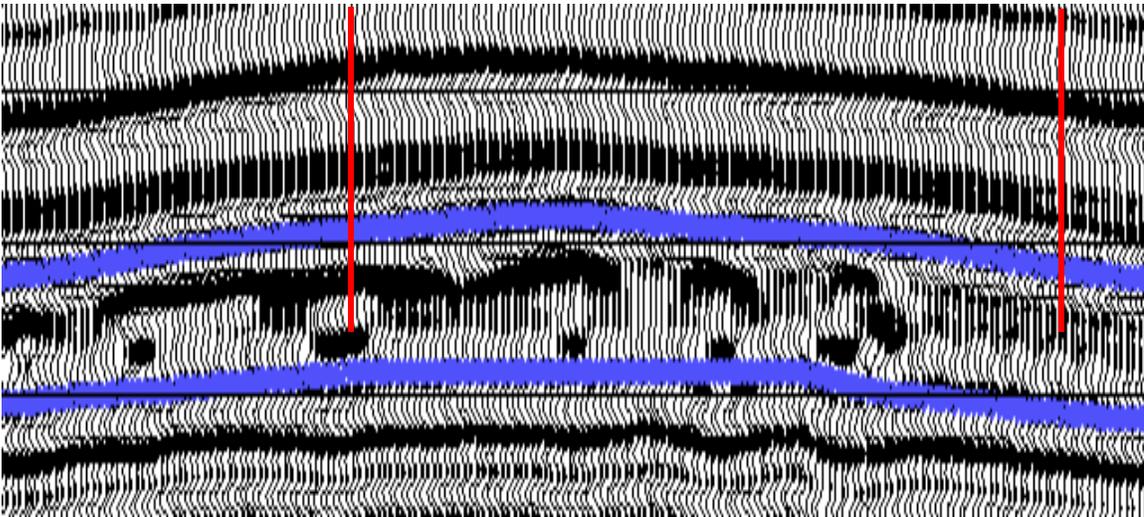
Figure 5.8 Enlarged final migrated stack of the 2000 synthetic seismic section
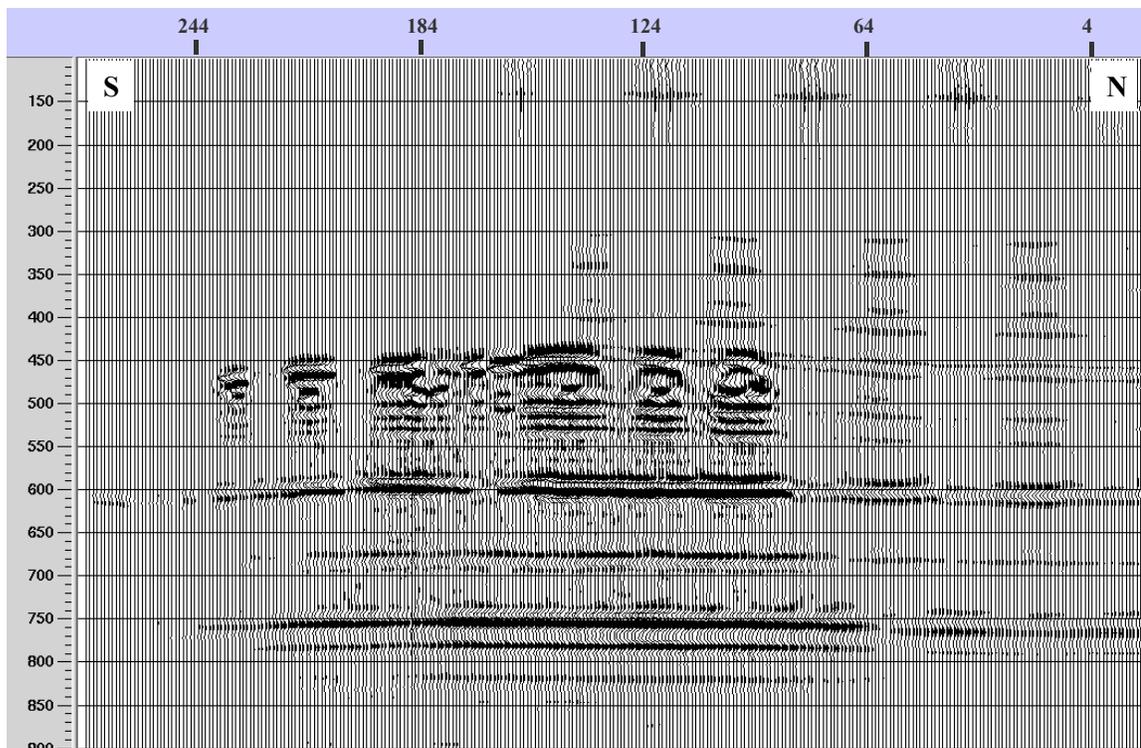
Figure 5.9 The synthetic seismic difference section, the 2000 synthetic section minus the 1991 synthetic section.
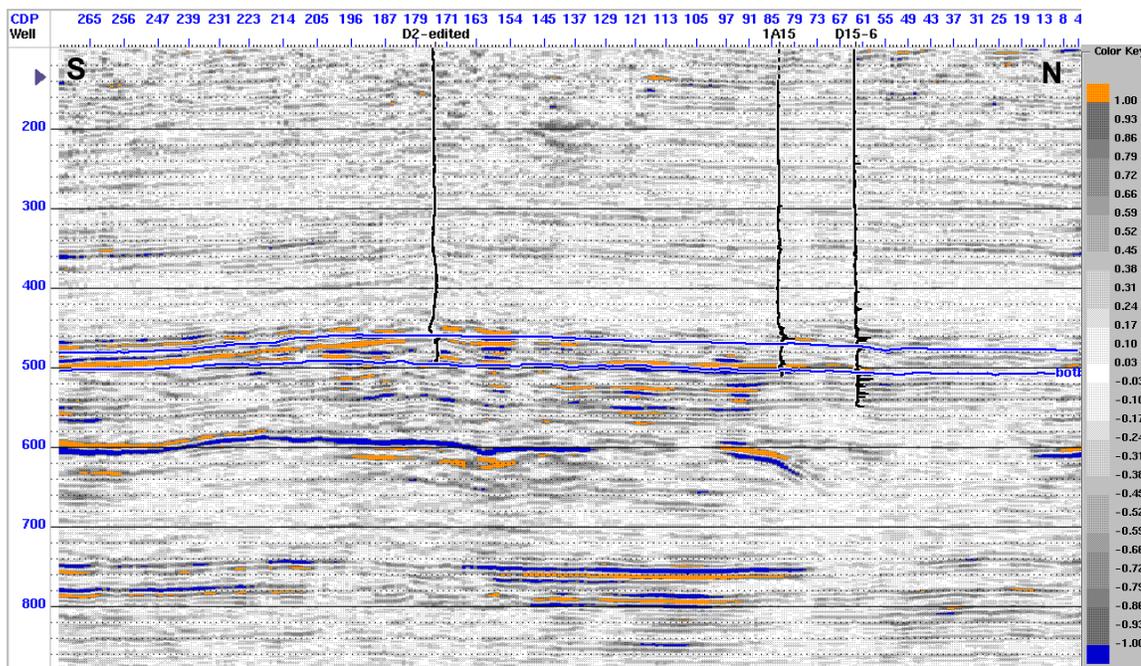
Figure 5.10 The seismic survey difference section, the 2000 final processed section minus the 1991 final processed section.

Chapter Six: Time-lapse interpretation of integrated data

6.1   Introduction

The ultimate goal of doing time-lapse reservoir analysis is to answer the practical

questions: where is the steam front or temperature front and where is the bypassed oil?

From Chapter 4 we have seen that reservoir simulation is constrained by the production,

temperature, and pressure data collected in the vicinity of wells, but the values of

pressure, temperature, and fluid saturations between or beyond wells are poorly

constrained with only the production data. Seismic surveys can be used to verify reservoir

information between or beyond wells. Before we start the interpretation of the seismic

difference section we have to know the limitations of seismic sections. In Chapter 3, we

have seen that processed seismic sections may have errors due to acquisition problems

and processing methods. By combining the synthetic seismic difference section, the real

seismic survey difference section, and the outputs of reservoir simulation (reservoir

pressure, gas and oil saturations, and temperature), the common existing features can be

extracted in the interpretation. In this way, the possible reasons for the mismatch and the

possible errors on seismic sections can be evaluated. Then, the above practical questions

can be answered based on the interpretation results.

6.2   Comparison between synthetic seismic and real seismic difference sections

6.2.1   Amplitude difference analysis

Figure 6.1 plots the difference sections between the 2000 stack and the 1991 stack from

the field seismic surveys (up) and the synthetic seismic modeling (down) and they are

matched together by well positions. The marked wells on the upper plot are all the wells

that are within 60 m of the seismic line. According to the production history (Table 4.1)

W wells started operation in September 1999 and X wells had not started operation until

August 2000. From the results in Chapter 4, it is known that the temperature spreads

about 5 m to 8 m per year and the W wells are at a 60 m offset from the seismic lines.

Therefore, temperatures from W wells should not have impacted on the 2000 seismic

survey. It is also known that pressure spreads about 20 m per month. The W wells were

just switched from production to injection in Feb. 2000. Therefore, the low pressure due

to production should not have had a large impact at the location of the seismic lines.

Based on the above consideration, on the lower plot of Figure 6.1, only the wells that

started in operation before 1999 are marked. We can see the banding effects on both

sections are mostly around these wells. The strong continuous event around the Top

Devonian on the synthetic difference section is missing in part of the real data indicating

that the seismic survey difference section using the conventional scaling method may

have some error in this part of the line. On the difference section from the surface

consistent scaling (Figure 3.4) this event is continuous below the reservoir. The

difference energy on the top reservoir at the southern end (left hand) of the line is on both

difference sections, although there is no well activity. We will discuss the cause by

comparing the synthetic difference section with the pressure, temperature and gas

saturation profiles. The difference energy on the shallow part of the synthetic difference

section (~120 ms) and the lower part of the northern end of the synthetic difference

section (~600 ms and 750 ms) seems to be processing artifacts, because of the similar

difference energy that can be found on the real seismic survey difference section (~80

ms).
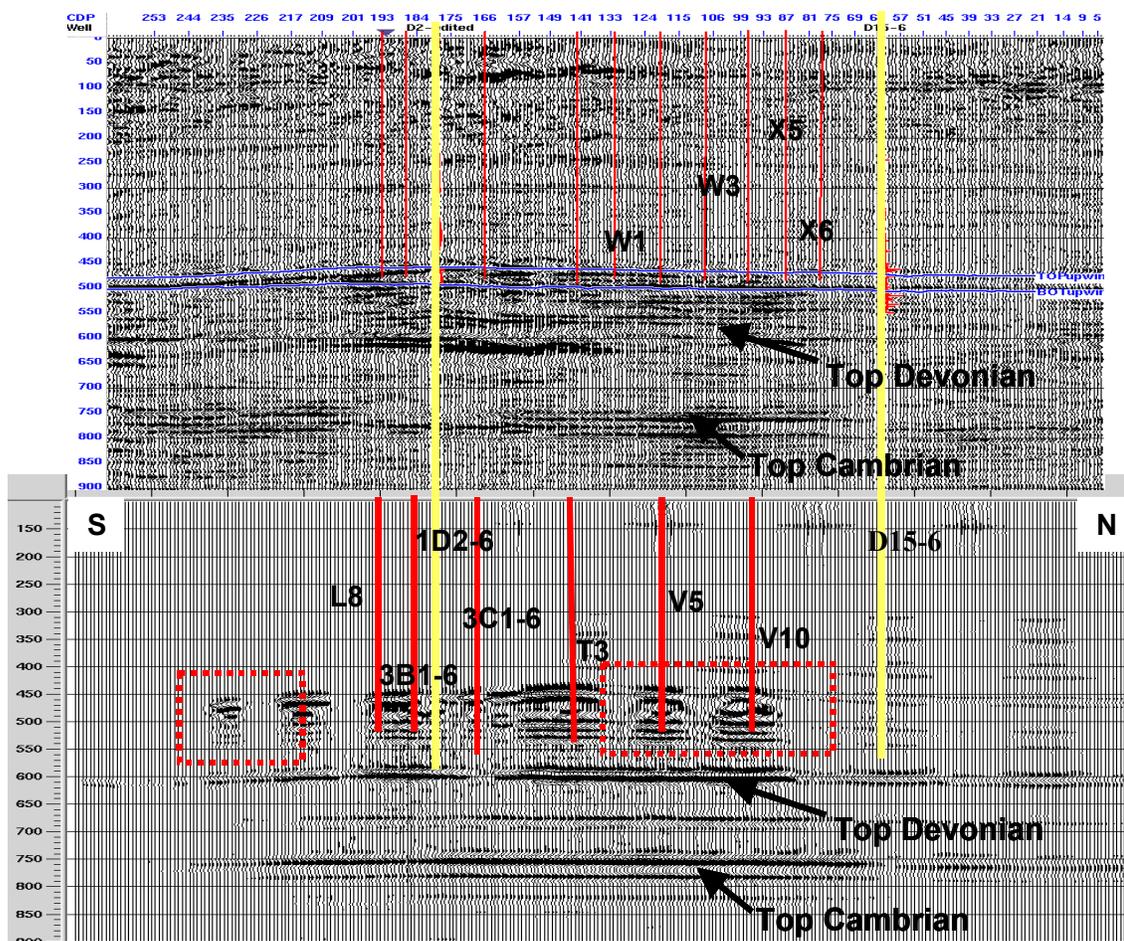
Figure 6.1 The difference sections between the 2000 stack and the 1991 stack from real seismic survey (up) and synthetic seismic modeling (down).

Both seismic survey and synthetic seismic processing have had post stack FDM migration applied to them. The amplitude change due to reservoir change may be migrated to the shallow part and the end part of the sections. Somehow these energies cannot be cancelled by the subtraction of the time-lapse sections.

The areas with dashed boxes are the areas that have large mismatches. On the synthetic seismic difference section it seems that there is less communication between well T3, V5 and V10 than on the real seismic survey difference section. The lateral permeability was increased in the reservoir model and the reservoir simulation was rerun. The resulting

seismic difference section had no visible change. One explanation is that the simulation model still has some other parameters that need to be checked. Alternatively, real seismic survey may have smeared the difference between these wells due to noise contamination and processing limitations. Post-stack migration was used and therefore, it might not produce the optimal image. Additionally, 3D effects may contaminate the 2D seismic survey data. Pre-stack migration may improve the match. These synthetic seismic modeling results are the closest match to actual seismic survey results that have been obtained to date.

6.2.2   Travel time difference analysis

Isochron ratio analysis was discussed in section 3.4. The isochron ratio for real seismic is the reservoir bottom horizon time minus the reservoir top horizon time of the 2000 seismic survey divided by the same value for the 1991 survey. The same analysis was also done on the synthetic seismic sections.

If there is no travel time change the isochron ratio should be very close to a value of 1 (Figure 6.2). This can be seen outside the reservoir zone in the northern part. The high values outside the reservoir zone in the southern part of Figure 6.2 appear on both the synthetic results and the real seismic results, although the positions are not matched exactly. There must be a reason for this and it will be discussed in section 6.2.3. The synthetic results show a maximum17% increase in travel time within the zone adjacent to wells T3 to V10. This is consistent with the real seismic results of an approximate increase of 20% increase in travel time. The ratio is back to a value of 1 between wells T3 and V5, and wells V5 and V10 in synthetic results. The results from the seismic survey do not show this.

Around wells 3B1-6, 1D2-6 and 3C1-6, the synthetic results show isochron values larger

than 1 but the real seismic results show isochron values smaller than 1. There are two

issues to consider. 1D2-6 and 3C1-6 were shut-in in 1991 (Table 4.2) after a period of

CSS production that started in the mid 1980s. Possibly, there was some residual

temperature and gas saturation around these well locations and therefore, the velocity was

relatively low during the 1991 survey. In 2000 these two wells were again in production

for more than two years (Table 4.2) so the temperature might be lower than in 1991. The

velocity around these same wells might be higher than those in 1991. Well 3B1-6 was in

production both in 1991 and 2000. Therefore, this mismatch is very likely due to a

reservoir simulation error. The temperature and gas saturations are high in the reservoir

simulation (Figure 6.5 and 6.6) around this area. Another aspect may be random error,

since the difference of the travel time around this part of the line between the two surveys

is about one sample interval (Figure 6.3). In Figure 6.3, the isochron difference between

wells 1D2-6 and 3C1-6 is around 2 ms which is the sample rate for seismic processing

and synthetic seismic modeling. The maximum time delay for both synthetic and real

seismic is around 7 ms and it is from CDP 130 to 180 in Figure 6.3. These CDP ranges

correspond to the large seismic amplitude below the reservoir on the difference sections

in Figure 6.1. This suggests that the large time delay caused the large mismatch below the

reservoir and the large difference amplitude on the seismic sections.
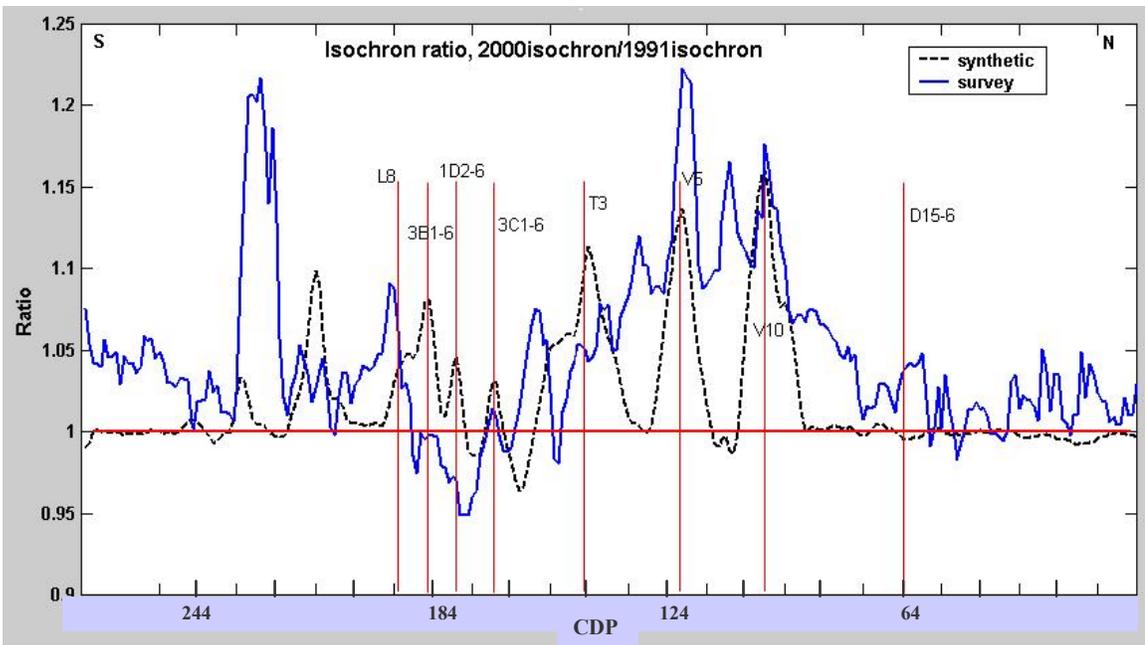
Figure 6.2 Isochron ratio comparison. The CDP numbers for the seismic survey sections were converted to the synthetic seismic CDP number for easy comparison.
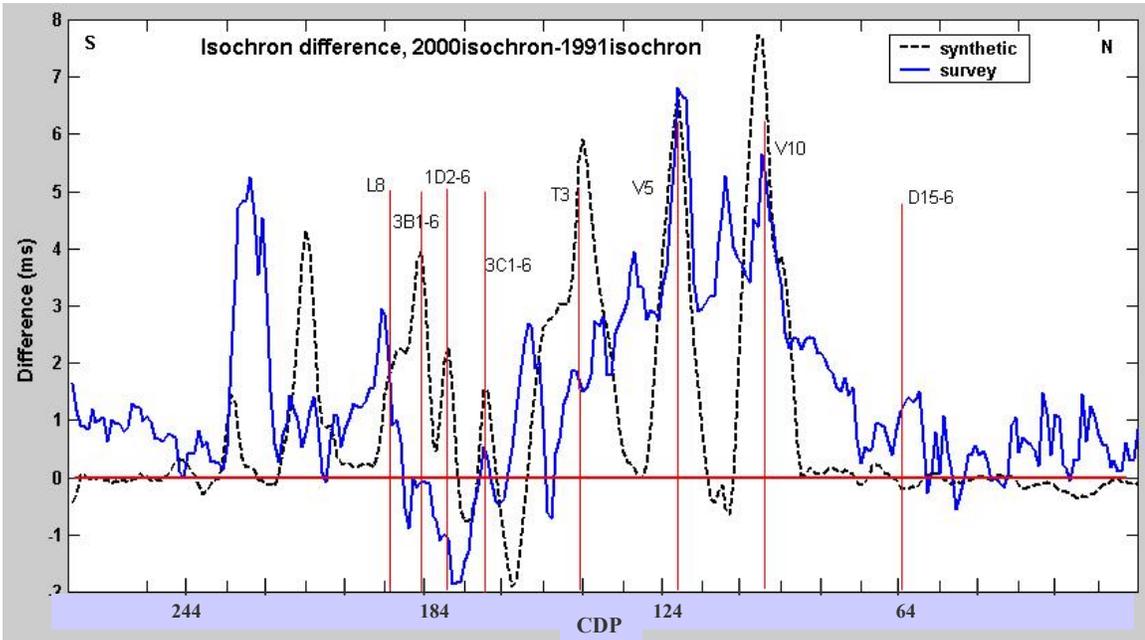

Figure 6.3 Isochron difference comparison. The CDP numbers for the seismic survey sections were converted to the synthetic seismic CDP number for easy comparison.

Overall, the features of the isochron ratio and the isochron differnce for the synthetic seismic sections are the similar the features for the real seismic survey sections. This indicates that the reservoir simulation and the followed synthetic modeling really reflect the in-situ reservoir conditions.

6.2.3   Reservoir properties vs. synthetic seismic difference sections

The simulated reservoir pressure distribution, gas saturations, temperature distribution, and oil saturations with synthetic seismic difference sections are plotted in Figure 6.4, 6.5, 6.6, and 6.7 for the three reservoir layers at the 1981, 1991, and 2000 time steps respectively. Pressure change is limited from CDP 190 to the southern end of the reservoir (Figure 6.4). The high pressure around well T3 is due to it being in the injection cycle in March 2000 (Figure 6.5). The lower pressure in the southern part may be because well Y1 (figure 4.5) was in CSS production since 1998.

According to the history data (Table 4.2) well 1D2-6, 3B1-6, and 3C1-6 have been in CSS operation since the early 1980s. Well L8's CSS operation started in 1983 and ended in 1997. L8, 1D2-6 and 3C1-6 were shut in from 1988 to 1992, and therefore, in 1991 the reservoir in this part was heated up but not significantly high(Figure 6.6). Wells T3, V5, and V10 began in CSS in 1995, 1996, and 1997 respectively. Large seismic difference energy appears around these active wells since they were not active during the 1991 survey. The temperature change between 1991 and 2000 to the south of well 1D2-6 is minimal (Figure 6.6). The difference energy visible around 600 ms and 750 ms at CDP locations100 to 200 corresponds to the increased gas saturation in the three reservoir layers (Figure 6.5). The thick gas zone plus high temperature lowers the velocity and causes large time delays (Figure 6.3). In the southern end of the reservoir, the gas

saturation only appears in the top layer. The difference energy is large in the top of the reservoir (Figure 6.5, CDP 30 to 70) with lesser changes below the reservoir level, because the lower velocity interval is restricted to the top layer, so time delay is minimal. This probably can explain the seismic energy at the southern end of the seismic survey difference section (Figure 6.1) on the top of the Waseca. The large time delay between Wells T3 and V10 is due to the combination of high temperature and high gas saturation. Figure 6.7 shows the oil saturation in the three layers. The northern end of the profile is the water zone for the model and oil and gas saturations are low.
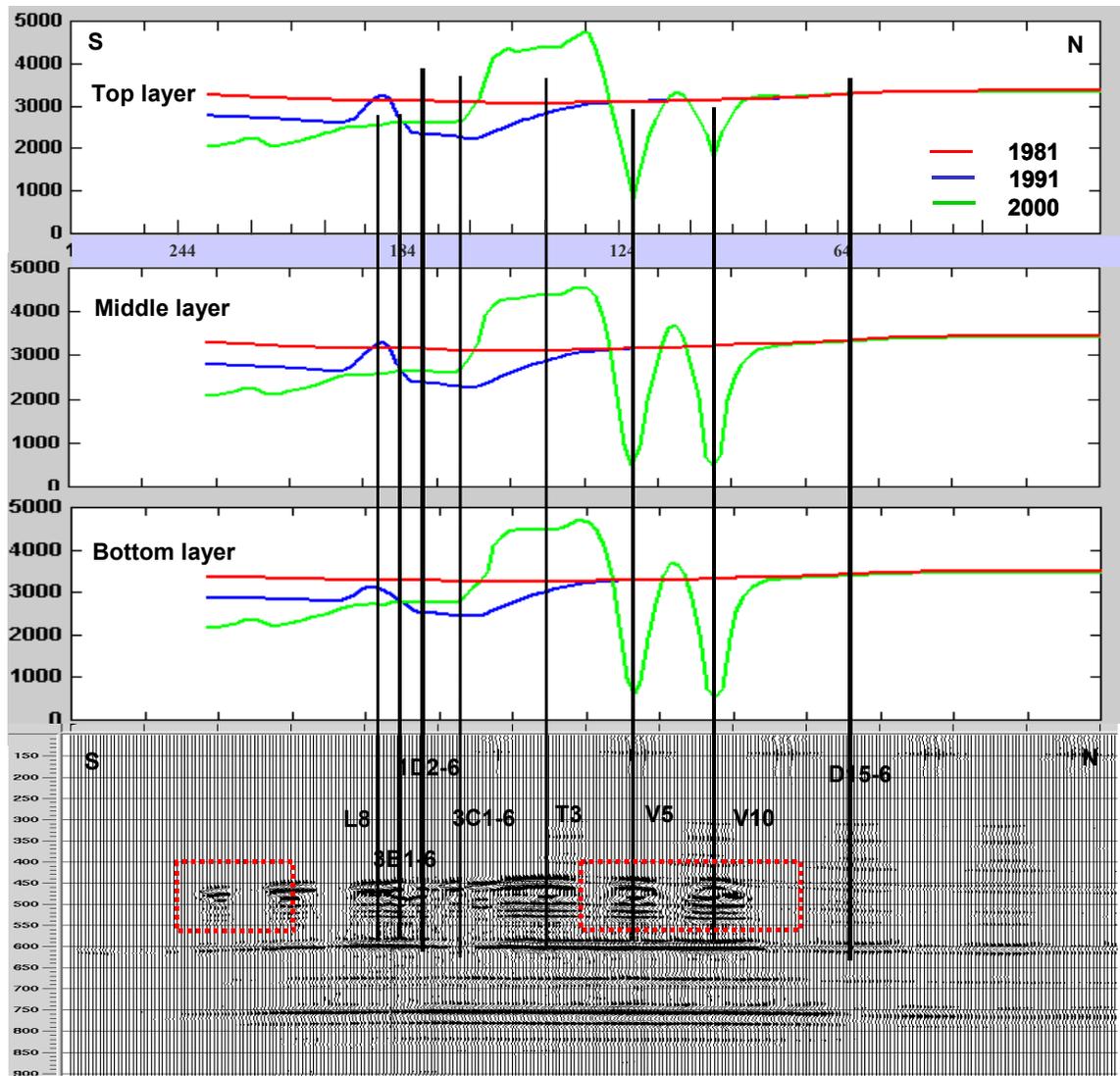
Figure 6.4 Reservoir pressure distribution in the three layers (up) and the synthetic seismic difference section (down).
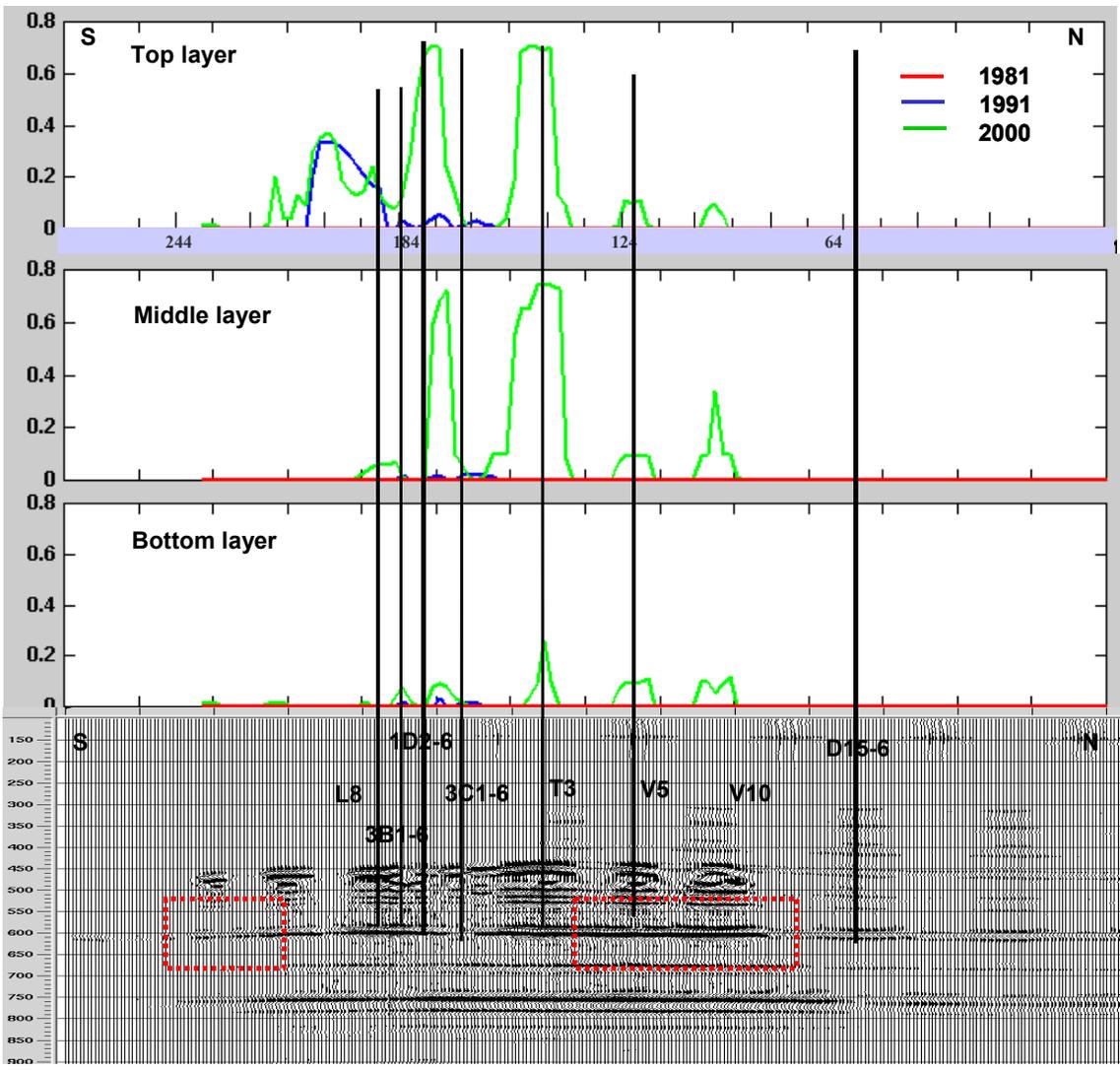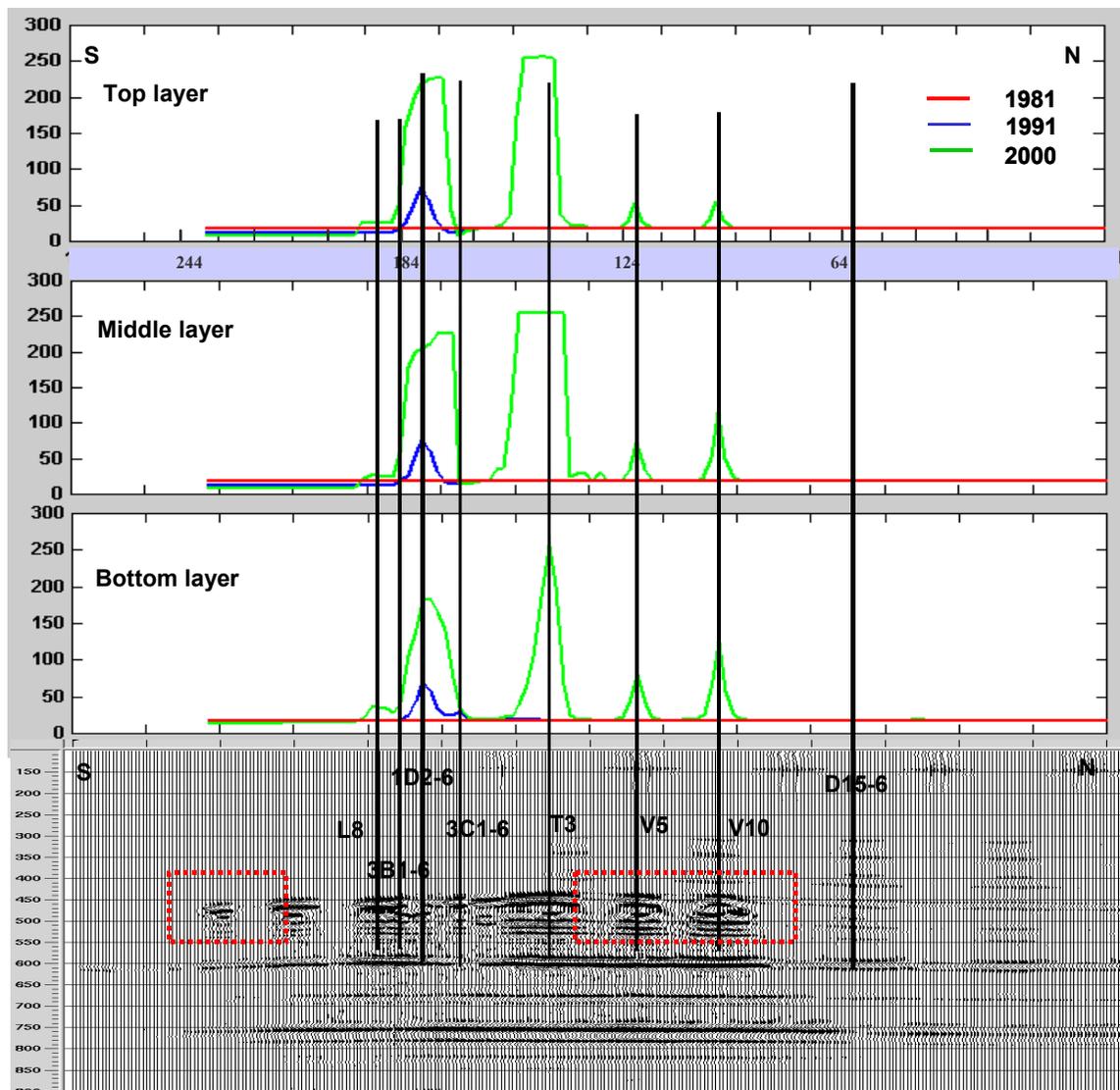
Figure 6.5 Reservoir gas saturation in the three layers (up) and the synthetic difference section (down).

Figure 6.6 Reservoir temperature in the three layers (up) and the synthetic difference section (down).
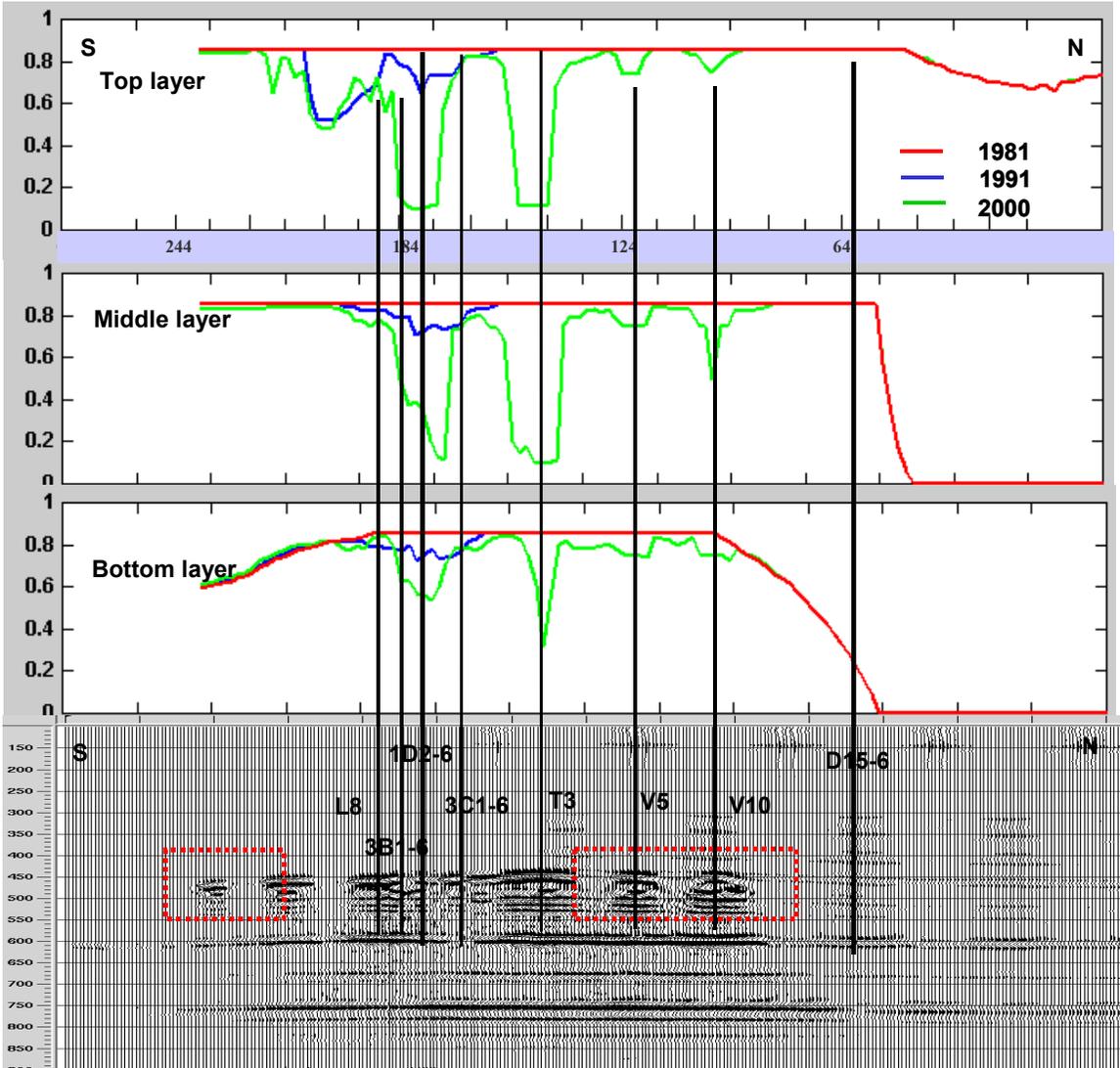
Figure 6.7 Reservoir oil saturation in the three layers (up) and the synthetic difference section (down).

6.3   Time-lapse AVO analysis

The reservoir simulation gives an approximate gas saturation distribution. In the

following it was investigated whether AVO analysis can be used to map gas zones. First,

to verify the AVO effect, AVO modeling was applied on the synthetic logs that are

extracted from the earth model for the synthetic seismic modeling. In Figure 6.8, the logs

before production are on the left side and the logs after production are on the right side. A

velocity decrease after production can be seen easily at the top of the reservoir. An AVO

modeling gather was generated from both pre-production and post-production logs. Then

the intercept and gradient stack (single trace) were derived. To see the effect better, the

two single traces of gradient were repeated 5 times in Figure 6.9 (wiggle traces). Then the

intercept and gradient was cross plotted (Figure 6.9, cross-plot). Most intercept and

gradient values are in the grey zone which is the background mud-rock line. The colour

key of the squares indicates the travel time of the values. The yellow and blue zones are

away from the mud-rock line and they are class 4 and class 3 gas sands according to

Castagna's classification.

The gas zones (in yellow and blue) that were picked outside the background zone (in

grey) are shown on the top of the reservoir after production (trace 6 to 10). The gas zone

marks outside the reservoir are due to non-production related factors. This modeling

result suggests that AVO analysis can be used to detect gas zones created by production.

Then, AVO analysis was implemented on the seismic lines. Before the AVO analysis,

super gathers were generated from groups of 5 CDP traces. The common offset stack

from the super gather has 12 offset bins. The original gathers and the common offset

stacks of the 1991 and the 2000 survey are plotted in Figure 6.10 and Figure 6.11.

A   B
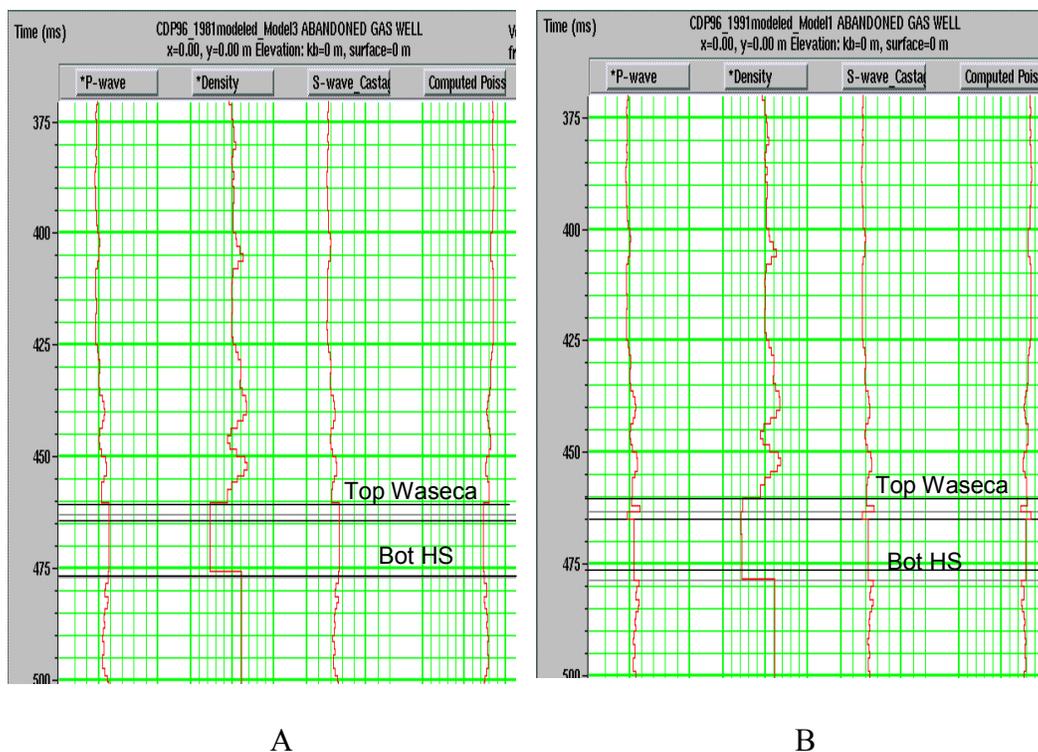
Figure 6.8 Synthetic logs from velocity and density models calculated from reservoir simulation output. A: synthetic logs before production. B: synthetic logs after production.

In the common offset stacks from the super gathers, the ground roll noise and random noise were suppressed. The three nearest offset traces were excluded because the ground roll noise was the dominant energy for these traces. The gradient and intercept stacks were then generated for the 1991 and 2000 survey. The cross plot for both the surveys is in Figure 6.12 and 6.14 respectively. The resulting gas zones interpreted from the gradient and intercept cross plots are shown in Figure 6.13 and 6.15. The gas zone for the 1991 survey follows the top of the reservoir along the crest of the formation. However, for the 2000 survey, the gas zones are not continuous and some are outside of the reservoir. Please note that some rocks have the same feature as gas sands on AVO cross plots. For example, some coal has the same AVO attributes as gas sand. Therefore, gas

sand stone has AVO effects but AVO effects can happen in other cases. On the other hand, the seismic surveys always have noise. The gas zones outside of the reservoir may be due to noise. The dominant trends of the gas zones are clearly outlined in spite of the noise. Please remember the gas may be methane or steam.
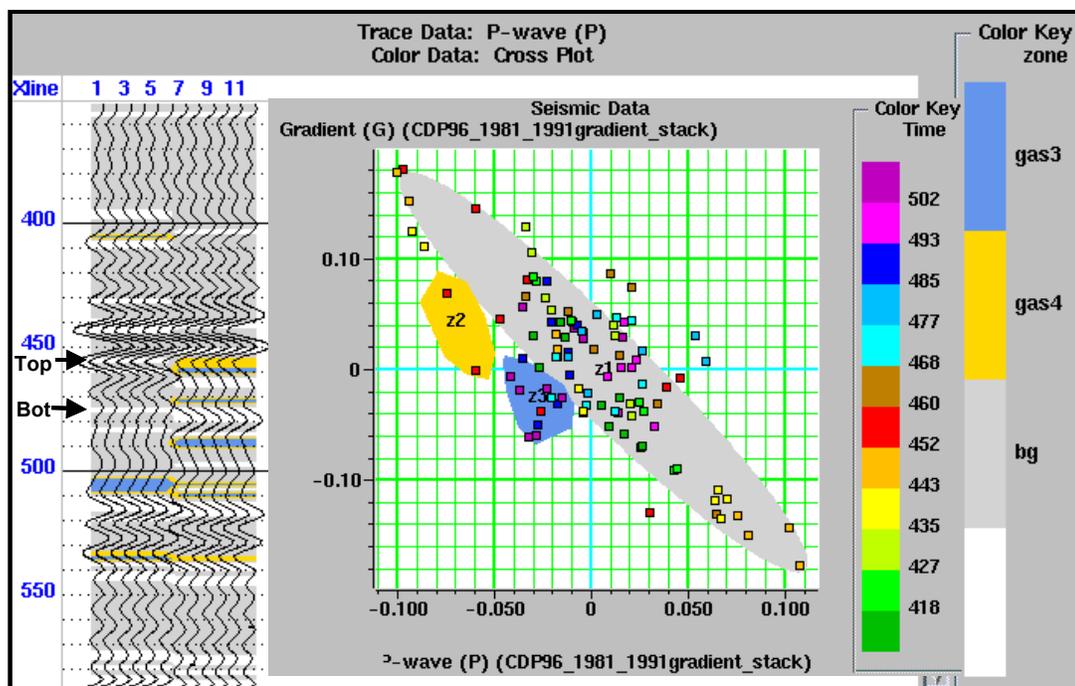
Figure 6.9 AVO analysis of the synthetic logs. The left wiggle traces are intercept stacks. Traces 1 to 5 are repeated traces for pre-production and traces 6 to 10 are repeated traces for post-production. The colour key time is the time in ms. The colour key zone indicates class 3 gas (blue), class 4 gas (yellow), and back ground mud-rock line (grey).
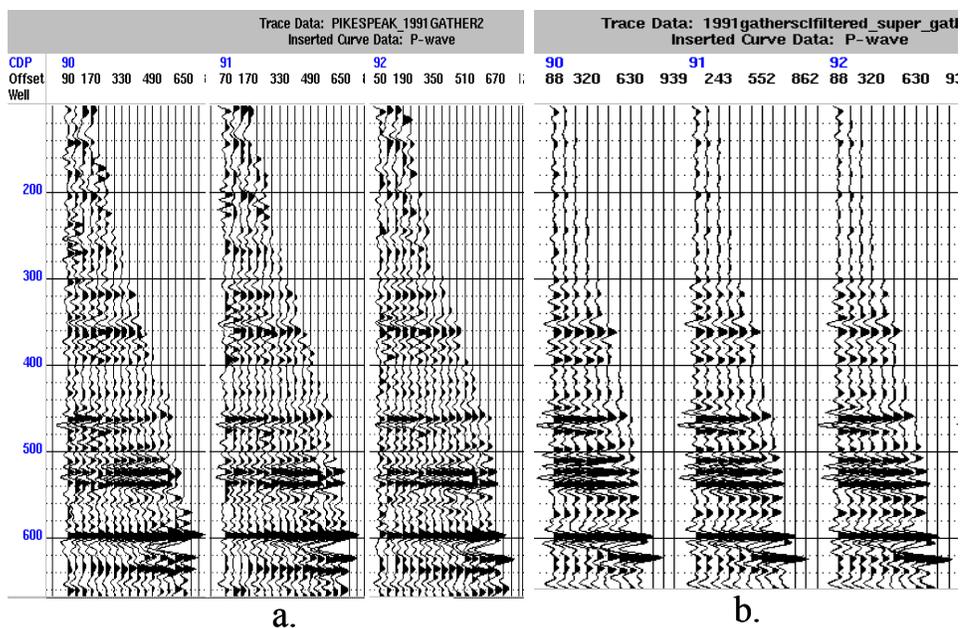
Figure 6.10 a. The original gathers of the 1991 survey with a bin size of 20 m. b. The common offset stacks generated by stacking every 5 CDPs and the offset bin size is 50 m.
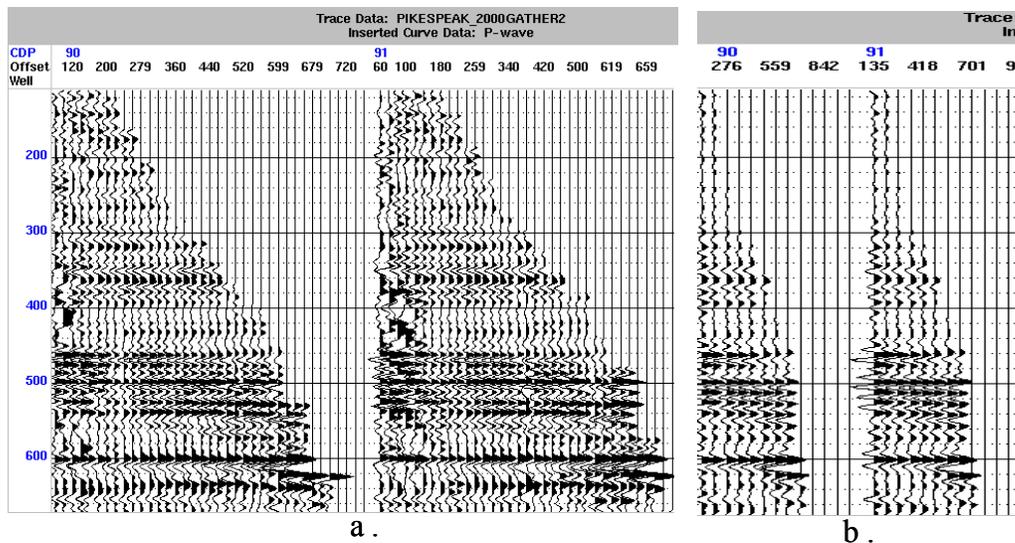

Figure 6.11 The original gathers of the 2000 survey with a bin size of 20 m. b. The common offset stacks generated by stacking every 5 CDPs and the offset bin size is 50 m.

To compare the gas zones from AVO analysis with the gas saturation from the reservoir simulation, the gas saturation from Figure 6.5, the gas zones from Figure 6.13, and the gas zones from Figure 6.15 are combined in Figure 6.16. The gas zones derived from AVO cross plots on both the 1991 survey and 2000 survey correspond to the gas saturation patterns in general. In 1991, gas saturation only happened in the top layer and the gas saturation is around well 1D2-6. But the gas zones in the AVO cross-section extended to well V5. The correlation of AVO derived gas zones and gas saturation for the 2000 survey is better than the 1991 survey. The gas zones on the AVO cross-section at Wells V10, V5, and south of L8 match the gas saturation in the top layer very well. The miss match of gas zones and gas saturation happens around well 1D2-6 and T3. The gas zones from the AVO method are only based on seismic data and the gas saturation distribution is mainly based on the engineering method. The two methods both have assumptions and limitations as mentioned in Chapter 3 and Chapter 4. The gas zones around wells L8 to 3C1-6 in 1991 and the gas zones around wells L8, V5, and V10 in 2000 are on both the independent methods, the possibility that they exist should be very high. Again we have to remember that the gas saturation may be steam or methane. To differentiate between steam and evolved methane, the temperature distribution from reservoir simulation should be considered. A gas phase with low temperature would denote vaporized methane.

Figure 6.12 Cross plot of the 1991 seismic survey 100 ms around reservoir top.

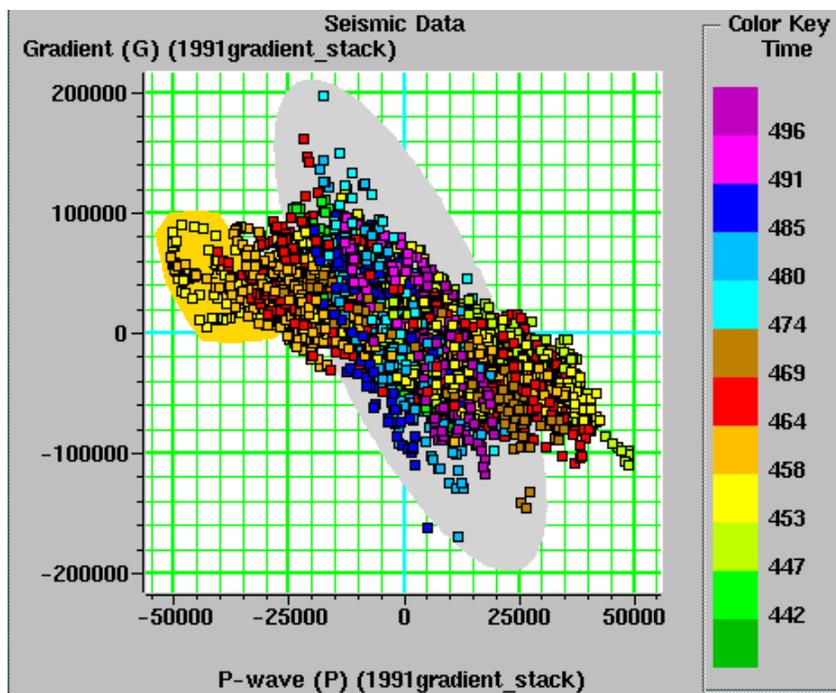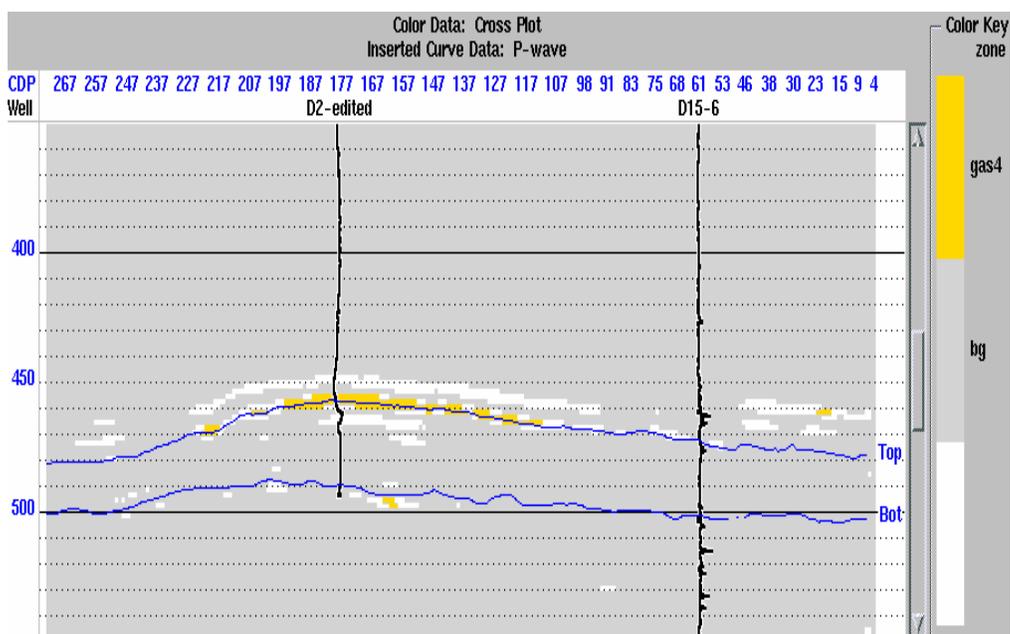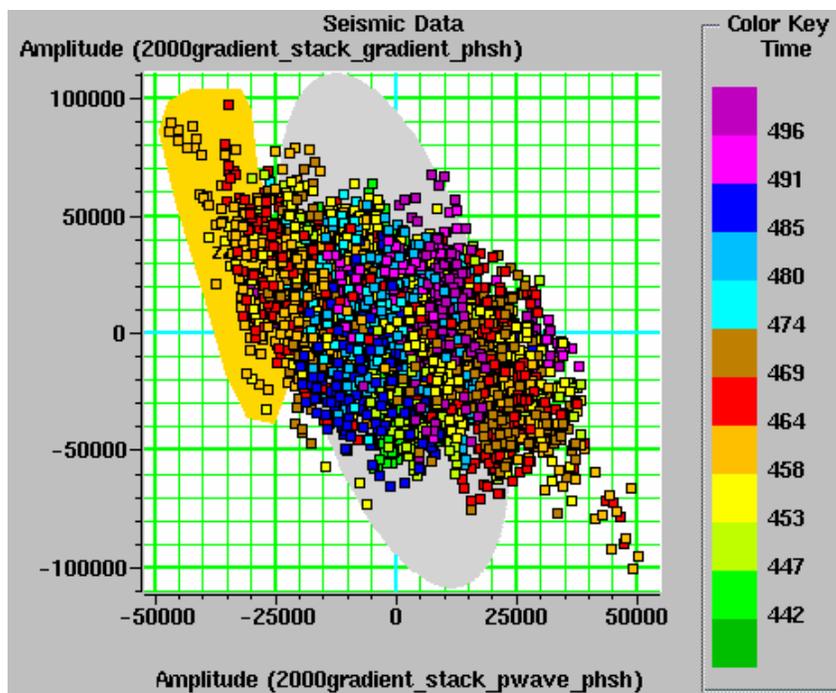**Figure 6.13 Cross section of the 1991 seismic AVO analysis.**

Figure 6.14 Cross plot of the 2000 seismic survey 100 ms around reservoir top.
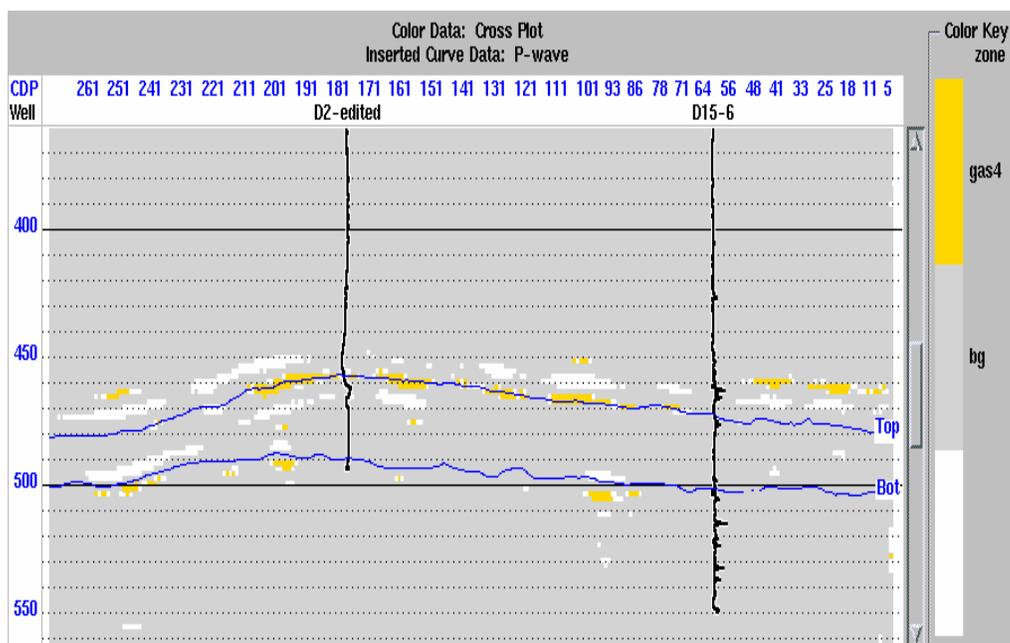

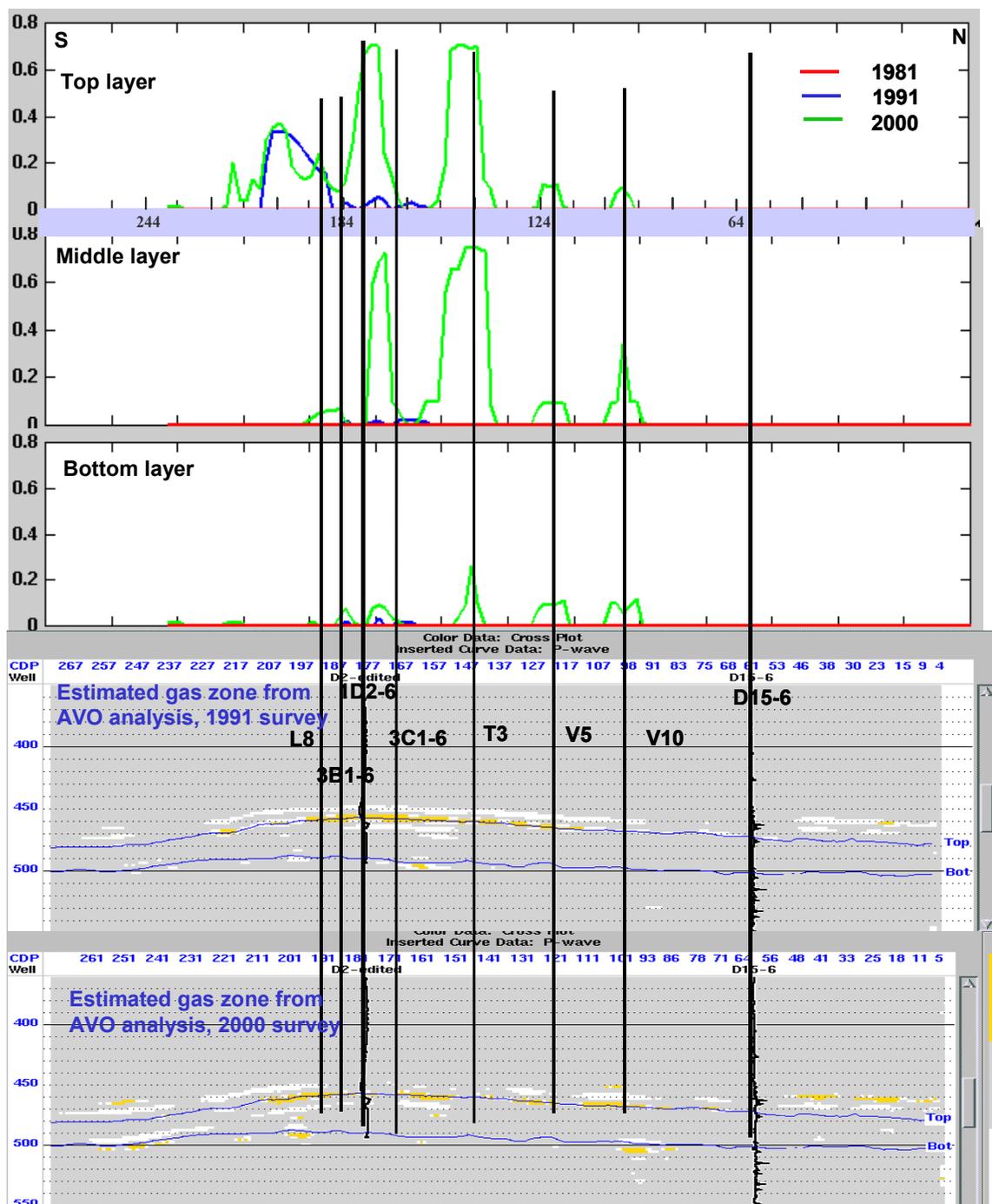**Figure 6.15 Cross section of the 2000 seismic AVO analysis.**

Figure 6.16 The comparison of AVO derived gas zone and the gas saturation from the reservoir simulation. The vertical lines are well positions.

6.4   Time-lapse inversion

Watson (2004) did post stack inversion using older versions (processed by Matrix Geophysical Services) of processed sections. Since the seismic surveys have been reprocessed for this study, it is worthwhile to see the inversion results using the updated processing methods. Inversion is a process that uses the observed data to get the earth model in the form of impedance. An inversion result for a seismic section is an impedance section. Impedance is the multiplication of velocity and density and it is the property of a medium.

The method that was used is model-based inversion. The inversion tests using AVO derived P wave stacks were checked. The good cross-equalization between the P wave stack of 1991 survey and the P wave stack of 2000 survey could not be obtained. Therefore, the final stacks of the 1991 and 2000 surveys are the inputs for the inversion; and P wave and density logs from four wells were used to create a model. The resultant acoustic impedance stacks are shown in Figure 6.17. Figure 6.17 a. is for the 1991 survey and Figure 6.17 b. is for the 2000 survey. High values are in red and low values are in blue. The difference impedance stack is in Figure 6.18. It was derived by subtracting the 2000 acoustic impedance stack from the 1991 acoustic impedance stack. Positive values mean the acoustic impedance decreased in 2000. The zones with the largest decreases correspond to the production areas (CDP 90 to 180, Figure 3.7). The other high value differences outside the reservoir may be caused by noise and they are not significantly large.
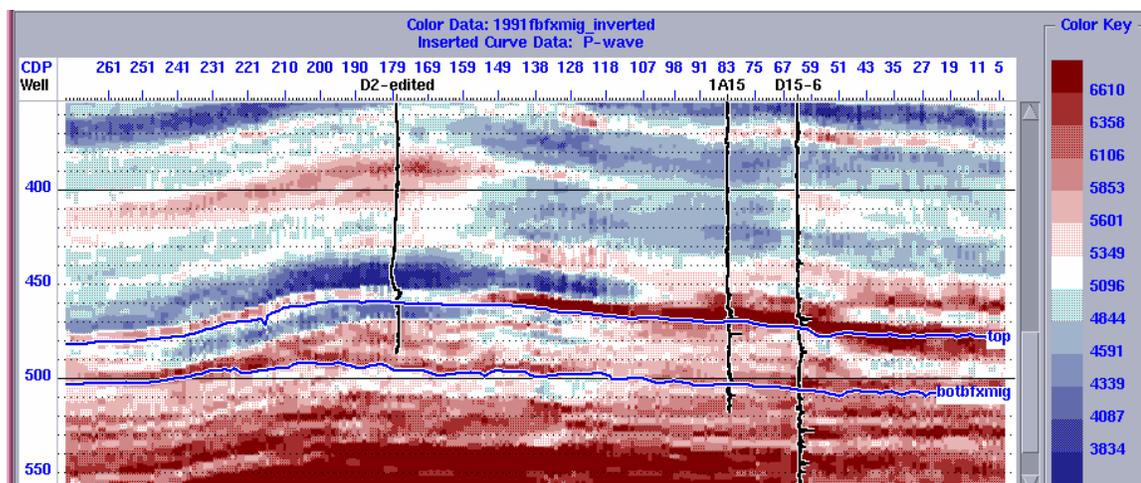
a.
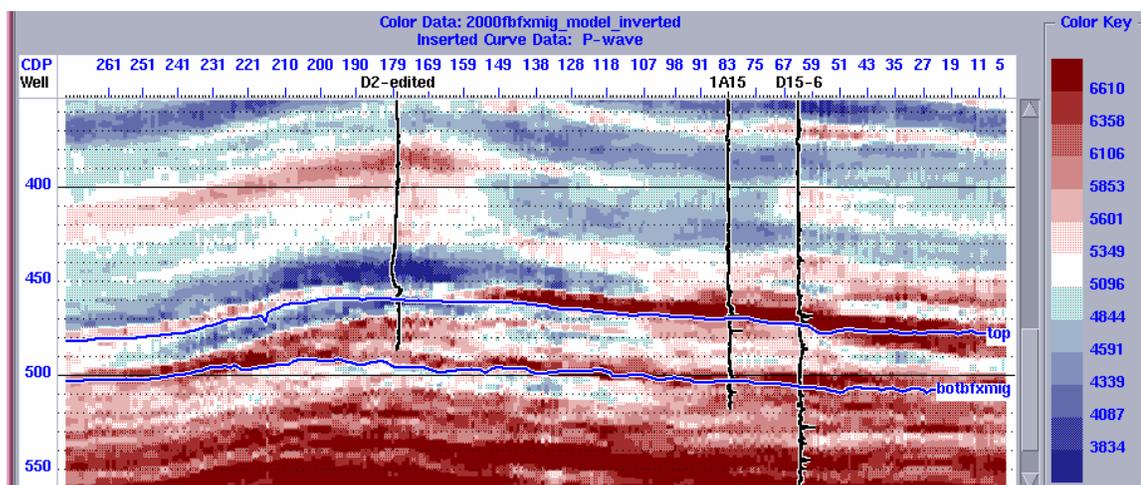
b.

Figure 6.17 Impedance sections from model based inversion. a., the 1991 P impedance, b., the 2000 P impedance. The unit is m/s g/cm^3.
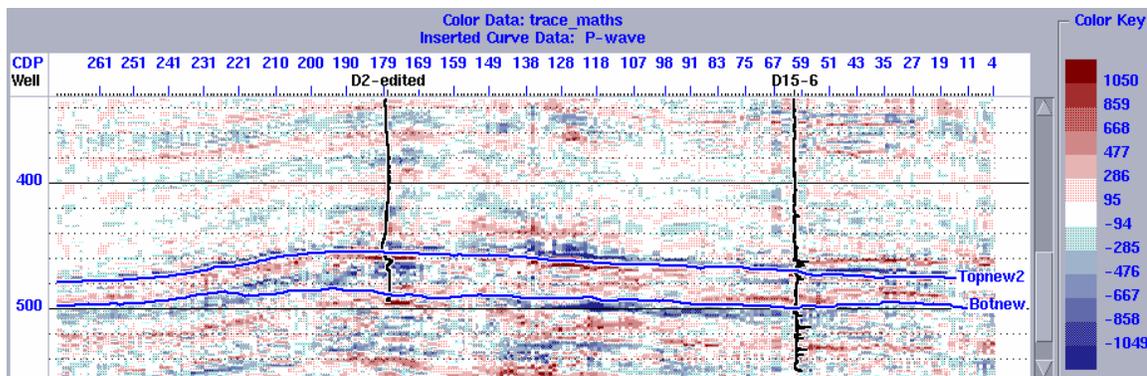
Figure 6.18 The impedance difference (1991 impedance minus 2000 difference). The circled areas have largest values.

6.5   Discussion

Interpretation is a procedure to integrate all of the information that one has to make conclusions. The individual information may be biased from the reality in different directions. Both seismic method and reservoir simulation have their own limitations. A seismic section can be contaminated by noise and equipment imperfection during acquisition. The processing method and software may also bring some errors. Reservoir simulation is based on a simplified model. The geometry of the reservoir model may have influence on the fluid saturation distributions. For the current reservoir model, the horizontal grid size (20 m) is larger than the CDP interval (10 m). I did interpolation on the grid values of the reservoir simulation results. Also, the vertical sizes of some grids (homogenous layer) are around 17 m for the third layer. I have discussed seismic resolution in Section 3.5. It is around 12.5 m. The coarse grids in the reservoir simulation may have some impact on the results. Since the machine power is not suitable for a big reservoir simulation job, it takes two days for a simulation run to finish for the present model. It was not realistic for me to refine the model further.
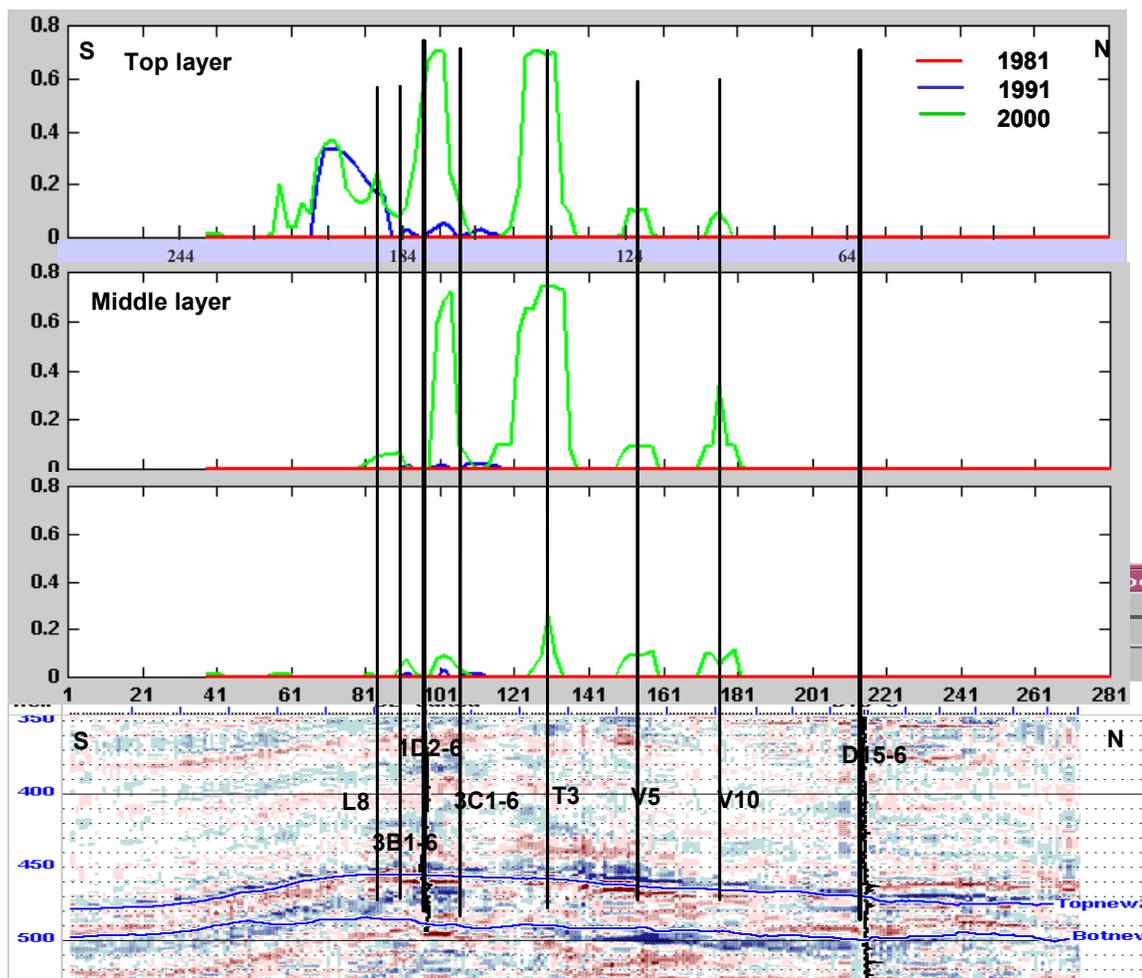
Figure 6.19: The impedance difference vs. gas saturation from reservoir simulation.

6.6   Conclusions

The results from the geophysical method are consistent with the results from the reservoir engineering study on the large scale. Referencing the reservoir engineering information, the following seismic interpretation has been obtained.

The large seismic difference energy corresponds to the thick gas phase zone with high temperatures that cause the longer seismic traveltime. This zone is very likely to be a

steam zone. The southern end seismic difference energy is due to the lower pressure that causes solution gas to vaporize.

The AVO analysis has shown that the AVO method can be used to detect steam and free gas zones. The impedance difference stack clearly outlined the largest impedance change zones and they are consistent with reservoir production activity.

**Chapter Seven:	Conclusions and future work**

**7.1	Conclusions**

The two time-lapse 2D seismic lines acquired in February 1991 and March 2000 are located in the eastern part of the Pikes Peak heavy oil field. They are in the area that has been undergoing CSS production processing. The carefully designed time-lapse seismic processing has successfully gained wavelet and structure matched time-lapse seismic final sections. Three scaling methods were investigated, conventional scaling, surface consistent scaling, and two mean window scaling, during the processing. The three processed difference sections were compared with isochron analysis and production activities. The conventional scaling method with multiple mean windows above the reservoir and one mean window including the reservoir gave the result most consistent with production information. Time-lapse seismic processing should be set to preserve signal amplitude and suppress noise amplitude rather than preserve all amplitude from acquisition.

The reservoir simulation based on the field reservoir production history for the 21 wells in the reservoir model, has provided a second information source for the time-lapse seismic analysis. The developed rock physics procedure based on Gassmann's equation and Batzle and Wang's empirical relationship successfully linked seismic method to reservoir engineering. The developed rock physics procedure can be applied to any reservoir fluid substitution analysis and can calculate both P wave velocity and S wave velocity. The resulting seismic model can be used for both PP wave and PS wave modeling.

Comparing the synthetic seismic difference section with the seismic survey difference section using saturation, temperature, and pressure results from the reservoir simulation. The following conclusions are drawn:

The areas with a gas saturation difference between two compared time steps have seismic differences because the presence of gas reduces the bulk modulus and bulk density of the saturated rock. Thicker gas zones correspond with larger traveltime delays in the seismic section. The thin gas zones only induce large reflectivity, and do not have enough time delay to have strong seismic difference in the deeper regions below the reservoir zone. High temperature regions also correlate with areas having large seismic energy differences. High temperature and thick gas (steam and methane) zones may be evidence for steam existence. The difference in the seismic energy in the southern end of the section is due to the lower pressure that causes solution gas to evolve. Pressure changes propagate much quicker (~20 m in one month) than temperature changes (~8 m in a year) for the Pikes Peak reservoir. The pressure dependence of the seismic data is due to its influences on gas saturation. The present model for reservoir simulation is very close to reality, although there is still room to improve it. Therefore, the bypassed oil area and steam front (high temperature front) can be estimated on the temperature and oil saturation distributions from the reservoir simulation.

This work demonstrates that with the rock physics procedure, joint interpretation between geophysics and reservoir engineering can be done directly by comparing the field seismic survey difference section and the synthetic seismic difference section which is based on reservoir simulation outputs. This integration study of the seismic method with reservoir simulation has enabled the explanation of seismic energy outside the reservoir and also

has given the reasons for the seismic difference energy in different locations on the seismic difference section from the engineering source of information. This is very helpful for seismic interpretation since the CSS processes for different wells are interfering with each other and therefore it is hard to distinguish between production produced seismic difference and data error.

This case has also demonstrated that the AVO method can be used to detect steam and vaporized gas zones. The impedance difference stack clearly shows the largest impedance change zones and they are consistent with reservoir production activity.

7.2   Future work

In terms of geophysics, I will try noise attenuation (very carefully) to get rid of some of the ground roll noise. Pre-stack migrations, both in time and depth, are also on my list of future endeavours. Pre-stack time migration may give a more focused seismic image and then the heat zones may have clearer resolution. Pre-stack depth migration can be used to construct an earth model that is closer to the real structure for both reservoir simulation and seismic modeling. I would also like to further research converted wave modeling and compare it with the processed PS sections. In terms of reservoir engineering, this thesis work was an effort to integrate the two branches of the oil and gas industry. This thesis has shown that an extra source of information from reservoir engineering can help the interpretation of seismic images. The reservoir model grids need to be downsized to match the seismic CDP interval. The reservoir model parameters also need to be checked in detail. These tasks will require the expertise of reservoir engineers. The future of oil and gas exploration depends upon the collaboration of geophysicists, geologists, and reservoir engineers.

References

Batzle, M. and Wang, Z., 1992, Seismic properties of pore fluids: Geophysics, **57**, No. 11, 1396-1408.

Biondi, B., Mavko, G., Mukerji,T., Rickett, J., Lumley, D., DeuTsch, C., Gundeso, R. and Thiele, M., 1998, Reservoir Monitoring: A Multidisciplinary feasibility study: The Leading Edge, **17**, No. 10, 1404-1414.

Bullen, K. E., 1963, An introduction to the theory of seismology: 3rd edition, Cambridge University Press.

Clark, M. S. and Klonsky, L. F., 2001, Geologic study and multiple 3-D surveys give clues to complex reservoir architecture of giant Coalinga oil field, San Joaquin Valley, California: The Leading Edge, **20**, No. 7, 744-751.

Core Laboratories, 2000, Advanced rock properties study for the University of Calgary: Internal report, 52132-00-1008, 52132-001085.

den Boer, L. D. and Matthews, L. W., 1988, Seismic characterization of thermal flood behavior: Proc. of the 4th International conference on heavy crude and tar sands (Unitar), Edmonton, **4**, 613-627.

Downton, J. and Lines, L., 2000, Preliminary results of the AVO analysis at Pike's Peak: CREWES (The Consortium for Research in Elastic Wave Exploration Seismology) Report, **12**, 523-531.

Eastwood, J., Lebel, P., Dilay, A., and Blakeslee, S., 1994, Seismic monitoring of steam-based recovery of bitumen: The Leading Edge, **13**, No. 4, 242-251.

Greaves, R. J. and Fulp, T. J., 1987, Three-dimensional seismic monitoring of an enhanced oil recovery process: Geophysics, **52**, No. 9, 1175-1187.

Hoffe, B. H., Bertram, M. B., Bland, H. C., Gallant, E. V., Lines, L. R., and Mewhort, L. E., 2000, Acquisition and processing of the Pikes Peak 3-C 2-D seismic survey: CREWES Research Report, **12**, 511-522.

Hedlin, K., Mewhort, L. and Margrave, G., 2001, Delineation of steam flood using seismic attenuation: 2002 Canadian Society of Exploration Geophysicists (CSEG) Annual Mtg, Calgary, Alberta.

Isaac, H., 1996, Seismic methods for heavy oil reservoir monitoring: Ph.D. thesis, Dept. of Geology and Geophysics, Univ. of Calgary.

Jack, I., 2003, Time-lapse seismic in reservoir management: CSEG Continuing education Doodle Train course note.

Jenkins, S. D., Waite, M. W. and Bee, M. F., 1997, Time-lapse monitoring of the Duri steamflood: a pilot and case study: The Leading Edge, **16**, 9, 1238-1274.

Johnston, D. H., McKenny, R. S., Verbeek, J. and Almond, J., 1998, Time-lapse seismic analysis of Fulmar Field: The Leading Edge, **17**, 10, 1420-1428.

Johnston, D. H., Eastwood, J. E., Shyeh, J. J., Vauthrin, R., Khan, M., and Stanley, L. R., 2000, Using legacy seismic data in an integrated time-lapse study: Lena Field, Gulf of Mexico: The Leading Edge, **19**, 294-302.

Lumley, D.E., 1995, Seismic time-lapse monitoring of subsurface fluid flow: Ph.D. thesis, Stanford University.

Lumley, D. E., 2001, Time-lapse seismic reservoir monitoring: Geophysics, **66**, 1, 50-53.

Miller, K. A., Stevens, L. G. and Watt, B. J., 1987, Successful conversion of the Pikes Peak viscous-oil cyclic steam project to steamdrive: Society of Petroleum Engineers (SPE) 18774.

Miller, K. A. and Given, R. M., 1989, Evaluation and application of Pikes Peak cyclic steam injection pressure data: The Journal of Canadian Petroleum Technology, **28**, No. 1, 26-32.

Mavko, G. and Mukerji, T., 1998, Bounds on low-frequency seismic velocities in partially saturated rocks: Geophysics, **63**, No. 3, 918-924.

Najjar, N. F., Stronen, L. K., and Alsos, T, 2003, Time-lapse seismic programme at Gullfaks: value and the road ahead: Petrolum Geoscience, **9**, 2003, 33-41.

Pullin, N. E., Jackson, R. K., Matthews, L. W., Thorburn, R. F., Hirsche, W. K. and den Boer, L. D, 3-D Seismic imaging of heat zones at an Athabasca Tar sands thermal pilot: Society of Exploration Geophysicists annual convention, 1987.

Rickett, J. E., and Lumley, D. E., 2001, Cross-equalization data processing for time-lapse seismic reservoir monitoring: A case study from the Gulf of Mexico: Geophysics, **66**, 1, 1015-1025.

Ross, C. P., Cunningham, G. B., and Weber, D. P., 1996, Inside the crossequalization black box: The Leading Edge, **15**, 1233-1240.

Ross, C. P. and Altan, M. S., 1997, Time-lapse seismic monitoring: some shortcomings in nonuniform processing: The Leading Edge, The Leading Edge, **16**, 1021-1027.

Schmitt, D. R., 1999, Seismic attributes for monitoring of a shallow heated heavy oil reservoir: A case study: Geophysics, **64**, 1, 368-377.

Settari, A., 2001, Topics in Reservoir Simulation: Course Notes.

Sheppard, G.L., Wong F.Y. and Love D., 1998, Husky's success at the Pikes Peak thermal project: UNITAR Conference, Beijing, China.

Stewart, R. R., Lines, L. R. and Mewhort, L. E., 2000, Multicomponent VSP and lake-bottom cable surveys-Pikes Peak, Saskatchewan: CREWES Research Report, 12, 35-42.

Talwani, M., 2003, Will Calgary be the next Kuwait? Editorial Desk: The New York Times, August 14, 2003

Tosoya, C., Nur, A., Vo-Thanh, D. and Prat, G. D., 1987, Laboratory seismic methods for remote monitoring of thermal EOR: SPE 12744.

Van Hulten, F.F.N., 1984, Petroleum geology of Pikes Peak heavy oil field, Waseca Formation, Lower Cretaceous, Saskatchewan: Canadian Society of Petroleum Geologists, Memoir 9, 441-454.

Watson, I.A., Lines, L. and Brittle K.F., 2002, Heavy-oil reservoir characterization using elastic wave properties: The Leading Edge, **21**, 736-739.

Watson, I.A. and Lines, L., 2003, Geological interpretations from seismic data at Pikes Peak, Saskatchewan: CREWES Research Report, **15**.

Watson, I.A., 2004, Integrated geological and geophysical analysis of a heavy-oil reservoir at Pikes Peak, Saskatchewan: M.Sc. thesis, Dept. of Geology and Geophysics, Univ. of Calgary.

Wang, Z. and Nur, A., 1992, Elastic wave velocities in porous media: A theoretical recipe in seismic and acoustic velocities in reservoir rocks, Theoretical and Model Studies: Society of Exploration Geophysicists, **2**, 1-35.

Wang, Z. and Nur, A., 1986, The effect of temperature on the seismic wave velocities in rocks saturated with hydrocarbons: Soc. Petr. Eng. (SPE) paper 15646, Proc. 61st Soc. Petr. Eng. Tach. Conf.

Wang, Z., Batzle, M. and Nur, A., 1988, Seismic velocities in heavy oil and tar sands: the basis for in situ recovery monitoring: Proc. of the 4th International conference on heavy crude and tar sands (Unitar), Edmonton, **4**, 601-611.

Wang, Z. and Nur, A., 2000, The Gassmann Equation Revised: Comparing Laboratory Data with Gassmann's Predictions: Seismic and acoustic velocities in reservoir rocks, Recent Developments, Society of Exploration Geophysicists, **3**, 1-35.

Wong, F. Y. F., Anderson, D. B., O'Rourke, J. C., Rea, H. Q. and Scheidt, K. A., 2001, Meeting the challenge to extend success at the Pikes Peak steam project to areas with bottom water: SPE 71630,

Xu, C., 2001, Processing the Pikes Peak walkaway VSP survey and estimating a Q-factor: AOSTRA Project 1296.

Yilmaz, O., 1991, Seismic data processing: Society of Exploration Geophysicists, 1991, Fifth printing.

Zhang, H., 2003, Interpretive PP and PS joint inversion: M.Sc. thesis, Dept. of Geology and Geophysics, Univ. of Calgary.

Zou, Y., Bentley, L. R. and Lines, L. R, 2002, Time-lapse seismic modeling of the Pikes Peak field: CREWES Research Report, **14**.
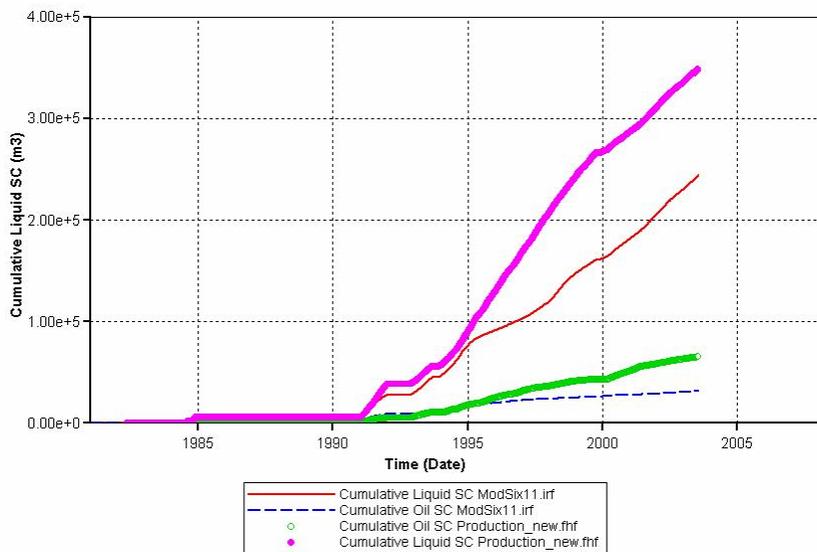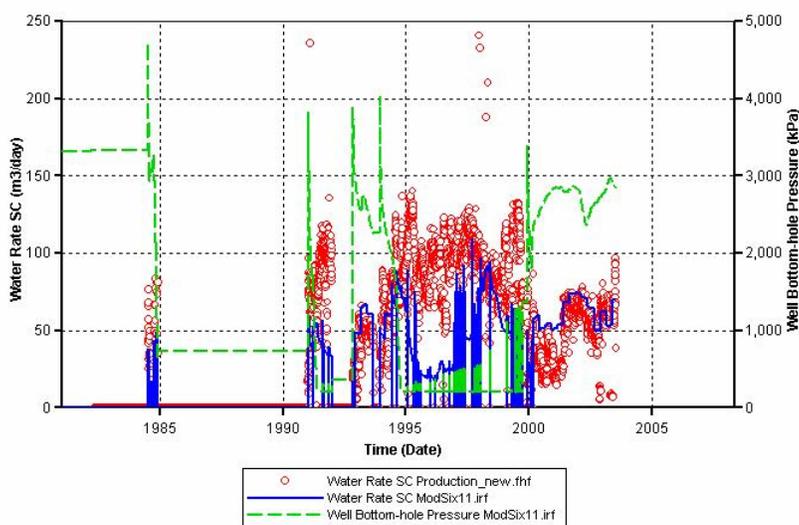
Appendix 1
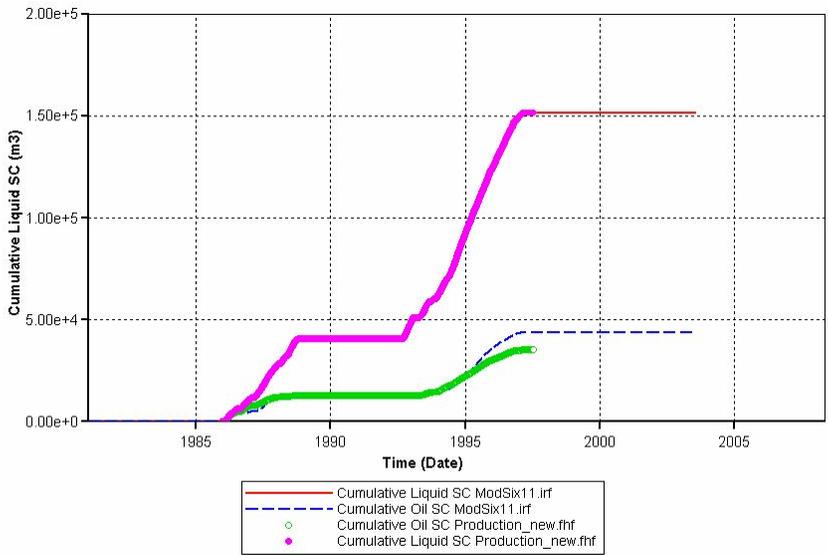
Figure. A.1 History matching results of cumulative liquid and cumulative oil production for well L8 in standard condition. The pink dots are the cumulative liquid productions from the history file. The red line is the cumulative liquid production from the simulation output. The green dots are the cumulative oil production from the history file. The blue dash line is the cumulative oil production from the simulation output.
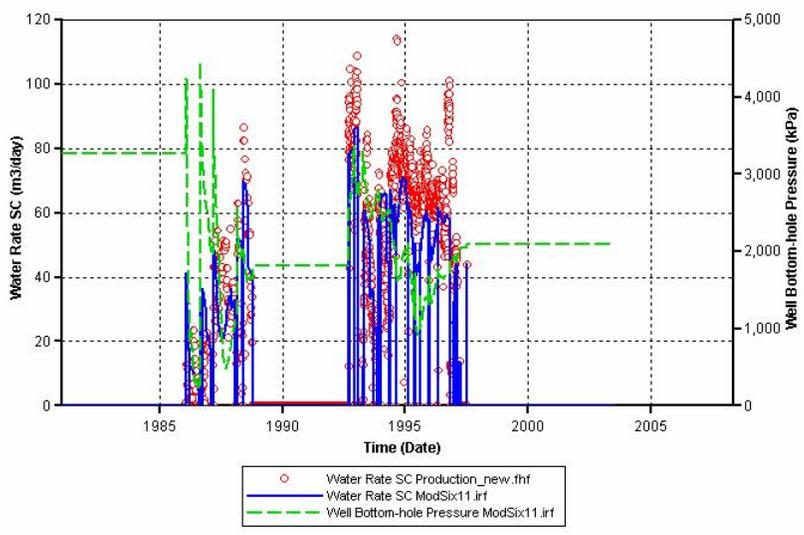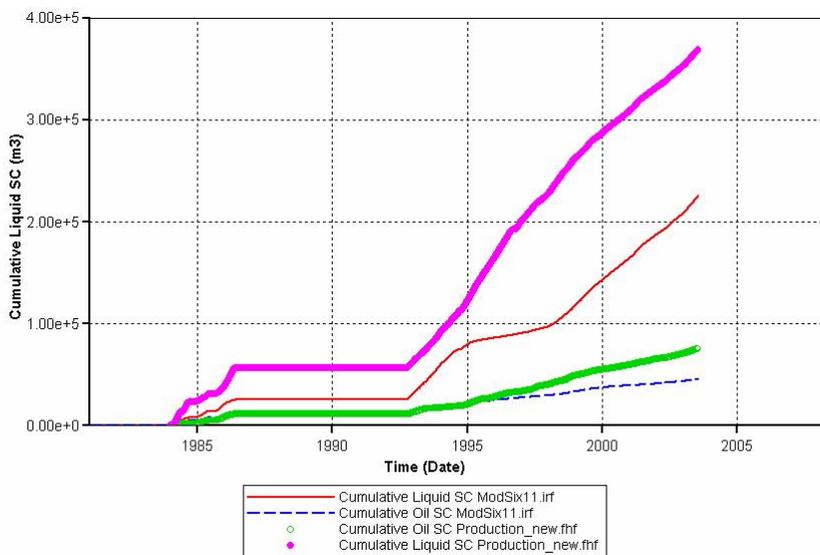

Figure A.2 History matching results of water rate and bottom hole pressure for well L8. The red dots are the water rate in standard condition from the history file. The blue line is the water rate in standard condition from the simulation output. The green dash line is the well bottom-hole pressure from the simulation output (there is no pressure history file).
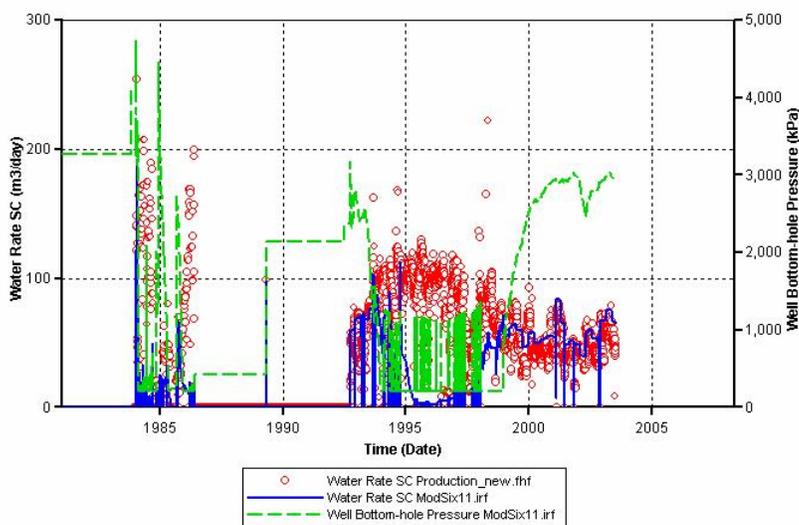
Figure. A.3 History matching results of cumulative liquid and cumulative oil production for well 3B1-6 in standard condition. The pink dots are the cumulative liquid productions from the history file. The red line is the cumulative liquid production from the simulation output. The green dots are the cumulative oil production from the history file. The blue dash line is the cumulative oil production from the simulation output.
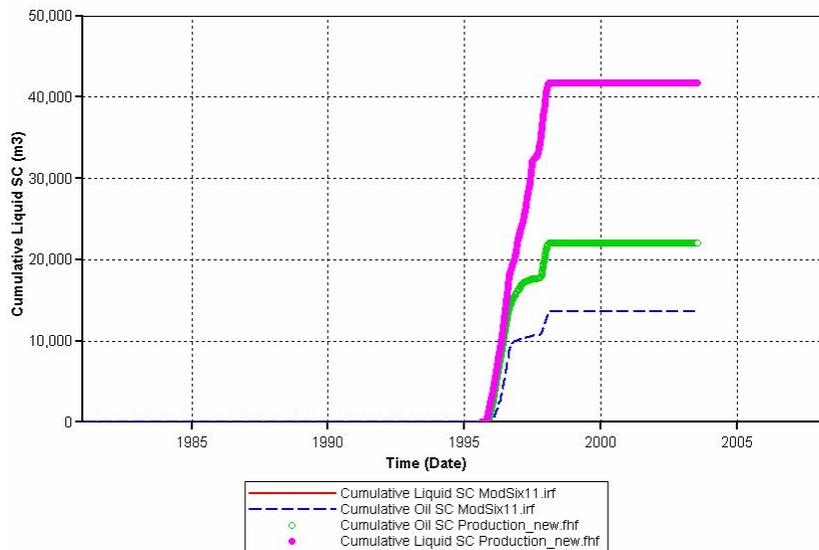

Figure A.4 History matching results of water rate and bottom hole pressure for well 3B1-6. The red dots are the water rate in standard condition from the history file. The blue line is the water rate in standard condition from the simulation output. The green dash line is the well bottom-hole pressure from the simulation output (there is no pressure history file).
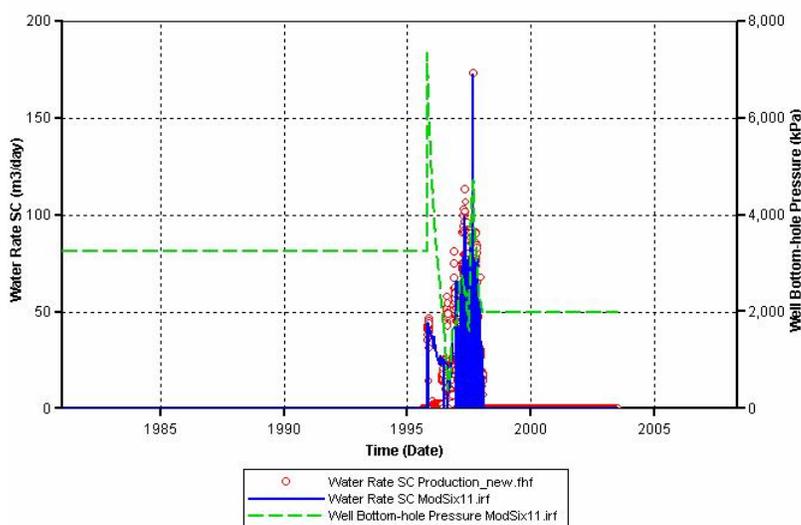
Figure. A.5 History matching results of cumulative liquid and cumulative oil production for well 3C1-6 in standard condition. The pink dots are the cumulative liquid productions from the history file. The red line is the cumulative liquid production from the simulation output. The green dots are the cumulative oil production from the history file. The blue dash line is the cumulative oil production from the simulation output.
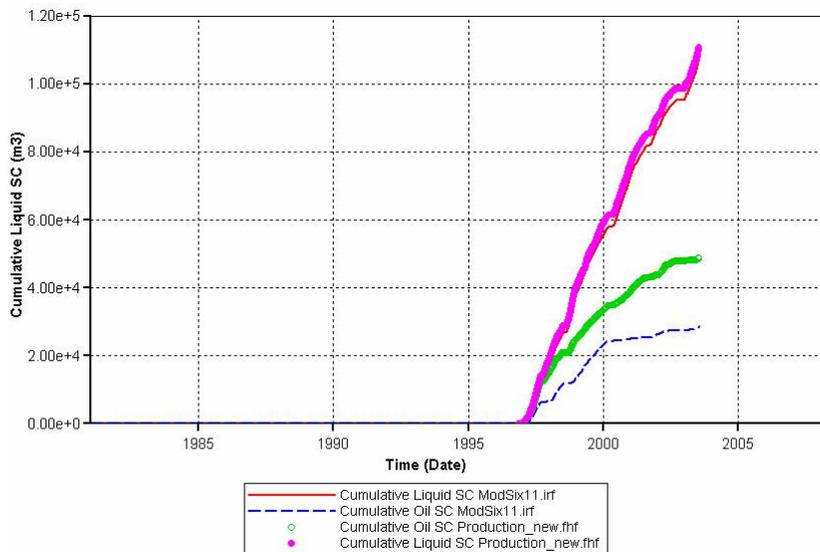

Figure A.6 History matching results of water rate and bottom hole pressure for well 3C1-6. The red dots are the water rate in standard condition from the history file. The blue line is the water rate in standard condition from the simulation output. The green dash line is the well bottom-hole pressure from the simulation output (there is no pressure history file).
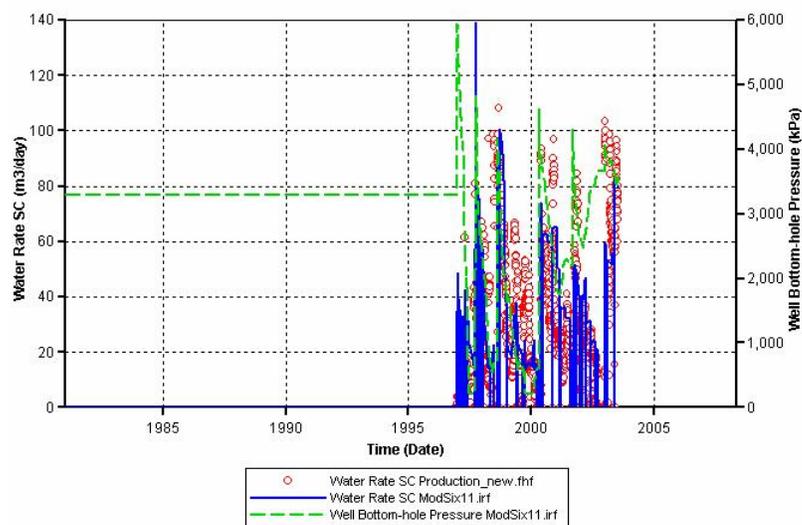
Figure. A.7 History matching results of cumulative liquid and cumulative oil production for well T3 in standard condition. The pink dots are the cumulative liquid productions from the history file. The red line is the cumulative liquid production from the simulation output. The green dots are the cumulative oil production from the history file. The blue dash line is the cumulative oil production from the simulation output.
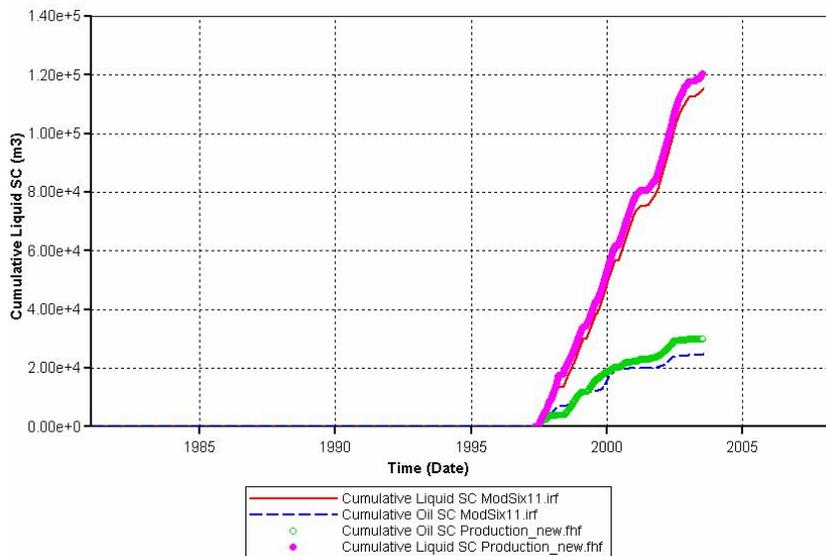

Figure A.8 History matching results of water rate and bottom hole pressure for well 4A2-6. The red dots are the water rate in standard condition from the history file. The blue line is the water rate in standard condition from the simulation output. The green dash line is the well bottom-hole pressure from the simulation output (there is no pressure history file).
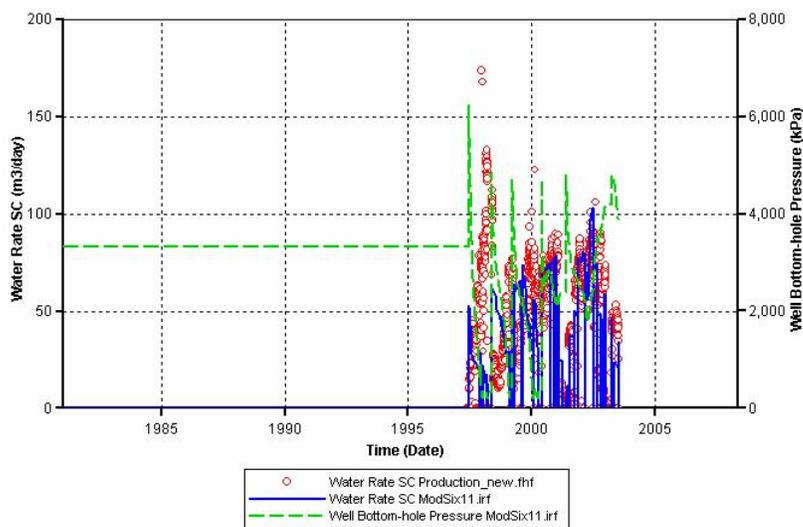
Figure. A.9 History matching results of cumulative liquid and cumulative oil production for well V5 in standard condition. The pink dots are the cumulative liquid productions from the history file. The red line is the cumulative liquid production from the simulation output. The green dots are the cumulative oil production from the history file. The blue dash line is the cumulative oil production from the simulation output.

Figure A.10 History matching results of water rate and bottom hole pressure for well V5. The red dots are the water rate in standard condition from the history file. The blue line is the water rate in standard condition from the simulation output. The green dash line is the well bottom-hole pressure from the simulation output (there is no pressure history file).

Figure. A.11 History matching results of cumulative liquid and cumulative oil production for well V10 in standard condition. The pink dots are the cumulative liquid productions from the history file. The red line is the cumulative liquid production from the simulation output. The green dots are the cumulative oil production from the history file. The blue dash line is the cumulative oil production from the simulation output.

Figure A.12 History matching results of water rate and bottom hole pressure for well V10. The red dots are the water rate in standard condition from the history file. The blue line is the water rate in standard condition from the simulation output. The green dash line is the well bottom-hole pressure from the simulation output (there is no pressure history file).